

# **Synthesis and characterization of 2D-TMDs thin films/flakes by various solution processed deposition methods for different applications**

by

**Talha Nisar**

a Thesis submitted in partial fulfillment

of the requirements for the degree of

**Doctor of Philosophy**

**in Physics**

Approved Dissertation Committee

---

Prof. Dr. Veit Wagner  
Jacobs University Bremen

---

Prof. Dr. Arnulf Materny  
Jacobs University Bremen

---

Prof. Dr. Ali Haider  
Quaid-e-Azam University Islamabad

Date of Defense: March 8<sup>th</sup>, 2021

---

Department of Physics and Earth Science




## Statutory Declaration

Family Name, Given/First Name	Nisar, Talha
Matriculation number	20331372
What kind of thesis are you submitting: Bachelor-, Master- or PhD-Thesis	Ph.D. - Thesis

**English: Declaration of Authorship:** I hereby declare that the thesis submitted was created and written solely by myself without any external support. Any sources, direct or indirect, are marked as such. I am aware of the fact that the contents of the thesis in digital form may be revised with regard to usage of unauthorized aid as well as whether the whole or parts of it may be identified as plagiarism. I do agree my work to be entered into a database for it to be compared with existing sources, where it will remain in order to enable further comparisons with future theses. This does not grant any rights of reproduction and usage, however.

The Thesis has been written independently and has not been submitted at any other university for the conferral of a PhD degree; neither has the thesis been previously published in full.

**German: Erklärung der Autorenschaft (Urheberschaft):** Ich erkläre hiermit, dass die vorliegende Arbeit ohne fremde Hilfe ausschließlich von mir erstellt und geschrieben worden ist. Jedwede verwendeten Quellen, direkter oder indirekter Art, sind als solche kenntlich gemacht worden. Mir ist die Tatsache bewusst, dass der Inhalt der Thesis in digitaler Form geprüft werden kann im Hinblick darauf, ob es sich ganz oder in Teilen um ein Plagiat handelt. Ich bin damit einverstanden, dass meine Arbeit in einer Datenbank eingegeben werden kann, um mit bereits bestehenden Quellen verglichen zu werden und dort auch verbleibt, um mit zukünftigen Arbeiten verglichen werden zu können. Dies berechtigt jedoch nicht zur Verwendung oder Vervielfältigung. Diese Arbeit wurde in der vorliegenden Form weder einer anderen Prüfungsbehörde vorgelegt noch wurde das Gesamtdokument bisher veröffentlicht.

X 29/01/2021 

---

Date , Signature



## Acknowledgement

First of all, I would like to thank my creator Almighty Allah: the most merciful and the most beneficent who gave me strength, hope, courage.

I wish to express my sincere appreciation to my Ph.D. supervisor Prof. Dr. Veit Wagner for all precious discussion and allowing me to work in his research group. I would also like to express my sincere gratitude to Dr. Torsten Balster for training me and providing technical support. I am very thankful to lab mates (Jonas Köhling, Michael Huth, Oliver Gomes, Nivedita Yumnum, Arne Hendel, Xiaoling Zeng and Vladislav Jovanov) for fruitful discussion and support in the lab. I would also like to acknowledge Prof. Arnul Materny and his group for support in the Raman lab. I am thankful to Prof. Ulrich Kortz for giving me access to electrochemical setup. A special thanks to Deutscher Akademischer Austauschdienst (DAAD) (DAAD-ID-57361932) and Jacobs University Bremen for financial support. I am also thankful to resident staff: Rennie Robert (RM), Daniel Christopher (RA), Fariba Sabzi (RA) Mauricio Moreno (RA)) in college 3 for giving me nice environment and a chance to live on campus and get experience in multi-cultural and multi-national environment.

Special thanks to my parents and my other close relatives especially my siblings, my grandmother, my uncles, cousins and my fiancé for their moral support, prayers and passion for my future.

I would also like to thank my friends : Inam ullah, Muhammad Salim, Sufyan Ramazan, Ali Haider, Tahir Zeb, Sayan, Saurav, Alireza for bringing much fun and support into my life.



# Table of Contents

1. Chapter 1. Introduction .....	1
1.1. Introduction & motivation.....	1
1.2. Transition metal dichalcogenides .....	7
1.3. Characterization methods .....	11
1.3.1. Atomic force microscope (AFM).....	11
1.3.2. Raman spectroscopy .....	13
1.3.3. UV-Vis spectroscopy .....	19
1.3.4. X-ray photoelectron spectroscopy .....	21
1.4. Hydrogen production and hydrogen evolution reaction (HER) .....	26
2. Growth of ultra-thin large sized 2D flakes at air-liquid interface to obtain 2D-WS <sub>2</sub> monolayers .....	31
2.1. Introduction .....	31
2.2. Methodology .....	32
2.2.1. Sample preparation and dip-coating .....	32
2.2.2. Conversion of dip-coated flakes to WS <sub>2</sub> .....	33
2.2.3. Characterization of precursor and flakes .....	33

2.3.	Results and discussion.....	35
2.3.1.	Mechanism behind flake formation .....	35
2.3.2.	Conversion of Flake to WS <sub>2</sub> , size , thickness of obtained flakes.....	41
2.4.	Conclusion.....	46
3.	Mechanical transfer of electrodeposited MoS <sub>2</sub> films to silicon wafer .....	47
3.1.	Introduction .....	47
3.2.	Methodology .....	48
3.2.1.	Electrochemical growth of MoS <sub>x</sub> .....	48
3.2.2.	Transfer of grown films to silicon wafer .....	49
3.2.3.	Conversion of electrodeposited films to MoS <sub>2</sub> .....	49
3.2.4.	Characterization methods.....	50
3.3.	Results and discussion.....	51
3.3.1.	Electrodeposition and mechanical transfer of MoS <sub>x</sub> films .....	51
3.3.2.	Characterization of MoS <sub>x</sub> films before and after transferred and annealing	
	54	
3.4.	Conclusion.....	60
4.	Electrodeposited ultra-thin MoS <sub>2</sub> films for hydrogen evolution reaction.....	61



4.1.	Introduction .....	61
4.2.	Methodology .....	62
4.2.1.	Sample preparation and electrodeposition .....	62
4.2.2.	Characterization .....	63
4.2.3.	Hydrogen evolution reaction.....	64
4.3.	Results and discussion.....	64
4.3.1.	Film deposition and characterization .....	64
4.4.	Hydrogen evolution reaction.....	71
4.5.	Conclusion.....	75
5.	Growth of MoS <sub>2</sub> films by spin coating for hydrogen evolution reaction .....	77
5.1.	Introduction .....	77
5.2.	Methodology .....	78
5.2.1.	Spin coating of precursor and conversion to MoS <sub>2</sub> .....	78
5.2.2.	Characterization of films before and after conversion.....	79
5.2.3.	Hydrogen evolution reaction.....	80
5.3.	Results and discussion.....	81
5.3.1.	Spin coating of MoS <sub>2</sub> films and characterization .....	81

5.4.	Hydrogen evolution reaction.....	86
5.5.	Conclusion.....	89
6.	Conclusions.....	90
7.	References.....	94

## Table of Figures

Figure 1-1 Emission of greenhouse gas by different sectors (2010) adapted from IPCC (Cambridge University Press, 2014).....	1
Figure 1-2 Year vs number of transistors on an integrated chip and evolution of electronic devices [93].....	4
Figure 1-3 a) Schematic illustration of TMDs crystal structure, with metal atoms (M, blue) sandwiched between chalcogen atoms (X, yellow). b) Schematic illustration of different prototypes of TMDs [20] .....	8
Figure 1-4 Band structure of MoS <sub>2</sub> and WS <sub>2</sub> from monolayer to bulk, calculated using DFT. The green curves represent conduction band edge and blue curves represent valence band edge [20].....	10
Figure 1-5 Working principle of atomic force microscopy (AFM).....	12
Figure 1-6 Energy scheme of Rayleigh and Raman (Stokes and anti-Stokes) scattering process.....	15
Figure 1-7 Cartoon of Raman spectrometer.....	18
Figure 1-8 Schematic drawing of an UV-Vis Spectrometer.....	21
Figure 1-9 Schematic illustration of X-ray photoelectron spectrometer. ....	24
Figure 1-10 Plot of orbital binding energies versus atomic number [94] .....	26
Figure 1-11 Energy scheme of hydrogen evolution reaction (HER) and oxygen evolution reaction (OER). ....	30

Figure 2-1 Schematic illustration of the flake formation at the air-liquid interface, dip-coating process and post annealing .....	34
Figure 2-2 Time dependent UV-Vis spectra of the 0.5 mM ATTW solution kept at 70-90 °C.....	36
Figure 2-3 Raman spectra of a flake from the air-liquid interface, a flake from the bottom of the liquid (80 °C sample) and pure references (WO <sub>3</sub> and ATTW).....	38
Figure 2-4 IR spectra of the flakes after 8 hours, WO <sub>3</sub> as reference and ATTW as reference.....	40
Figure 2-5 Raman spectrum of a post-annealed flake at 800 °C.....	42
Figure 2-6 Raman measurement done at different post-annealing temperatures (500-900°C). b) Plot of FWHM against post-annealing temperature.....	42
Figure 2-7 X-ray photoelectron spectra (W <sub>4f</sub> ) of flakes before and after annealing at 800 °C and pure ATTW reference. ....	44
Figure 2-8 Atomic force microscope image (left) and thickness profile of the edge (right) of a WS <sub>2</sub> monolayer flake. ....	45
Figure 2-9 Optical microscope image of WS <sub>2</sub> flakes on a silicon wafer. Several images are stitched together to obtain a larger visible area.....	45
Figure 3-1 a) Electrochemical setup followed by post annealing scheme b) Scheme for the transfer of the electrodeposited film from Au covered growth substrate to a base silicon substrate and corresponding real image. ....	51

Figure 3-2 Thickness vs roughness plot before and after transfer with inset of atomic for microscopy image electrodeposited layers. ....	53
Figure 3-3 UV-Vis of the films electrodeposited films before and after conversion to MoS <sub>2</sub> . ....	55
Figure 3-4 a) Raman spectra of the MoS <sub>2</sub> films annealed at different temperature. b) FWHM of E2g1 and A <sub>1g</sub> peak vs post annealing temperature. ....	57
Figure 3-5 Raman spectra of MoS <sub>2</sub> films with different thicknesses (left). Atomic force microscope image of a transferred MoS <sub>2</sub> film on silicon wafer (right). ....	58
Figure 3-6 XPS spectrum: Mo <sub>3d</sub> and S <sub>2s</sub> peaks of the electrodeposited film before and after conversion to MoS <sub>2</sub> . ....	59
Figure 4-1 a) Electrochemical deposition setup. b) Deposition time vs thickness of the films plot with inset of an optical microscope image (scale bar: 20μm) of 20 nm electrochemically deposited MoS <sub>x</sub> layer of Au substrate .....	66
Figure 4-2 Thickness vs roughness plot and inset of atomic force microscope image of the electrochemically deposited film.. ....	66
Figure 4-3 Raman spectrum of electrodeposited MoS <sub>3</sub> before annealing. ....	67
Figure 4-4 Raman spectrum of electrodeposited films with different thickness after annealing at 450 °C. ....	68
Figure 4-5 XPS spectrum: Mo <sub>3d</sub> and S <sub>2s</sub> before and after annealing at 450 °C. ....	70
Figure 4-6 Polarization curve of MoS <sub>2</sub> films on ITO and Au substrate and Pt as a reference.....	73

Figure 4-7 Polarization curve of MoS <sub>2</sub> films with different thicknesses on Au substrate (left). b) Polarization curve of MoS <sub>2</sub> films with different thicknesses on Au substrate. ..	73
Figure 4-8 AFM picture of ITO on glass surface. ....	74
Figure 4-9 Tafel plots obtained from polarization curves. ....	75
Figure 5-1 Schematic illustration of the sample preparation: From liquid phase precursor till conversion to MoS <sub>2</sub> films. ....	80
Figure 5-2 a) Thickness of the films vs concentration of the precursor solution. b) Roughness vs thickness of the film with inset of atomic force microscope image of MoS <sub>2</sub> film. ....	81
Figure 5-3 Raman spectra of the annealing at 450 °C triggering conversion to MoS <sub>2</sub> . ....	83
Figure 5-4 UV-Vis absorption spectra of the films before and after annealing at 450 °C triggering conversion to MoS <sub>2</sub> . ....	84
Figure 5-5 XPS: Mo <sub>3d</sub> and S <sub>2s</sub> energy range before and after conversion to MoS <sub>2</sub> . ....	86
Figure 5-6 Polarization curves of Pt and ITO as reference and MoS <sub>2</sub> films with different thicknesses on ITO/glass substrate. Scans start at 0.2 V with the forward and backward directions indicated by the arrows. ....	87
Figure 5-7 . Tafel plot extracted from the polarization curve in the forward direction of 2.2 nm MoS <sub>2</sub> film. ....	88

## Abstract

As the Moore's law is approaching its limits. Quantum effects doesn't allow us to further reduce the dimension of the silicon-based transistor to improve the efficiency of electronics. Silicon based devices needs to be replaced with new material having better charge carrier mobility. The discovery of 2D graphene like semiconducting transition metal dichalcogenides TMDs has given a hope to research community to fabricate atomically thin devices. Atomically thin two-dimensional (2D) transition metal dichalcogenides (TMDs) are promising candidates for future electronics. Currently, the growth of large area TMDs thin films/flakes is one of the biggest challenges. A novel method for the growth of ultra-thin and large area WS<sub>2</sub> monolayer flakes has been developed by introducing a solution-based temperature-dependent process. This two-dimensional WS<sub>2</sub> growth process is low cost and environmentally friendly. WO<sub>3</sub> flakes are grown at the air-liquid interface using ammonium tetrathiotungstate ((NH<sub>4</sub>)<sub>2</sub>WS<sub>4</sub>, ATTW) as WS<sub>2</sub> precursor. The process requires a moderate activation temperature as no flakes are formed at room temperature. Successful growth of flakes was observed in an aqueous solution of the precursor at a temperature between 70 and 90 °C. These flakes could be transferred to any substrate by a controlled dip-coating process. Large 2D WS<sub>2</sub> flakes with a lateral size of up to 100 μm were obtained after sulfurization. The thickness ranged from a WS<sub>2</sub> monolayer to five monolayers, as verified by AFM. The mechanism of chemical reaction behind the formation of the flakes was investigated by FTIR, Raman, UV-Vis and X-ray photoelectron spectroscopy (XPS). The initial flakes were found to be made of WO<sub>3</sub>, which were successfully converted to WS<sub>2</sub> by a post annealing step at 500-900 °C. This simple and environmentally friendly growth technique can be used to produce large WS<sub>2</sub> flakes for next generation electronics.

Similarly, large area MoS<sub>2</sub> ultra-thin film deposition is one of the big challenges in the recent years. Electrodeposition provides an opportunity to grow such ultra-thin films on

large scale. However, the transfer of the electrochemically grown film to desired substrate is challenging. Standard transfer of thin films is done by wet etching in which the underlying substrate is etched. In this work, the polymer coated electrodeposited  $\text{MoS}_2$  films on Au are separated mechanically from the underlying substrate by using ultra-sonication. Collapse of micron-sized bubbles produced by ultra-sonication at the interface of Au and silicon substrate provides enough energy for separation due to their weak adhesion. The Au layer is then removed by standard Au-etchant (K/KI) and the polymer coated film is transferred to a desired substrate. Ammonium tetrathiomolybdate (ATTM) has been used as precursor material for the electrodeposition of the films. Initial electrochemically grown films consist of  $\text{MoS}_3$  which is reduced to  $\text{MoS}_2$  by a post annealing step at 450 °C to 900 °C. Obtained films are investigated by AFM, Raman, UV-Vis and XPS. Crystal quality improves by increasing the post annealing temperature. The thickness of the thinnest film was found to be equivalent to 2 monolayers of  $\text{MoS}_2$ , which is desirable for future electronics.

To limit global warming, the emission of greenhouse gases needs to be reduced. For this, fossil fuel consumption must be replaced by green energy sources such as  $\text{H}_2$  gas. The hydrogen evolution reaction (HER) is a potential production method for  $\text{H}_2$  gas, and it does not produce harmful byproducts. The HER performance can be enhanced by using a catalyst to lower the over-potential and minimize energy consumption.  $\text{MoS}_2$  has been demonstrated to be an excellent catalyst for HER. Here, we used electrodeposition and spin coating to produce  $\text{MoS}_2$  layers. These methods are relatively cheap, fast, solution-based and feasible at room temperature. With electrodeposition,  $\text{MoS}_2$  can be deposited on any conducting surface while spin coating can be done on any flat substrate (conducting or non-conducting). For this purpose, ammonium tetrathiomolybdate (ATTM) and molybdenum pentachloride ( $\text{MoCl}_5$ ) were used as a single-source precursor materials for electrodeposition and spin-coating, respectively. Ultra-thin  $\text{MoS}_2$  films were obtained by such deposition methods followed by sulfurization at 450 °C. The Raman spectroscopy and



X-ray photoelectron spectroscopy (XPS) results show that the deposited MoS<sub>2</sub> films (both electrodeposited and spin coated) are amorphous and have a sulfur deficiency, which is beneficial for HER activity. Due to their high hydrogen evolution efficiency and abundance, MoS<sub>2</sub> thin films can replace noble metal catalysts such as Pt. The HER activity measurements for electrodeposited MoS<sub>2</sub> showed an overpotential for 30 nm thick MoS<sub>2</sub> of -0.33 V, whereas for smaller thicknesses below 10 nm a value of -0.22 V was found. This indicates that ultra-thin films of MoS<sub>2</sub> show a better HER activity than thick films. The obtained Tafel slope of 44 mV per decade for 5 nm MoS<sub>2</sub> is better than values reported for single crystal MoS<sub>2</sub> and other 2D materials such as WS<sub>2</sub>. The performance of the ultra-thin films of MoS<sub>2</sub> is better than thicker films of MoS<sub>2</sub>. The measured Tafel slope is 43 mV per decade which is similar to electrodeposited MoS<sub>2</sub> films.

## List of Abbreviations and Symbol

Abbreviations	Explanations
<b>2D</b>	Two-dimensional
<b>AFM</b>	Atomic force microscopy
<b>ALD</b>	Atomic layer deposition
<b>ATTM</b>	Ammonium tetrathiomolybdate
<b>ATTW</b>	Ammonium tetrathiotungstate
<b>CVD</b>	Chemical vapor deposition
<b>FET</b>	Field-effect transistor
<b>FWHM</b>	Full width at half maxima
<b>HRTEM</b>	High resolution transmission electron microscopy
<b>HER</b>	Hydrogen evolution reaction
<b>IR</b>	Infrared (spectroscopy)
<b>ITO</b>	Indium tin oxide
<b>MoCl<sub>5</sub></b>	Molybdenum(V)-chloride
<b>MOCVD</b>	Metal organic chemical vapor deposition
<b>MoS<sub>2</sub></b>	Molybdenum disulfide
<b>MoS<sub>3</sub></b>	Molybdenum trisulfide
<b>MoO<sub>3</sub></b>	Molybdenum trioxide
<b>RMS</b>	Root mean square
<b>Rms</b>	rotation per minute
<b>PMMA</b>	Poly(methyl methacrylate)
<b>SEM</b>	Scanning electron microscopy
<b>TMD</b>	Transition metal dichalcogenides
<b>XPS</b>	X-ray photoelectron spectroscopy
<b>UV-Vis</b>	Ultraviolet visible spectroscopy

$\mu$	Carrier mobility
-------	------------------

## Thesis organization

Based on the content of this Ph.D. work, this thesis is presented in 5 chapters that are organized in following way.

**Chapter 1** contains a short introduction and motivation about this research work. TMD semiconductors are introduced especially  $\text{MoS}_2$  and  $\text{WS}_2$ . Crystal structure and band structure of  $\text{MoS}_2$  and  $\text{WS}_2$  are described. Basic principles of characterization methods, i.e., atomic force microscope, Raman spectroscopy, UV-Vis spectroscopy, and x-ray photoelectron spectroscopy, used in this work are discussed. Hydrogen evolution reaction as an application of  $\text{MoS}_2$  is also introduced.

**Chapter 2** covers the growth of ultra-thin large sized 2D at air-liquid interface to obtain  $\text{WS}_2$  monolayer flakes. A novel method for the growth of ultra-thin and large area  $\text{WS}_2$  monolayer flakes has been developed by introducing a solution-based temperature-dependent process.  $\text{WO}_3$  flakes are grown at moderate temperature at this air-liquid interface for the first time. Grown 2D flakes were successfully converted to  $\text{WS}_2$  by sulfurization. Thickness of the thinnest film was found to be equivalent of a monolayer of  $\text{WS}_2$ . Crystal quality of the obtained  $\text{WS}_2$  flakes was found be improved with increasing annealing temperature.

**Chapter 3** presents a mechanical transfer of electrochemically grown ultra-thin  $\text{MoS}_2$  films from the growth substrate to a silicon substrate. For this purpose, ammonium tetrathiomolybdate has been used as a precursor material. Electrodeposited films are separated from the growth substrate by ultra-sonication. The Gold layer was etched by standard gold etchant (KI). After etching gold layer, floating polymer coated  $\text{MoS}_x$  layer on gold etchant was picked up by clean silicon wafer. Polymer was removed with acetone. Transferred  $\text{MoS}_x$  layers were sulfurized at high temperature (450-900 °C).  $\text{MoS}_2$  bilayer

is successfully obtained as verified by Raman and AFM. Crystallinity of MoS<sub>2</sub> was found to be improved with increasing post-annealing temperature.

**Chapter 4** presents growth of MoS<sub>2</sub> films by electrochemical deposition for hydrogen evolution reaction. With electrodeposition thin films can be grown on large scale. Electrodeposited MoS<sub>x</sub> films were sulfurized at 450 °C. The Obtained MoS<sub>2</sub> films are found to be active catalyst for hydrogen evolution reaction. Thickness dependent HER activity is also studied. The HER activity measurements for electrodeposited MoS<sub>2</sub> showed an overpotential of -0.33 V for 30 nm thick MoS<sub>2</sub>, whereas for smaller thicknesses below 10 nm a value of -0.22 V was found. This indicates that ultra-thin films of MoS<sub>2</sub> show a better HER activity than thick films. A Tafel slope of 44 mV per decade was obtained for 5 nm MoS<sub>2</sub>.

**Chapter 5** presents ultra-thin spin coated MoS<sub>2</sub> films for hydrogen evolution reaction. For this purpose, a novel single source Mo-precursor molybdenum pentachloride (MoCl<sub>5</sub>) is used. The Spin coated precursor is converted to MoS<sub>2</sub> by post annealing at 450 °C with additional sulfur in inert environment. The HER activity is presented for available thicknesses. The HER activity for 2.2 nm thick MoS<sub>2</sub> film is determined at an over-voltage of -0.25 V while for 15 nm films HER activity is observed at -0.44 V. Tafel slope is 43 mV per decade which is similar to electrodeposited MoS<sub>2</sub> films.

## **Objectives of the thesis**

Graphene and its 2D analogue semiconducting TMDs have been grown by various well-established growth methods, i.e. chemical vapor deposition and atomic layer deposition for various applications (transistor, vallitronic, photovoltaic devices, hydrogen evolution reaction). Motivated by the importance for 2D TMDs application, This Ph.D. work is focused on:

- i) Growth of large area 2D TMDs (especially WS<sub>2</sub> and MoS<sub>2</sub>) films/flakes based on alternative solution-based deposition methods.
- ii) Improvement of the crystallinity of the grown TMDs films/flakes.
- iii) Hydrogen evolution reaction activity on 2D TMDs.

## 1. Chapter 1. Introduction

### 1.1.Introduction & motivation

Global warming is one of the major challenges of the world. In the past few decades, the emission of the greenhouse gases has significantly increased. Fossil fuel consumption and industrial processes are the main sources of CO<sub>2</sub> emission, which is 78% of the total greenhouse gas emission. Increasing human population and economic growth are directly linked to the global greenhouse gas emission. In the past two centuries the human population is grown from 1 billion to 7.8 billion . The current growth rate is 1.1% per year which is around 0.083 billion annually (Source: United Nations (2020)). The economic sector is also increased accordingly to fulfill the requirements of the people. In figure 1.1 greenhouse gas emission by various sectors are shown.

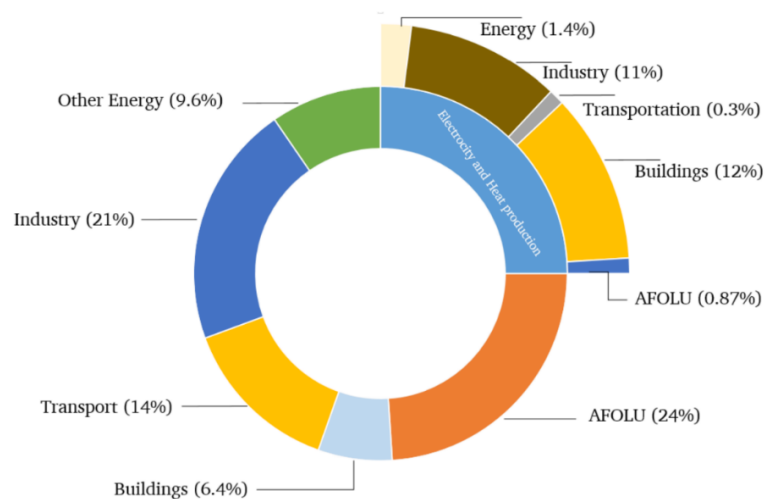


*Figure 1-1 Emission of greenhouse gas by different sectors (2010) adapted from IPCC (Cambridge University Press, 2014)*

To reduce the emission greenhouse gas, European Union is trying to replace fossil fuel consumption with clean energy sources. The target is to reduce 80-95% greenhouse gas emission by 2050 [1]. There are many proposed alternative options to avoid fossil fuel consumption such as windmills, solar energy, hydraulic energy, and hydrogen gas. Replacing the consumption of the fossil fuel is not an easy task because the alternative green energy sources are not consistent and stable temporally. For example, the solar energy cannot be used effectively in Germany especially in winter due to the lack of the sunlight. Similarly, for the wind energy, a constant significant wind is required. Among other proposed alternation options, hydrogen evolution reaction provides a long-term and best solution because of the abundance of water and higher energy density of hydrogen . Production of hydrogen gas through hydrogen evolution reaction can replace fossil fuel consumption and support economic section such as energy production, industries, and transportation. Hydrogen is one of the best green energy sources because it produces harmless by-products. In the past three decades, Germany has increased the production of green energy significantly (6 times). Currently in 2020, green energy consumption is only 18% of the net energy-consumption (Eurostat report). Intensive study has been done to consider hydrogen as an alternative energy source to fossil fuel to reduce greenhouse gas emission in Germany. In fact, a theoretical study shows that investment in hydrogen production is more beneficial for Germany due to high share of renewables in EU [2]. In simple words production of the hydrogen gas through hydrogen evolution reaction is one of the most promising ways to reduce emission of greenhouse gases in future. Hydrogen



gas can be obtained by the electrolysis of water. A suitable catalytic electrode can reduce the overpotential and minimize energy consumption. Currently the state-of-the-art catalyst for the electrolysis of water is platinum [3]. But due to its high cost and low abundance platinum cannot be used for mass production of hydrogen gas.  $\text{MoS}_2$  and  $\text{WS}_2$  has been demonstrated to be an alternative catalyst for hydrogen evolution reaction because of their abundance in nature and suitable band structure [4], [5]. In my work, I have also demonstrated  $\text{MoS}_2$  to be an active catalyst for hydrogen evolution reaction. We produced  $\text{MoS}_2$  thin layers by two different solution-based processes, i.e. electrochemical deposition, and spin-coating. These solution-based processes are large area deposition methods and doable at room temperature followed by a sulfurization step. These deposition methods can be used for mass production of  $\text{MoS}_2/\text{WS}_2$  for hydrogen evolution reaction in future. Furthermore, TMDs semiconductors are also potential candidates for future electronics.

Ever since the transistor was invented, its size is getting smaller and smaller which is the building block of electronic devices. Similarly, the number of transistors per unit area on an integrated circuit doubles every eighteen months (see figure 2). Based on this observation Gordon Moore derived Moore's law in 1965 [6]. The performance of the electronic devices is also getting better and better as the size of transistor gets smaller and number of transistors increases on the electronic chip. The performance of the field effect transistor depends on certain parameters, i.e. charge carrier mobility, channel length, threshold voltage and contact resistance. High performance transistor requires low dimensions and high carrier charge mobility. Researcher are trying to further reduce the

dimension of the transistor to improve performance further. Currently, dimensions of a transistor in modern electronics is in the range of few nanometers. So, the transistor is less than 100 atoms across. Dimensions of the transistor is already approaching the limits of the Moore's law. At the nanoscale, quantum effects play its role, i.e. quantum mechanical tunneling. We will have leakage currents because the electrons can cross the barrier in the transistor due to quantum tunneling. Quantum effect pose a limit to Moore's law. This is a big challenge for the researchers. Quantum effects prevent us to further reduce the dimensions of the transistor.

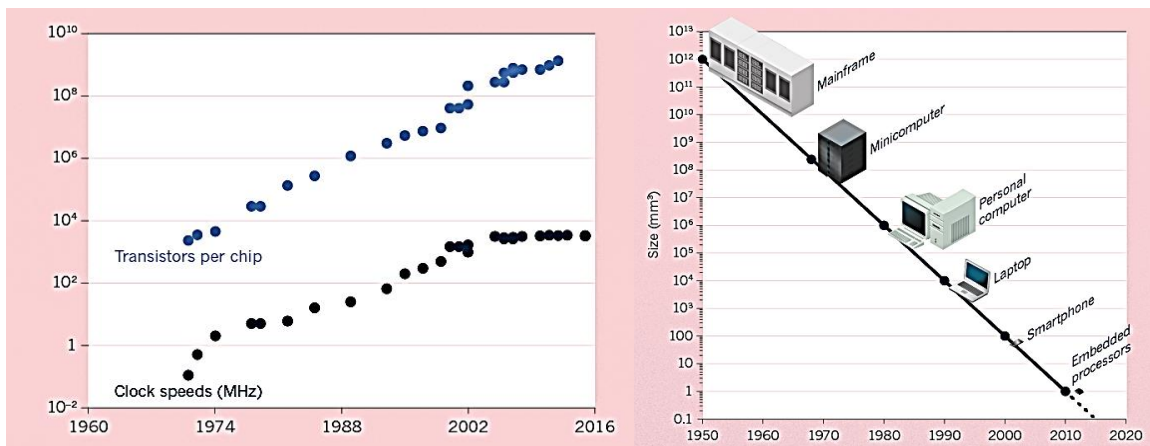


*Figure 1-2 Year vs number of transistors on an integrated chip and evolution of electronic devices [93]*

Alternative way to improve performance of a transistor is to use a material with higher charge carrier mobility than silicon. Silicon based transistors need to be replaced by other semiconducting material which has higher charge mobility. The discovery of atomically

thin graphene has opened a completely new research area and a hope for scientists. High performance graphene-based field effect transistor has been reported with carrier mobility  $> 120000 \text{ cm}^2\text{V}^{-1}\text{s}^{-1}$  [7] but due to a conducting nature of a graphene, this transistor cannot be properly switched-off. So, graphene is not an appropriate material for switching devices. Scientists were looking for analogue materials which has similar properties like 2D-graphene but with finite bandgap (semiconducting materials). It is found that transition metal dichalcogenide (TMDs) are similar two-dimensional (2D) materials [8], [9]. Among other TMDs,  $\text{MoS}_2$  and  $\text{WS}_2$  show best properties [10]. TMDs semiconductors possess a non-zero bandgap (1-2 eV) [10]. It has been demonstrated that  $\text{MoS}_2$  and  $\text{WS}_2$  show good properties such as high mobility, thickness dependent band structure [11][12][13]. Now the next challenge is to grow TMDs semiconductors thin films on large scale for different applications. In this research, new deposition methods are developed, i.e. electrochemical deposition, dip-coating, and spin-coating to produce  $\text{MoS}_2/\text{WS}_2$  ultra-thin films/flakes. The electrochemically deposited  $\text{MoS}_2$  films have been successfully transferred from a conducting growth-substrate to a silicon substrate by a mechanical transfer method followed by gold etching.  $\text{MoS}_2$  has also been deposited by spin-coating on ITO and silicon wafers. Similarly, large lateral sized  $\text{WS}_2$  flakes have been obtained by dip-coating process [14]. TMDs thin films/flakes obtained by such processes are candidates to be used for transistor fabrication in future.

TMDs semiconductors are 2D materials with monolayer thickness less than 1 nm [15].

$\text{MoS}_2$  and  $\text{WS}_2$  has been demonstrated to be the best among other TMDs semiconductor

because of their interesting band structure and moreover MoS<sub>2</sub> is an abundant in nature. To make ultra-thin layers of TMDs for different applications proper deposition methods need to be developed. Primary goal is to grow uniform ultra-thin sheets of TMDs (ideally monolayers) on large scale for industrial applications. In 2011, the first MoS<sub>2</sub> high performance transistor has been reported by Kiss research group [8]. MoS<sub>2</sub> flakes were obtained by mechanical exfoliation (scotch-tape method). The reported MoS<sub>2</sub> transistor's performance was great with a carrier mobility of  $\sim 200 \text{ cm}^2\text{V}^{-1}\text{s}^{-1}$ . However, with mechanical exfoliation, the size and the thickness of the flakes cannot be controlled. The reported lateral size of MoS<sub>2</sub> flake was in the range of  $10 \mu\text{m}$  so this method is not suitable for mass production of TMDs. MoS<sub>2</sub> and WS<sub>2</sub> monolayer have also been deposited by vacuum processed deposition methods, i.e. atomic layer deposition (CVD) [9], [16], metal organic CVD [17] and atomic layer deposition [18]. Currently above mentioned vacuum processes are well-established deposition methods yielding monolayers flakes with lateral size of few centimeters [9]. Deposition by such methods are done at high temperature and under low pressure vacuum. The substrate must be nonflexible. Sometimes the precursor used is a toxic material. Alternative solution-based deposition methods are presented here such as electrochemical deposition, dip-coating, and spin-coating. These solution-based deposition methods combine several advantages, i.e. cheaper precursor material, ability for mass production, and to be compatible with wide range of substrates.

## 1.2. Transition metal dichalcogenides

Transition metal dichalcogenides (TMDs) are the 2D material analogue to conducting graphene. They possess a non-zero bandgap ranging from 1-2 eV [19], [20], are important for hydrogen evolution reaction and for switching devices such as field effect transistors. TMDs are a group of materials with chemical formula  $\text{MX}_2$ , where M represents a transition metal atom from the chromium family (group IVB, particularly molybdenum and tungsten) and X represents an atom from the oxygen family (group VIA, particularly sulfur and selenium). Within the 2D sheets, the atoms are covalently bonded that's why TMDs are mechanically strong materials while the sheets are connected with each other by a weak van der Waals force which make TMDs flexible. Due to the weak van der Waals force between the sheets, they can slide over each other so TMDs (specially  $\text{MoS}_2$ ) can be used as lubricant. The transition metal in  $\text{MX}_2$  is sandwiched between chalcogen atoms. This structure is extended into 2D sheet and makes a hexagonal structure. The 2D sheets are stacked together in different ways (polytypes) which has different stacking orders and M-coordination. The TMDs have either hexagonal or rhombohedral crystal structure and the metal atom in the crystal has octahedral or trigonal prismatic coordination [20]. The commonly known prototypes are 1T, 2H and 3R, where T represents trigonal, H represents hexagonal and R represents rhombohedral (see figure 1.3). The digits in the prototypes represents the number of TMD molecules present in the unit cell. The lattice constant varies between 0.31 nm to 0.37 nm depending on TMDs material. The spacing between the interlayers is 0.65 nm. The letter “c” is the stacking index with defines the number of the

sheets in each prototype. So stacking index is different for each prototype, i.e.  $c$  is 0.65 nm for 1T-prototype, 1.95 nm for 3R-prototype and 1.3 nm for 2H-prototype.

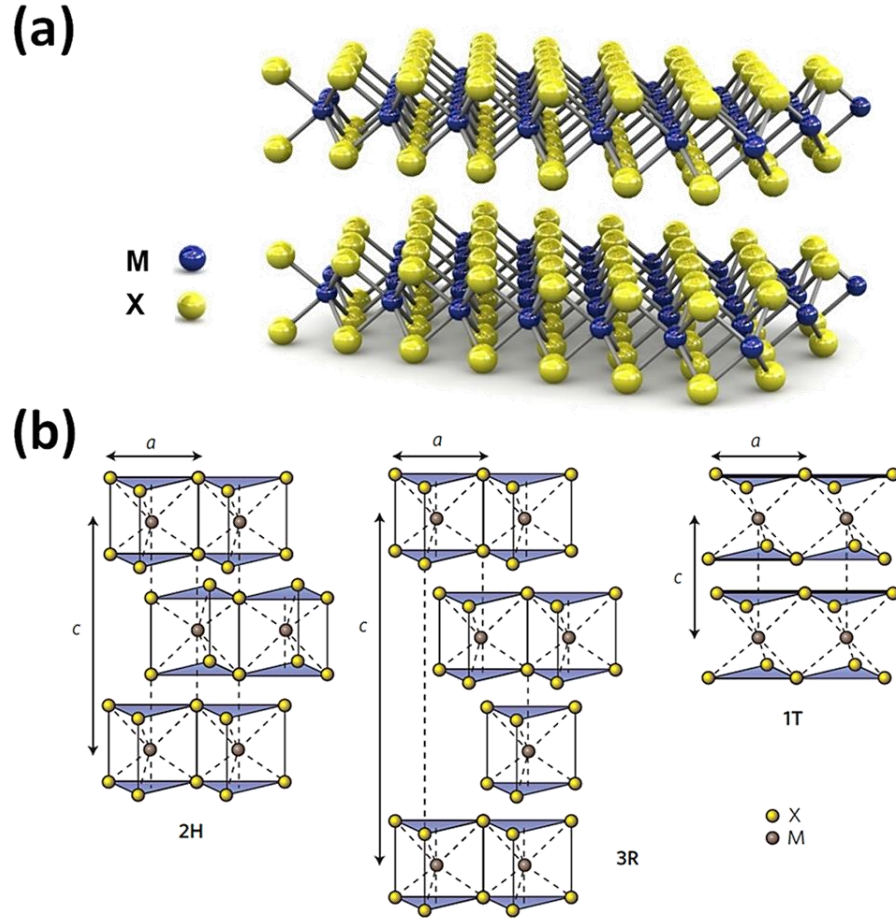
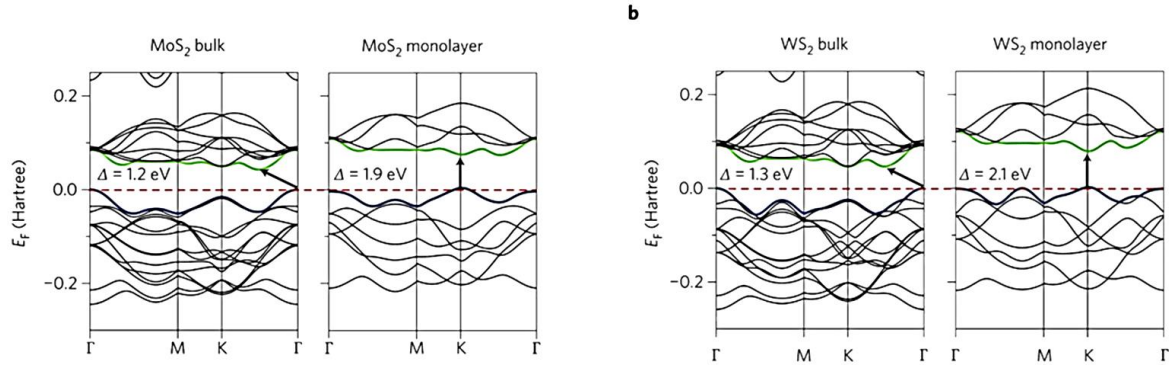


Figure 1-3 a) Schematic illustration of TMDs crystal structure, with metal atoms (M, blue) sandwiched between chalcogen atoms (X, yellow). b) Schematic illustration of different prototypes of TMDs [20]

This work is mainly focused on 2H  $\text{MX}_2$ , which is stable semiconductor. From the family of TMDs,  $\text{MoS}_2$  and  $\text{WS}_2$  show interesting properties and are intensively studied. They have been used in many areas such as catalyst for hydrogen evolution reaction [21], [5], spintronics [22], photocatalyst [23], and field effect transistor [8], [11], because of their characteristic band structure. Monolayer of  $\text{MoS}_2$  and  $\text{WS}_2$  are direct semiconductors with a bandgap of 1.8 and 2.3 eV, respectively [20]. The bandgap of the monolayer originates from the transition at the K point in the Brillouin zone. The optical bandgap (transition at K symmetry point) is independent of the thickness of the TMDs [20]. As the thickness of the TMDs increases, the band structure switches from direct semiconductor to indirect semiconductor. The transition from the direct semiconductor to indirect semiconductor happens because the valence band at the  $\Gamma$  symmetry point moves up and the conduction band at the middle of  $\Gamma$  and K points moves down with increasing thickness of TMD. Bulk  $\text{MoS}_2$  and  $\text{WS}_2$  is an indirect semiconductor with bandgap of 1.23 and 1.32 eV, respectively. The indirect bandgap comes from the transition between conduction band at the mid of K and  $\Gamma$  points and valence band at the  $\Gamma$  point. The band structure of  $\text{MoS}_2$  is shown in figure 1.4.



*Figure 1-4 Band structure of MoS<sub>2</sub> and WS<sub>2</sub> from monolayer to bulk, calculated using DFT. The green curves represent conduction band edge and blue curves represent valence band edge [20]*

The TMDs show a wide range of interesting properties depending on their band and crystal structure. Some TMDs are insulator such as HfS<sub>2</sub>, some have semiconducting nature such as 2H MoS<sub>2</sub> and WS<sub>2</sub>, some behaves like a metal such as VSe<sub>2</sub> and interestingly some are superconductors, i.e. TaSe<sub>2</sub> [20]. The monolayer of TMDs has attracted the attention of the research community because of its unique properties in electronics. The monolayer of MoS<sub>2</sub> can easily be obtained using scotch tape method or mechanical exfoliation. The mobility of a MoS<sub>2</sub> monolayer transistor is  $\sim 200 \text{ cm}^2\text{V}^{-1}\text{s}^{-1}$  at room temperature [8]. The current on/off ratio is  $1 \times 10^{-8}$ . Similarly, MoS<sub>2</sub> and WS<sub>2</sub> have also been demonstrated to be a good catalyst for hydrogen evolution reaction because of their suitable band structure [24], [5]. MoS<sub>2</sub> and WS<sub>2</sub> have been deposited by various deposition methods, i.e. chemical vapor deposition (CVD) [9], spin-coating [25], dip-coating [26], [14], electrochemical deposition [3], and spray coating [27]. TMDs have also been demonstrated to be active



catalyst for hydrogen evolution reaction because of their suitable band structure. Electrochemically deposited MoS<sub>2</sub> show good HER active with a small Tafel slope of 40 mV per decade [28].

### **1.3.Characterization methods**

#### **1.3.1. Atomic force microscope (AFM)**

Atomic force microscopy (AFM) is a characterization technique used to get a detailed topological information of a surface of a thin film on nanometer scale. It is done by measuring forces between the film's surface and a fine tip. AFM consists of a fine tip which is attached to a cantilever. A laser beam shines on the tip that is reflected onto a 4 quadrant photodetector which produces an electric current and the cantilever is scanned across the surface. Due to the microscopic roughness of the layer, the tip is deflected during the scanning process. This deflection causes a change in the position of the reflected laser beam on the 4-quadrant photodetector. The photocurrent of the 4-quadrant photodetector changes

accordingly. This is how topology of the surface is recorded. The basic working principle of AFM is shown in figure 1.5.

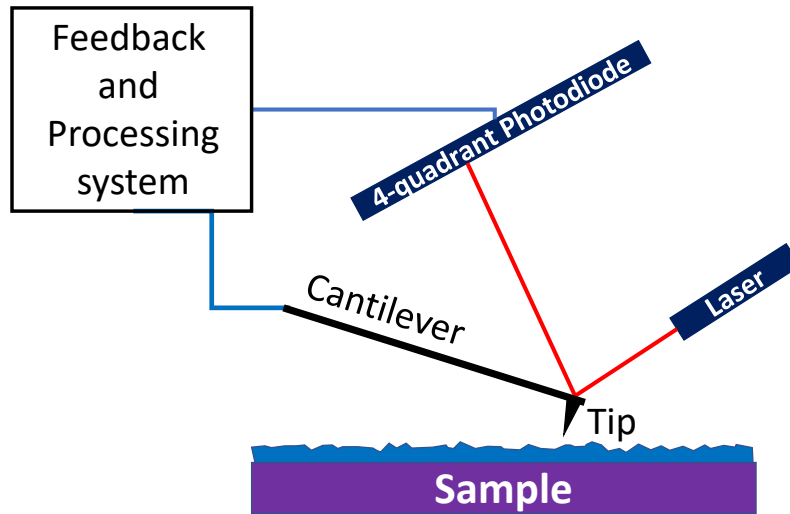


*Figure 1-5 Working principle of atomic force microscopy (AFM).*

The AFM can be operated in mainly three modes, a) Contact mode: the tip physically touched the surface of the film and deformation of the cantilever due to the roughness of the surface is recording, b) tapping mode: The cantilever taps the surface and oscillates close to its resonance frequency. The vibration in cantilever is obtained by piezo element. The frequency and amplitude remains constant until tip interacts with the surface of the sample. As tip approaches the surface, the amplitude changes due to possible interacting forces, i.e. weak Van der Wall force, dipole interaction or electrostatic forces. The controller adjust the height of the tip accordingly. In this mode, the AFM topological image is produced by recording the interacting forces between the tip and surface of the sample.

c) non-contact mode: The cantilever oscillates but doesn't physically touch the surface of the film. In this mode, the cantilever is vibrated at its resonance frequency. The interacting forces between the tip and the surface of the sample change resonance frequency of the cantilever. This change in resonance frequency allows the controller to maintain distance between the sample and the tip. The topological AFM image is obtained by measuring the distance between the tip and surface of the sample. In this research, the AFM (Nanosurf) was operated in tapping mode. AFM is a very sophisticated method to measure the thickness and roughness of the films. For topological information the AFM measurements are performed on the middle of the film. In order to get the thickness of the films the AFM measurements are performed on the edge of the film and part of the underlying substrate. The difference between the top of the film's edge and the substrate along perpendicular axis to the surface is the height of the film. Since the thickness of the TMDs monolayer is well-defined [20]. The number of MoS<sub>2</sub>/WS<sub>2</sub> sheets present in a grown film can be obtained from the thickness of the film.

### **1.3.2. Raman spectroscopy**

Raman spectroscopy is a non-destructive way to study the structural fingerprint of a material by addressing the vibrational modes, e.g. of a WS<sub>2</sub> and MoS<sub>2</sub> crystal. It gives us information about the lattice dynamic, i.e. Raman active modes. Raman scattering phenomenon was discovered by an Indian physicist Sir Chandrasekhara Venkata (CV) Raman. He found that the wavelength of the incident light changes (increase or decrease)

when interact with some materials. This phenomenon was found to be a new type of light scattering (inelastic scattering) and was called Raman scattering, named after its discoverer Sir CV Raman. Sir CV Raman was awarded a Nobel prize in physics in 1930 for the discovery of the Raman scattering. When the light hits the surface of a material, it can be reflected, refracted, transmitted or scattered. If the energy of incident photon is equal to the energy difference between two energy level in a crystal system, then the incident photon can be absorbed by the system and the system will be excited. Absorption spectroscopy is based on this phenomenon. If the bandgap of a material is larger than the energy of an incident photon, the light will pass through the material without absorption. Scattering (elastic or inelastic) can also occur when a photon interacts with the material. For scattering phenomenon, the energy of the incident photon does not have to match with the bandgap of the material. In fact, virtual states are involved in the scattering process. The lifetime of those virtual states are extremely short ( $\sim$  *femtosecond*). In scattering process when a photon interact with a crystal, the system goes from a vibrational ground state to a virtual states and it comes back to vibrational ground state by releasing a photon. If the energy of the incident photon and the scattered photon is equal, this type of scattering is called Rayleigh scattering. But if the system comes back from the virtual state to vibrational excited state, so the energy of the incident photon will be larger than that of the scattered photon. This type of inelastic scattering is called Stokes Raman scattering. If a photon interacts with a crystal which is already vibrationally excited and crystal comes back to the ground state after scattering, the energy of the scattered photon will be higher than that of

incident photon. This inelastic scattering is known as anti-Stokes Raman scattering. At low temperature the Stokes Raman scattering is dominant because most of the crystals are in the vibrational ground state, while at high temperatures anti-Stokes process becomes dominant because more crystals are in the vibrational excited state due to available thermal energy. Different types of scattering are shown in figure 1.6.

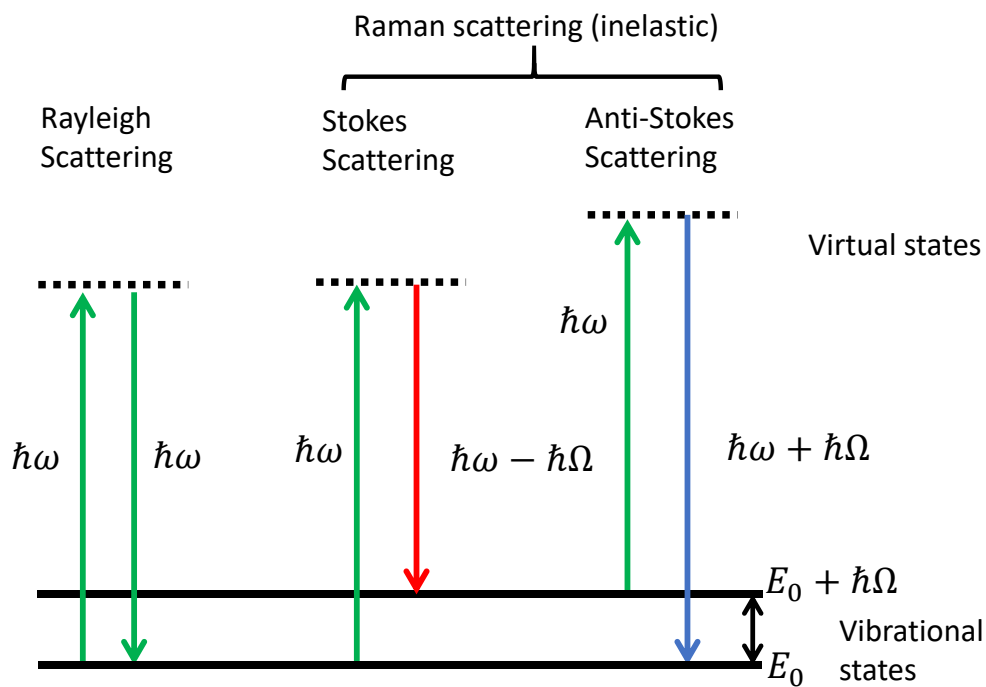


*Figure 1-6 Energy scheme of Rayleigh and Raman (Stokes and anti-Stokes) scattering process.*

The scattering process can also be explained in a different way. Light is an electromagnetic wave. When light interacts with a crystal, it distorts the electron cloud around the nucleus.

If the nuclear motion is not involved in this interaction, the energy of the incident photon will be equal to the scattered photon. This scattering is called Raleigh scattering. The mass of the nucleus is very high compared to electrons. If nuclear motion is involved in a scattering process then there will be either transfer of energy from the photon to the system (Stokes Raman scattering) or from the system to the scattered photon (anti-Stokes Raman scattering). The distortion of the electron cloud depends on the excitation source (the energy of a laser used in experiment). In other words, the energy of virtual states depends on the energy of the incident photon or frequency of laser source.

The crystal can be modeled as solid spheres (atoms) connected with each other by a spring. If there are N atoms in a molecule, then there will be 3N-3 modes of vibrations. The energy or frequency of each mode of vibration depends on the masses of each sphere (atom) at the end of the spring and the spring force constant. In the case of a real crystal the spring constant is defined by the bond between (among) the atoms. Hook's law can be applied to this model of a crystal system. We can determine the frequency of different modes of vibrations that depends on the mass of atoms and the bond between the atoms [12]. The following equation is for diatomic molecule with mass  $m_1$  and  $m_2$  attached with a bond.

$$\nu = \frac{1}{2\pi} \times \sqrt{\frac{2K}{\mu}}$$

Where  $\nu$  is the frequency,  $K$  is the force constant,  $c$  is the speed of light and  $\mu$  is the reduced mass ( $\frac{1}{\mu} = \frac{1}{m_1} + \frac{1}{m_2}$ ) of the atoms involved in the vibration. If the mass of the atoms in a crystal is small, then the frequency will be high. Similarly, if the bond between the atoms is strong then the frequency of the vibration will be high. Raman spectra are typically plotted in wavenumber scale instead of wavelength because wavenumber is directly proportional to energy. The Raman shift can be expressed as

$$\bar{\nu} = \left( \frac{1}{\lambda_{in*}} - \frac{1}{\lambda_{scatter}} \right)$$

Where  $\bar{\nu}$  is the Raman shift given in a wavenumber,  $\lambda_{in*}$  is the wavelength of incident photon and  $\lambda_{scatter}$  is the wavelength of a scattered photon in vacuum.

In the Raman spectroscopy, the shift in the energy of incident photons and the scattered photons gives us information about the structural fingerprints of material. Theoretical study shows that MoS<sub>2</sub>/WS<sub>2</sub> has four Raman active modes [29], i.e A<sub>1g</sub> (an out of plane vibration), E<sub>2g</sub><sup>1</sup> (an in-plane vibration in basal plane of Mo and S atoms), E<sub>1g</sub> (an in-plane vibration in basal plane of S atoms), E<sub>2g</sub><sup>2</sup> (an in-plane vibration in basal plane of Mo and S atoms). In our work E<sub>2g</sub><sup>1</sup> and A<sub>1g</sub> are studied. The peak position of these two modes depends on the thickness of the TMDs layers. As the thickness of TMD layers increases from monolayer, the peak position of E<sub>2g</sub><sup>1</sup> moves to lower wavenumbers (Red-shift) while the peak position

of  $A_{1g}$  moves to higher wavenumbers (blue shift). So the peak position of these two Raman active modes ( $E_{2g}^1$  and  $A_{1g}$ ) can give us information about the thickness of the obtained film.

In this work, the Raman measurements (Horiba Jobin-Yvon T64000 spectrometer) were carried out with a green laser ( $Ar^+$  ion) as an excitation source with 514.5 nm wavelength. 50x objective was used to collect the signal and dispersed with 2400 lines/mm grating. The Raman scattered light was detected by charged-coupled device (CCD) detector which was cooled by liquid nitrogen to  $-110^\circ C$ . The Raman experimental setup is illustrated in figure 1.7. The beam splitter shown in figure 1.7 is an optical device that split the laser beam into two beams. The Notch filter used in Raman setup is a type of filter that stops light with a range of frequencies. Light with frequencies below and above this range is allowed to pass through the Notch filter. The purpose of this filter is to stop the primary laser beam's entry to spectrometer.

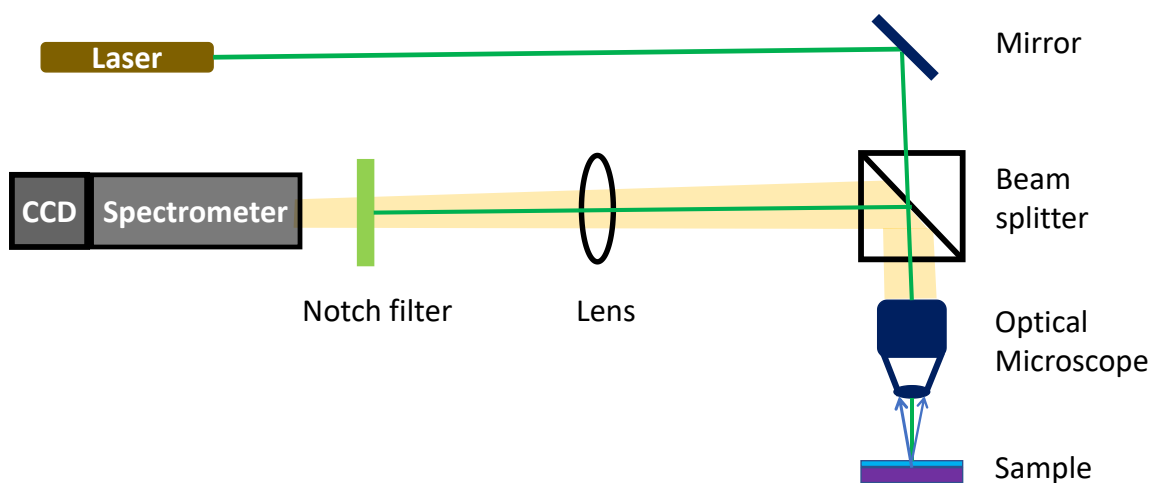


*Figure 1-7 Cartoon of Raman spectrometer*



### 1.3.3. UV-Vis spectroscopy

UV-Vis spectroscopy is an optical spectroscopy based on the interaction of the material with visible and ultraviolet light. This spectroscopy is used in many areas, i.e research, industries, production and quality control, to characterize different materials. Tungsten lamp is usually used as a light source in UV-Vis spectroscopy. In this work, UV-Vis measurements were done in absorption mode. The light is shine on the sample and it absorb light with specific wavelength. The transmitted light is first diffracted and then directed onto the photodetector. The absorption of the light has a direct relation with the amount of substance present in the sample, thickness of the sample and extinction coefficient. The extinction coefficient is specific to each material. Furthermore, the absorption is indirectly proportional to the transmitted light. The absorption of the light can be explained by Beer-Lambert law

$$A = \varepsilon . c . d$$

Where A is the absorbance, c is the concentration of the substance, d is the pathlength of the sample and  $\varepsilon$  is the extinction coefficient. The above equation is applicable to liquid samples. In this work, UV-Vis measurements of ATTW are done in liquid phase. For solid samples, the concentration is 100%. The UV-Vis measurements are performed in reflection or absorption mode in order to get excitonic fingerprints of the material. When a material is exposed to light with range of energies, the photon energy is transferred to the crystal. Absorption (A) is the ratio between the transferred energy to the material and the incident

19

energy. The absorption can be presented in terms of transmission (T) and reflection (R). In this work, the UV-Vis measurements are done in an absorption mode.

$$A = 1 - R - T$$

In other words, the absorbance (Abs) measurement is telling us about the amount of energy transferred to the sample. It is also called the optical density of the sample. The absorbance can be expressed in terms of reflectance or transmittance

$$Abs = -\log_{10}(T)$$

For above relation, it is assumed that either R or T is equal to zero. Which means that the sample is either transparent or highly reflective. In this work, the absorption spectrum (see figure 3.2) exhibits excitonic peaks at 612 , 674 nm which corresponds to A and B exciton of MoS<sub>2</sub>, respectively. These excitons are assigned to the direct optical transition between valence band and the conduction band at the K symmetry point in Brillion zone. Furthermore, there is another broad peak in the absorption spectrum around 400-450 nm which is assigned to the C and B excitons. The experimental set of UV-Vis spectrometer is shown as follows.

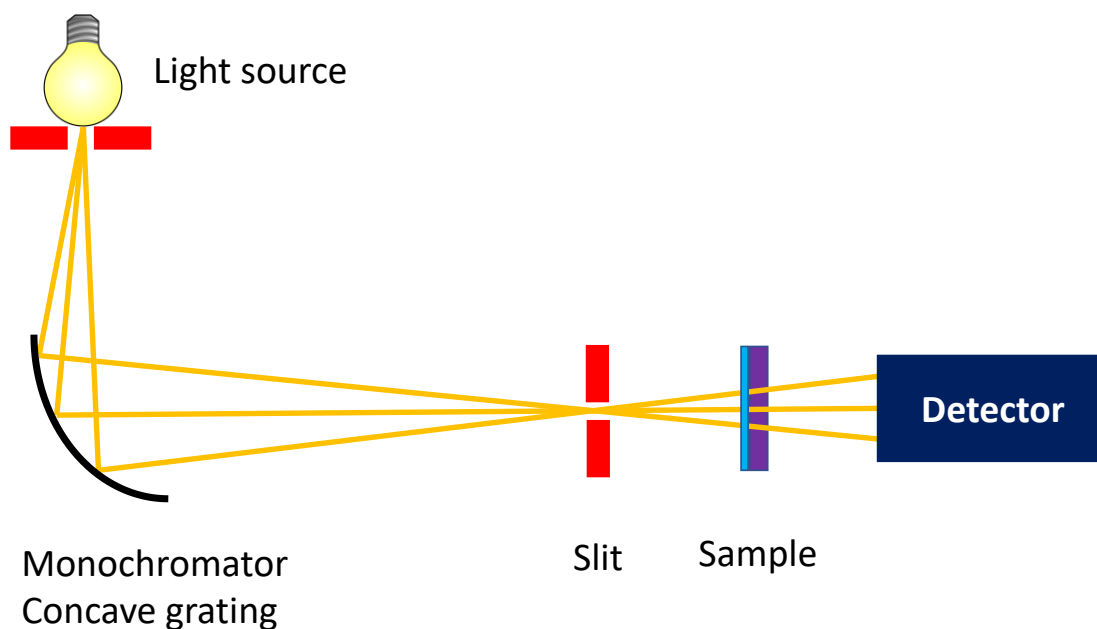


*Figure 1-8 Schematic drawing of an UV-Vis Spectrometer*

#### **1.3.4. X-ray photoelectron spectroscopy**

X-ray photoelectron spectroscopy (XPS) is surface sensitive spectroscopic method used to find composition and chemical state of atoms in a material. The basic physics behind XPS is the photoelectric effect experimentally discovered by Heinrich Hertz in 1885. German-American physicist Albert Einstein explained photoelectric effect theoretically by introducing the concept of an energy packet called photon. Albert Einstein got a Nobel prize for the explanation of this effect. The photoelectric effect describe the process when a photon hits an atom and this photon is absorbed, that an electron is ejected with finite

kinetic energy. In this process the total energy is conserved. The kinetic energy of the ejected electron can be explained by the following equation

$$KE = h\nu - BE - \theta$$

In the above equation, KE represents the kinetic energy of the ejected electron,  $h\nu$  represents the energy of the incident photon, BE represents the binding energy of the electron in the atom with respect to the Fermi energy of the material and  $\theta$  is the work function of material. In XPS, X-rays are produced by hitting an Al/Mg anode with accelerated thermionically generated electrons. In our experiment, X-rays (1253.6 eV) are shined on the surface of the material which results in the ejection of the electrons called photoelectrons. The ejected electrons leave an empty space behind. This empty space is refilled by electrons from the upper energy levels by either emitting another photon or kicking out another electron called Auger electron. The energy of the Auger electron does not depend on the incident photon's energy that's why Auger spectrum is often represented on kinetic energy scale. In the XPS process, when the ejected electron passes through solid material, it can be scattered either elastically or inelastically. If the electron loses kinetic energy upon collision (inelastic scattering) then the desired information about the material can't be obtained. Therefore, mean free path of the electrons in the material should be considered in order to interpret the intensity information correctly. Mean free path is the average distance between two scattering events. So the corrected electron intensity can be obtained by using Beer-Lambert law

$$I = I_0 \exp(-x/\lambda \cos \theta)$$

In the above equation,  $I$  represent the reduced electron signal,  $I_0$  represents the surface electron signal,  $x$  represents the penetration depth,  $\lambda$  represents the mean free path of an electron and  $\theta$  represents the emission angle. Mean free path of electrons ( $\lambda_e$ ) depends on the kinetic energy of the electrons for different elements. The dependence of  $\lambda_e$  on kinetic energy is strong and it depends weakly on the elements. So, the mean free path of electrons is denoted by  $\lambda_e = \lambda_e(E_{kin})$ . The binding energy of the electrons depends on the chemical state and is a fingerprint of a material. That is why the XPS spectrum is presented on binding energy scale. The kinetic energy of the emitted electron depends on the incident photon energy.

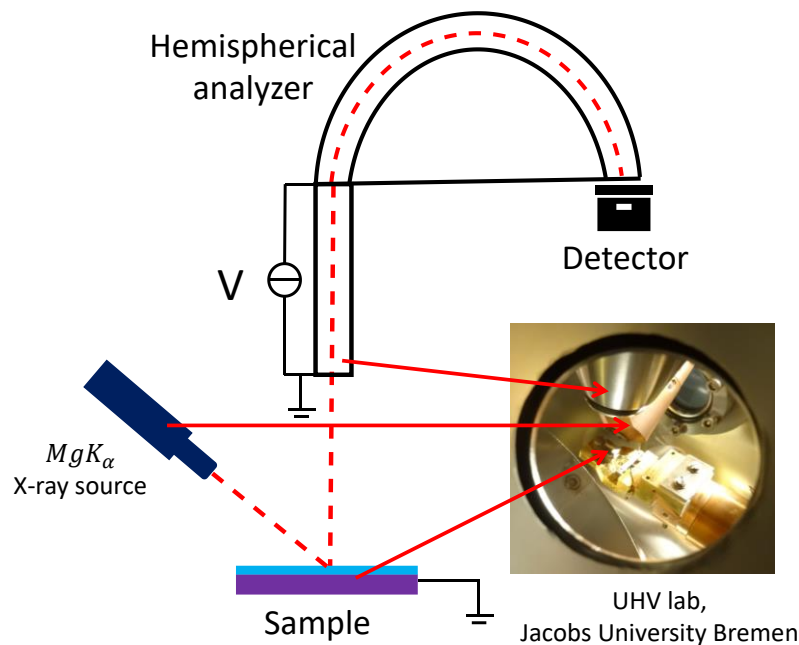


*Figure 1-9 Schematic illustration of X-ray photoelectron spectrometer.*

In photoelectron spectroscopy, the kinetic energy of ejected electrons is measured, and the number of the electrons is analyzed. Hemispherical electron analyzer is used to select electrons with specific energy. Since electrons are charged particles and heavily interact with material so XPS is surface sensitive. Only a few nm at the surface of the material can be analyzed due to the small mean free path  $\lambda_e$ . In order to avoid the interaction of the ejected electrons with the atmosphere, XPS measurements are performed in high vacuum ( $\sim 10^{-6}$  mbar). In this work, XPS measurements are done in an ultra-high vacuum ( $\sim 10^{-10}$  mbar). We can study all the elements with XPS except hydrogen and helium because they have extremely small cross-section or do not have 2 electrons. The binding energy of the

electron in an orbital depends on the atomic number of an element. As the numbers of the electrons in an atom changes, the difference between the energy shell and fermi energy also changes accordingly. The binding energy of an electron also depends on the chemical environment, i.e., an atom bonded to another atom or atoms. This chemical shift depends on the electronegativity of the atoms bonded. The valence electrons in a molecule are attracted more toward the atom having higher electronegativity. This phenomenon also effects the binding energy of the core electrons. Using this knowledge, we can identify different elements or compound by XPS. The relation between the atomic number and the binding energy is shown in the figure 1.10.

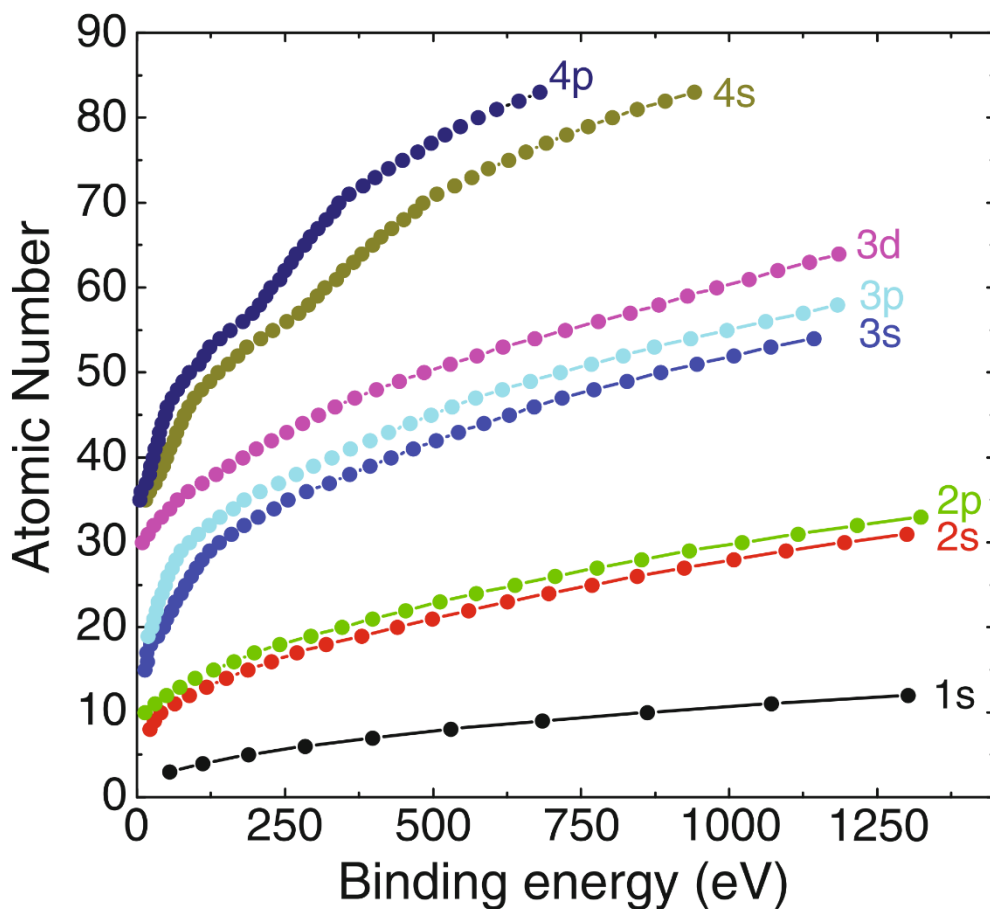


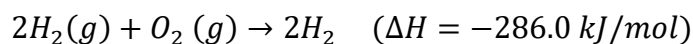
Figure 1-10 Plot of orbital binding energies versus atomic number [94]

#### 1.4. Hydrogen production and hydrogen evolution reaction (HER)

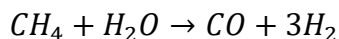
In order to overcome the problem of global warming, emission of the greenhouse gases needs to be reduced. For this purpose, fossil fuel must be replaced with green energy source. One of the potential candidates is  $H_2$  gas because of its high energy density.  $H_2$  gas does



not exist in appreciable concentration freely in the atmosphere or on the Earth. It must be extracted from other hydrogen containing compounds, i.e., water (H<sub>2</sub>O) or natural gas. Hydrogen is a potential fuel due to its high energy density. The burning of hydrogen gas is an exothermic chemical process. The chemical reaction of hydrogen burning is given as follows

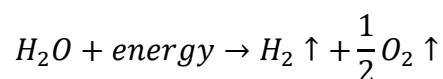


The above equation implies that 286 kJ energy is released when 1 mol of hydrogen and oxygen reacts with each other. Due to high energy density and low molecular weight, hydrogen has been consumed as fuel in many areas such as transportation and space vehicles since middle of 19<sup>th</sup> century. Currently established way to produce hydrogen gas is reforming of a natural gas. One of the final reaction products of the reforming of natural gas is hydrogen together with carbon dioxide and even carbon monoxide. Although this is a widely used way to produce hydrogen gas its drawback is, that fossil consumption is still involved in this process. The chemical reaction for reforming of natural gas is given below



An alternative way to generate hydrogen gas is water splitting. One of the most studied ways of H<sub>2</sub> production is electrolysis of water. In the process of the electrolysis of water, the water molecule is split into hydrogen and oxygen with no harmful byproduct. The electrolysis of water was first done Jan Rudolph Deiman Adriaan in 1789 using

electrostatic generator. In 1890, Charles Renard invented a water electrolysis unit to produce  $H_2$  gas as fuel for airships. In the 1960s, General Electric invented a proton exchange membrane for electricity production for the Gemini space program. Later it was used for electrolysis of water as well. In the simple electrolysis of water, electric energy is used to break the bond between hydrogen and oxygen. The electrolysis of water can be explained by the following chemical equation



The efficiency of the electrolysis of pure water is very small  $\sim 10^{-7}$  moles/liter due insulating nature of pure water. Therefore in our experiment  $H_2SO_4$  aqueous solution (pH=0) was used as an electrolyte. Acidic solution has positive and negative ions which makes that electrolyte a good conductor for electricity. The choice of electrodes is also important for high efficiency of electrolysis of water. The electrode should be a good electric conductor, have high surface area and be chemically, thermally and mechanically stable. In order to lower the overpotential and increase the efficiency, a suitable catalyst should be used. The three parameters defining a good catalyst for hydrogen evolution reaction are (i) Set-off potential (overpotential) (ii) current density (at the same set-off potential) (iii) Tafel slope. Reduction/oxidation (redox) reaction takes place in electrochemical cell when electric current is passing through the cell. Redox reaction causes current to flow in the electrochemical cell. For this current to flow, an additional voltage is required together with thermodynamically determined potential (theoretically predicted) to cause redox

28

reaction. The additional voltage is called overpotential. In the process of electrolysis, exchange of electrons occur at the electrodes (oxidation: loss of electrons, reduction: gain of electrons). Electrolysis requires a decomposition voltage. The difference between decomposition voltage and the reduction potential (theoretically predicted) is known as overpotential. Decomposition of water molecule is a 4-electron process with dissociation energy of 1.23 eV per electron [29]. The energy bands of the catalytic material should be aligned in such a way that valence band maximum is close to OER potential (see figure 1.11) while conduction band minimum is close to HER potential. A catalytic material makes this process thermodynamically more favorable. A high-quality catalyst possesses low overpotential, high current density and a low Tafel slope. Tafel slope is extracted from polarization curve. It shows the increase of electrochemical reaction rate with respect to overpotential by factor of ten. The current state of the art catalyst for hydrogen evolution reaction is platinum. Generally metals from Pt group (Pt, Ir, Pd, Rh [30]) are reported to possess highest HER activity. Pt is widely used as a catalytic electrode for HER. The reported Tafel slope for Pt is 30 mV/decade [30]. But application of Pt for HER is limited due to its low abundance and high cost. Therefore, researchers are constantly looking for cheap, globally abundant, and good catalyst material for HER.

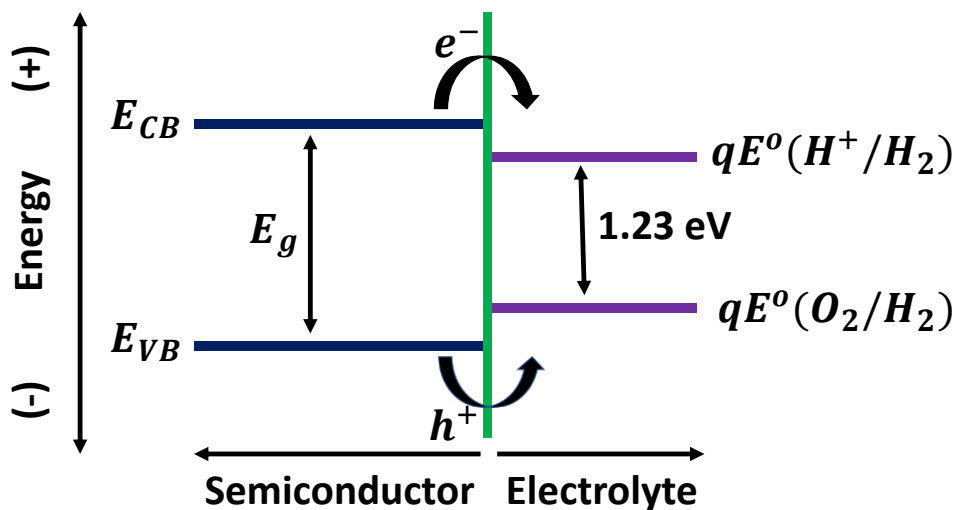


Figure 1-11 Energy scheme of hydrogen evolution reaction (HER) and oxygen evolution reaction (OER).

Recent theoretical and experimental studies show that 2D MoS<sub>2</sub> is a good catalyst for hydrogen evolution reaction. In 1977, first MoS<sub>2</sub> HER activity was reported [31]. MoS<sub>2</sub> nanoparticles perform better than bulk MoS<sub>2</sub> [19]. A reported study in 2007 shows that edge sites of MoS<sub>2</sub> act as active sites for HER [4]. One of the ways to improve catalytic activity of MoS<sub>2</sub> is to grow MoS<sub>2</sub> with small particles in order to get more active edge sites. S-vacancies also act as active sites for HER [24]. In this approach, MoS<sub>2</sub> layers are deposited by solution-based processes, i.e. electrochemical deposition and spin-coating.

## Chapter 2

### 2. Growth of ultra-thin large sized 2D flakes at air-liquid interface to obtain 2D-WS<sub>2</sub> monolayers

This work is published in Journal of Physics D: Applied Physics.

DOI: <https://doi.org/10.1088/1361-6463/abc198>

#### 2.1.Introduction

The discovery of 2-dimensional (2D) graphene has opened a complete new research area [32]. Unlike conducting graphene, transition metal dichalcogenides (TMDs) such as MoS<sub>2</sub> and WS<sub>2</sub> exhibit a well-defined bandgap with values ranging from 1-2 eV [10], [33], [34]. These materials are potential candidate for future electronics due to their 2D nature. The transition metal ion is sandwiched between two chalcogen atoms forming a honeycomb crystal structure extending into a 2D sheet. Among other TMDs, WS<sub>2</sub> is a promising candidate because of its non-zero bandgap that allows to fabricate high performance nano-devices such as thin-film field effect transistors, photoactive cells and spintronic devices [11], [12], [22]. WS<sub>2</sub> monolayer has been deposited by various deposition methods such as atomic layer deposition [18], pulsed laser deposition technique [35], chemical vapor deposition [22]. Similarly, WS<sub>2</sub> nanostructure/nanosheets have also been grown by solution based processes such as chemical exfoliation [36], liquid-phase sonication [37], hydrothermal synthesis [38] and Liquid-phase precursor mixing [39]. By now chemical vapor deposition and atomic layer deposition are well-established methods, but they require expensive instrumentation, high temperature and vacuum. Furthermore, for the latter methods the WS<sub>2</sub> grain size strongly depends on the substrate used [40],[41], which puts limitations for large scale production of WS<sub>2</sub> thin film devices. An alternative simple wet chemical deposition method is presented here for the growth of 2D flakes from aqueous

solution below 100 °C. This growth mode is similar to the previously reported growth of large area MoS<sub>2</sub> flakes [26]. Post-annealing of the initially obtained WO<sub>3</sub> flakes results in ultra-thin WS<sub>2</sub> flakes. This wet chemical deposition process has several advantages such as (i) the use of non-expensive and non-toxic precursor materials, (ii) it can be performed on a large scale, and (iii) it is compatible with a wide range of substrates. In this work, WS<sub>2</sub> flakes are obtained from a solution-based process. Initially WO<sub>3</sub> flakes are grown at air-liquid interface as result of thermal decomposition of precursor below 100 °C. This solution-based process has advantage over CVD and ALD process because in CVD and ALD process, the deposition of precursor requires high temperature, vacuum processing and plasma treatment. The precursor flakes are formed at the liquid-air interface and transferred to a silicon wafer by a controlled dip-coating process. To our knowledge this is the first time that the growth of large precursor flakes is reported at the air-liquid interface to obtain WS<sub>2</sub> flakes. The transferred precursor flakes are post-annealed in an inert environment to convert them to WS<sub>2</sub>. The precursor solution and the flakes were characterized by various methods, i.e. Raman, XPS, and UV-Vis spectroscopy as well as atomic force microscopy.

## **2.2.Methodology**

### **2.2.1. Sample preparation and dip-coating**

Silicon wafers covered with 270 nm SiO<sub>2</sub> were used in this experiment as substrates. The wafers were cleaned with acetone and isopropanol. Thereafter the wafers were rinsed with DI-water, dried with a nitrogen gun and heated at 120 °C for 5 minutes to evaporate remaining solvents. After cleaning the wafer, they were treated with UV-ozone to remove any remaining organic contaminations. Afterwards, ammonium tetrathiotungstate ((NH<sub>4</sub>)<sub>2</sub>WS<sub>4</sub>, ATTW) was dissolved in DI-water and a 5 mM aqueous precursor solution was prepared. The precursor solution was ultra-sonicated for 15 minutes in order to obtain a uniform solution and dispersed ATTW in the solvent. The precursor material ATTW

(purity 99.9 %) was bought from Sigma-Aldrich. No flakes were observed at the air-liquid interface at room temperature even after a week of storage. When the ATTW precursor solution was heated to 70-90 °C, formation of the flakes was observed at the air-liquid interface. These flakes were transferred from the air-liquid interface to a Si/SiO<sub>2</sub> substrate by means of controlled dip-coating with a withdrawal speed of 1 mm s<sup>-1</sup>. The transferred flakes were heated at 120 °C for 20 minutes in order to evaporate remaining water from the surface.

### **2.2.2. Conversion of dip-coated flakes to WS<sub>2</sub>**

The samples were post annealed at high temperature (500-900 °C). For this purpose, the samples were kept in the middle of a quartz tube which was put in a furnace. Pure sulfur in a quartz crucible was placed in the upstream near the edge of the furnace. Then argon gas with 5% H<sub>2</sub> was used to flush with a high rate for 3 minutes to remove residual air. After purging, the gas flow rate was reduced to 50 sccm. The temperature of the furnace was gradually increased to the target temperature (500-900 °C) at a ramp speed of 20 °C/min. The samples were kept at the target temperature for 120 minutes before cooling down to room temperature. The complete experimental process is illustrated in Figure 2.1.

### **2.2.3. Characterization of precursor and flakes**

To determine the mechanism of flake formation at the air-liquid interface, the solution was kept at 70 °C, 80 °C and 90 °C for a few hours. UV-Vis measurements of a small part extracted from the solution were done after every 15 minutes. The UV-Vis measurements of the solution were performed on a Cary 5000 UV-Vis-NIR spectrometer in the spectral range from 200 to 1100 nm. Raman measurements of the flakes from the air-liquid interface and from the bottom of the solution were excited by a laser at 514 nm. The signal was received with a 50x objective. The scattered light was dispersed with a 2400 g/mm grating and detected by a liquid nitrogen cooled charged-coupled device (CCD) detector (Horiba

Jobin-Yvon T64000 system). The IR measurements were done on the flakes from the air-liquid interface and from the bottom of the solution. In order to do IR measurements, the flakes were filtered by a filter paper and mixed with KBr in a 1:99 ratio. To make fine pellets for IR analysis, the mixture was pressed hydraulically and the IR measurements were done in transmission mode in nitrogen environment. In order to do X-ray photoelectron spectroscopy (XPS) on the flakes, the flakes were transferred to a gold-covered silicon wafer and introduced into a XPS chamber equipped with a photoelectron spectrometer with a hemispherical analyzer (Specs-Phoebos 100) and a Mg/Al X-ray gun (Specs XR-50). The Analyzer was used (in transmission mode) with a pass energy of 50 eV. The Mg  $K\alpha$  radiation source was used for excitation. The CASA XPS<sup>TM</sup> program was used for the evaluation of the XPS data and the background was subtracted using Shirley's method. After post-annealing, the samples were again characterized by Raman and XPS spectroscopy in order to confirm the conversion of the precursor flakes to WS<sub>2</sub>. The thickness of the flakes was measured by atomic force microscope (AFM) (Nanosurf).

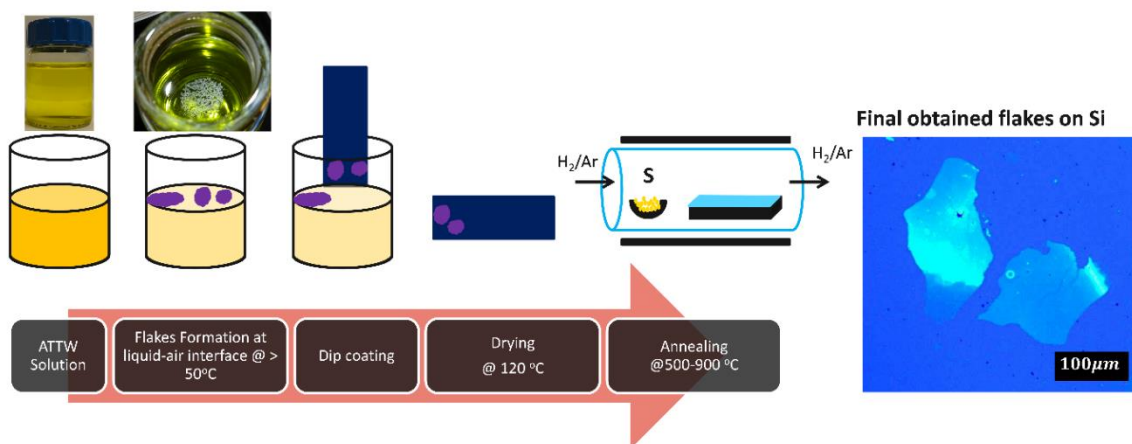


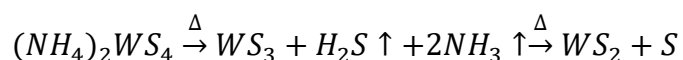
*Figure 2-1 Schematic illustration of the flake formation at the air-liquid interface, dip-coating process, and post annealing.*



## **2.3.Results and discussion**

### **2.3.1. Mechanism behind flake formation**

An aqueous solution of ATTW is stable at room temperature. In an inert environment such as N<sub>2</sub> or Ar the thermal decomposition of ATTW occurs at temperature between 170 and 280 °C and results in a conversion to WS<sub>3</sub>, H<sub>2</sub>S and 2NH<sub>3</sub> [42]. The obtained WS<sub>3</sub> further reduces to WS<sub>2</sub> if it is kept at a temperature between 280 and 330 °C. The chemical reaction that occurs during thermal decomposition is given as follows:



#### **2.3.1.1. Flakes formation at the air-liquid interface**

In this work, the ATTW is dissolved / dispersed in deionized water. The aqueous solution of ATTW is stable under normal atmosphere and at room temperature and no flakes are formed at the air-liquid interface or at the bottom. However, when the ATTW solution is kept at 70 – 90 °C flakes are observed at the air-liquid interface after a few hours. Since the formed flakes are large and located at the surface of the liquid, any external vibration could break the flakes into smaller pieces. On a vibrationally isolated optical bench this risk is minimized. The absorbers of the used bench have a resonance frequency of 1 Hz and absorb all vibrations with higher frequencies. The flakes transferred to a silicon wafer are shown in Figure 2.1.

#### **2.3.1.2. UV-Vis spectroscopy**

To determine the chemical process behind of the formation of the flakes, UV-Vis measurements of a small part extracted from the ATTW solution (70-90 °C) were performed every 15 minutes continuously for several hours. In the beginning, the colour of the solution was dark-yellow and gradually became lighter until it was completely

transparent, as shown in the Figure 2.2b. In the UV-Vis spectrum, three excitonic peaks are visible at 216, 277 and 393 nm (as shown in 2.2a), which are attributed to the tetrahedral ion  $WS_4^{2-}$  [43]. The intensity of the  $WS_4^{2-}$  peaks gradually decreased at different rates for the different temperatures of the solution, as shown in Figure 2.2b. The  $WS_4^{2-}$  peaks almost disappeared which is in good agreement with the colour of the solution. This indicates that ATTW in solution decomposes and turns into flakes at 70, 80 and 90 °C, which appear at the air-liquid interface as shown in Figure 2.1.

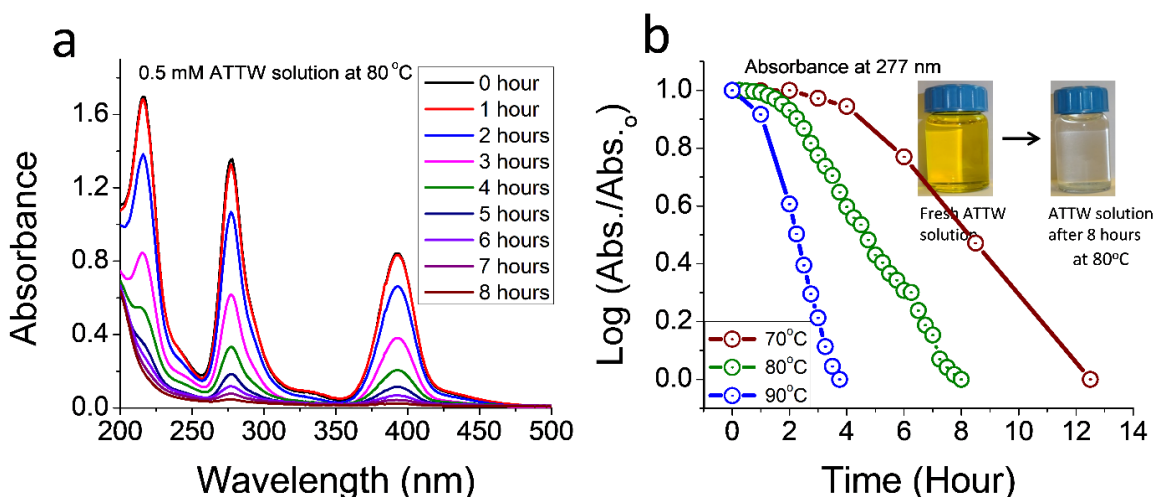


Figure 2-2 Time dependent UV-Vis spectra of the 0.5 mM ATTW solution kept at 70-90 °C.

### 2.3.1.3. Raman spectroscopy

In Figure 2.3 Raman spectra are shown of a flake from the air-liquid interface after two hours and a flake from the bottom of the liquid after 8 hours grown at 80 °C together with pure references (ATTW and WO<sub>3</sub>). In the Raman spectrum of a flake from the air-liquid

interface after 2 hours, six peaks are visible at 803, 712, 482, 325, 267, and 130 cm<sup>-1</sup> in the measured spectral range. Out of the six peaks, five (803, 712, 325, 267, and 130 cm<sup>-1</sup>) are attributed to the Raman-active modes of WO<sub>3</sub> [44]. On the other hand, the peak at 482 cm<sup>-1</sup> is attributed to ATTW [45]. A literature report [44] assigns the former vibrational modes to symmetric stretching of O-W-O bonds, asymmetric stretching of W-O-W bonds, O-W-O deformation, W-O stretching and W-O bending modes of WO<sub>3</sub>, respectively. The peak at 482 cm<sup>-1</sup> is attributed to the symmetric stretching mode ( $\nu_1$ ) of the terminal tungsten-sulfur (W=S) bonds in  $WS_4^{2-}$ . So, the flakes of the air-liquid interface are mainly composed of WO<sub>3</sub> and a small residual of ATTW precursor is also present in the flakes. In the Raman spectrum of the flakes from the bottom of the liquid after 8 hours, all typical peaks of WO<sub>3</sub> are observed which indicated that these flakes are also mainly composed of WO<sub>3</sub>. In addition to the WO<sub>3</sub> peaks, minor peaks of ATTW are also visible, but they are weaker when compared to the Raman spectrum of the flakes from the air-liquid interface. This indicates that the amount of ATTW residual is further reduced in the flakes with the passage of time. In the Raman spectrum of the pure WO<sub>3</sub> reference, five typical Raman-active modes of WO<sub>3</sub> are visible at 803, 712, 325, 267, and 130 cm<sup>-1</sup> in the measured spectral range. These peaks are attributed to the Raman active modes of WO<sub>3</sub> as described above. In the Raman spectrum of pure ATTW, four typical Raman-active modes of  $WS_4^{2-}$  are observed at 482, and 457 cm<sup>-1</sup> as well as two broader peaks at 176 cm<sup>-1</sup>. The peak at 457 cm<sup>-1</sup> corresponds to the triply degenerate asymmetric stretching mode ( $\nu_3$ ) of the tungsten-sulfur (W=S) bond. The peak at 482 cm<sup>-1</sup> is attributed to the symmetric stretching mode ( $\nu_1$ ) of tungsten-sulfur (W=S) bond. The broad peaks at 176 cm<sup>-1</sup> are indicative for the degenerate vibrational modes ( $\nu_2, \nu_4$ ).

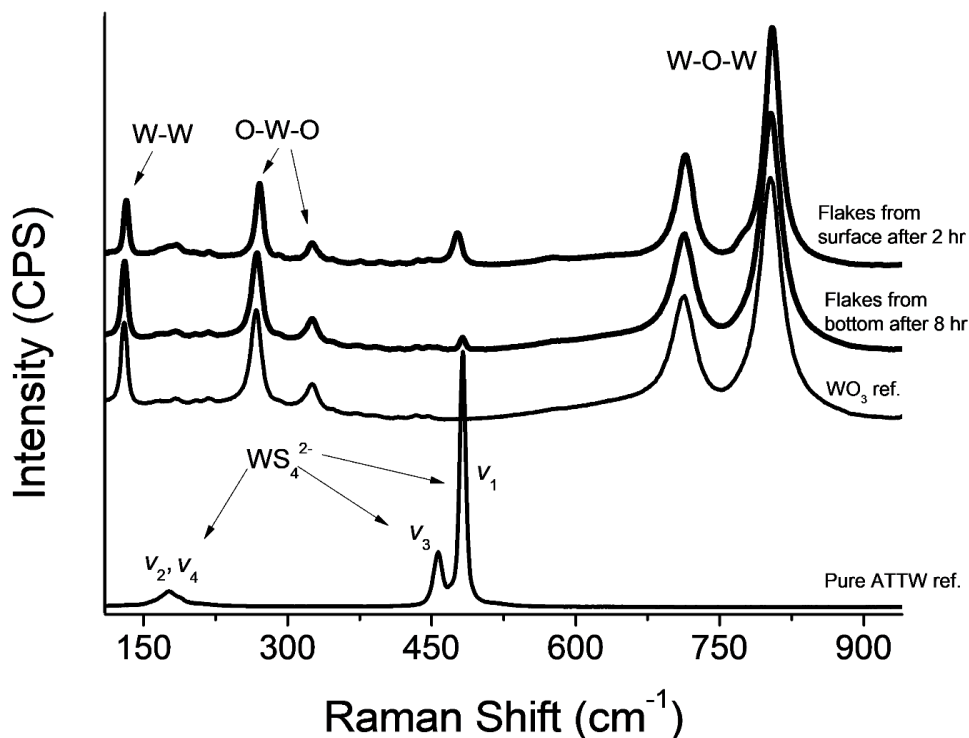


Figure 2-3 Raman spectra of a flake from the air-liquid interface, a flake from the bottom of the liquid (80 °C sample) and pure references (WO<sub>3</sub> and ATTW).

#### 2.3.1.4. Infra-red spectroscopy

Similarly, the flakes and pure references (WO<sub>3</sub> and ATTW precursor) were further characterized by means of infra-red (IR) spectroscopy. All IR spectra (Figure 2.4) exhibit broad bands at 3465 and 1615 cm<sup>-1</sup>, which are attributed to the O-H stretching mode and O-H-O symmetric bending mode of H<sub>2</sub>O, respectively [46]. In the IR spectrum of the flakes obtained after 8 hours, the bands in the range of 500-1000 cm<sup>-1</sup> are attributed to the W-O vibrational modes of WO<sub>3</sub> [44]. The bands are associated with the W-O-W and W-O

stretching modes, respectively. This also indicates that the obtained flakes are mainly composed of WO<sub>3</sub>, which is consistent with the Raman results. The IR spectrum of the WO<sub>3</sub> reference is shown in Figure 2.4. The typical bands of WO<sub>3</sub> are visible in the spectrum as described above. Similarly, the IR spectrum of the pure precursor ATTW exhibits bands at 1382 and 455 cm<sup>-1</sup>. A strong band at 455 cm<sup>-1</sup> is attributed to the asymmetric stretching mode (W=S bonds) of the WS<sub>4</sub><sup>2-</sup> ion [45]. The band at 1382 cm<sup>-1</sup> corresponds to the vibrational mode of the ammonium ion. The ATTW precursor decomposes to H<sub>2</sub>S↑, WS<sub>3</sub> and 2NH<sub>3</sub>↑. The WS<sub>3</sub> then reacts in aqueous solution with water to form WO<sub>3</sub> and

H<sub>2</sub>S↑. The balanced chemical reactions are given below and they are consistent with Raman, IR and XPS results.

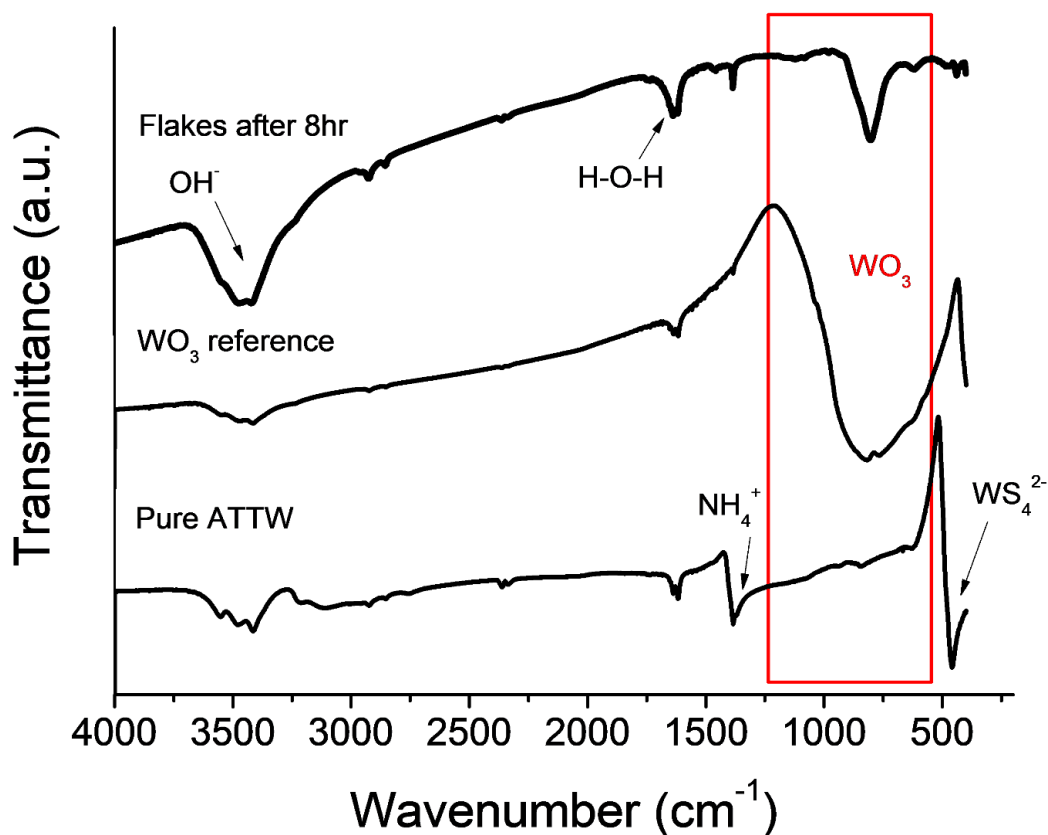
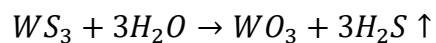
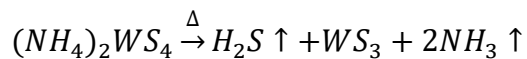
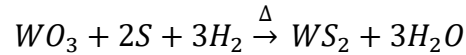


Figure 2-4 IR spectra of the flakes after 8 hours, WO<sub>3</sub> as reference and ATTW as reference.

### 2.3.2. Conversion of Flake to WS<sub>2</sub>, size , thickness of obtained flakes

#### 2.3.2.1. Raman spectroscopy

A post-annealing step was performed to convert the initial WO<sub>3</sub> flakes to WS<sub>2</sub>. The annealed flakes were characterized again by Raman spectroscopy. In Figure 2.5, the Raman spectrum of a flake annealed at 800 °C is shown. Two intense peaks at 356 and 418 cm<sup>-1</sup> are observed, which are attributed to the first order Raman-active modes  $E_{2g}^1$  and  $A_g^1$  of WS<sub>2</sub>, respectively [47]. In addition, two other broad peaks at around 308 and 680 cm<sup>-1</sup> are visible that correspond to the higher-order longitudinal acoustic modes 2LA and 4LA, respectively. Thus, the Raman result confirms the formation of WS<sub>2</sub> after post-annealing. Post-annealing temperature dependent Raman measurements show that crystallinity of the obtained WS<sub>2</sub> flakes improves with increasing temperature. The full-width at half maximum (FWHM) of the Raman peaks is small for post-annealing at high temperatures and large for low post-annealing temperatures (see figure. 2.6). This reduction of FWHM with increasing temperature shows the improvement of crystallinity of the obtained WS<sub>2</sub> flakes. The measured FWHM (8.3 cm<sup>-1</sup>) of the Raman active  $A_{1g}$  mode of obtained WS<sub>2</sub> flakes at 900 °C is similar to the reported WS<sub>2</sub> flakes grown by CVD and ALD [48], [18], [49], [50]. The chemical reaction for the conversion of the precursor flakes to WS<sub>2</sub> is given below



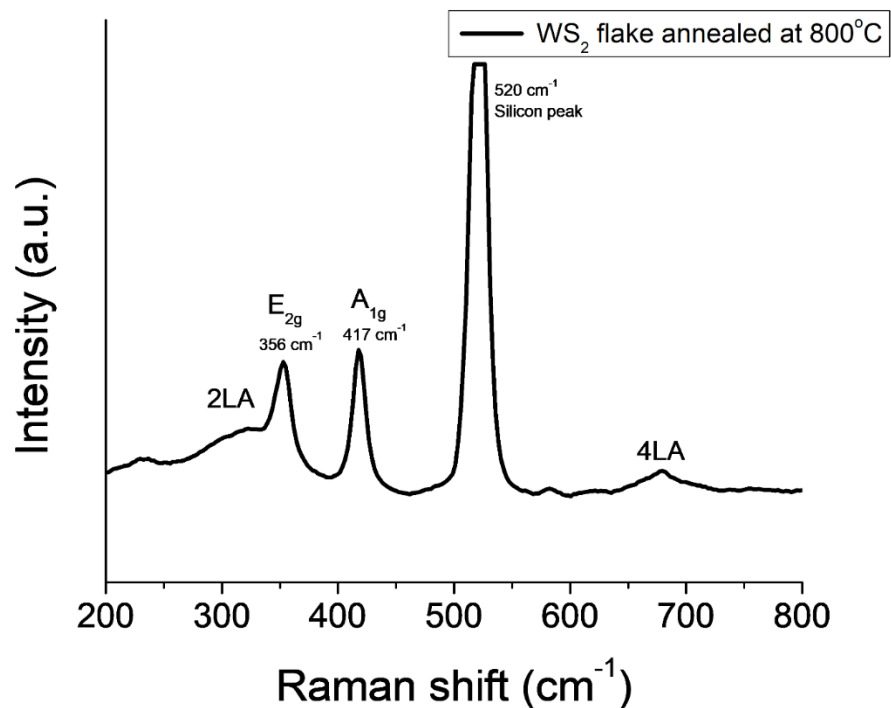


Figure 2-5 Raman spectrum of a post-annealed flake at 800 °C.

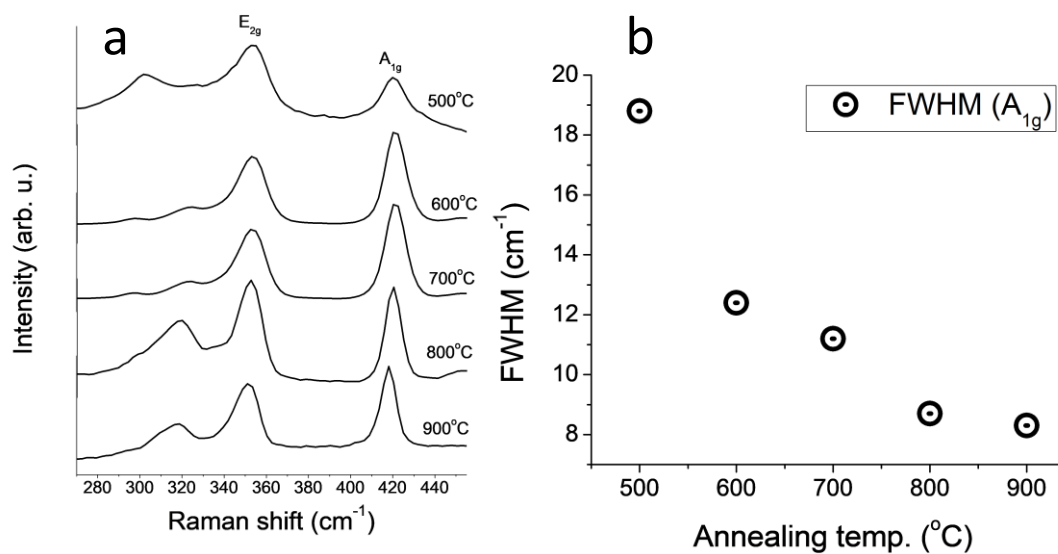


Figure 2-6 Raman measurement done at different post-annealing temperatures (500-900°C). b) Plot of FWHM against post-annealing temperature.



### 2.3.2.2. X-ray photoelectron spectroscopy

In Figure 2.7, the photoelectron spectra and peak fits for the W 4f<sub>5/2</sub> and 4f<sub>7/2</sub> doublet of the flakes before and after annealing together with pure ATTW as reference are shown. The spectrum of the flakes exhibits a doublet with binding energies of 38.3 and 35.9 eV for the W 4f<sub>5/2</sub> and 4f<sub>7/2</sub> components, respectively, which corresponds to the peak positions for WO<sub>3</sub> [51]. This indicates that the flakes are comprised of mainly WO<sub>3</sub>, which is consistent with the Raman and IR results. For comparison, XPS measurements were also performed on pure ATTW and the spectrum consists of a doublet with binding energies of 37.2 and 35.3 eV for the W 4f<sub>5/2</sub> and W 4f<sub>7/2</sub>, respectively. XPS measurements were also performed after annealing at 800 °C. Such XPS spectrum mainly consists of a doublet with binding energies of 36.8 and 34.6 eV for the W 4f<sub>5/2</sub> and W 4f<sub>7/2</sub>, respectively, which suggests WS<sub>2</sub> formation. The atomic ratio between W and S is found to be 1:2.1, which is close to the ideal ratio in WS<sub>2</sub>. Hence the flakes annealed at 800 °C with an additional sulfur source in an inert environment are converted to WS<sub>2</sub>.

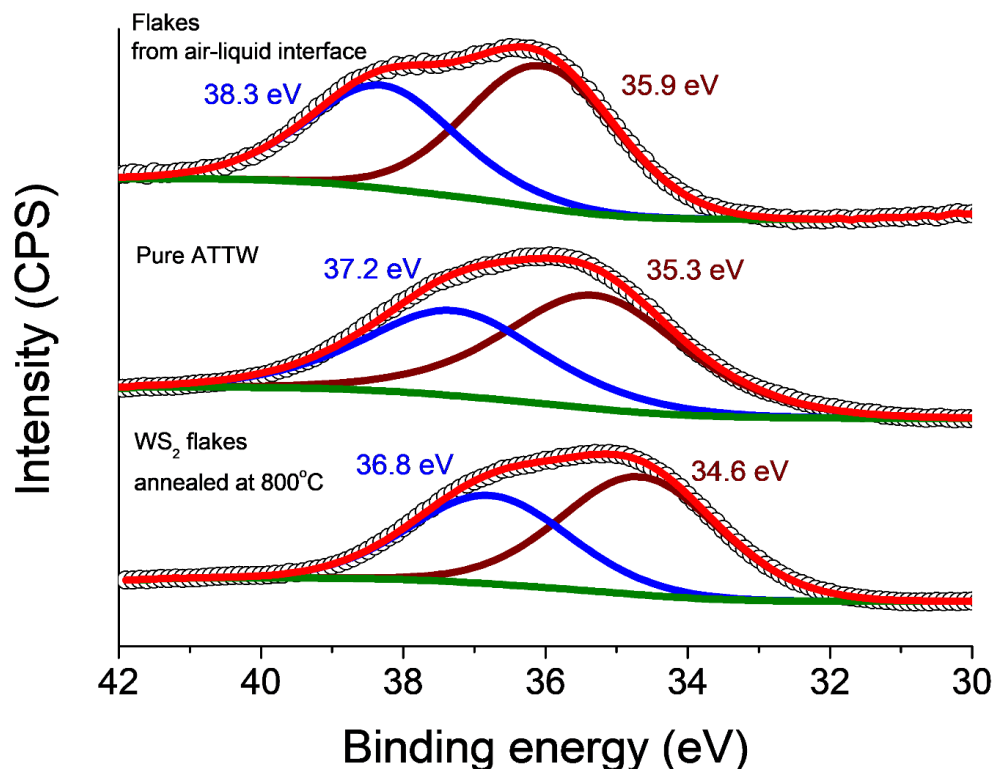


Figure 2-7 X-ray photoelectron spectra ( $W_{4f}$ ) of flakes before and after annealing at 800 °C and pure ATTW reference.

### 2.3.2.3. Atomic force microscopy and optical microscopy

The thickness of the flakes was measured by atomic force microscope. The thickness of the thinnest flake was found to be equivalent to a monolayer (0.85 nm) of WS<sub>2</sub> as shown in Figure 2.8. The minor difference between the thickness of the measured WS<sub>2</sub> monolayer and the intrinsic thickness (0.7 nm) of the WS<sub>2</sub> monolayer is attributed to surface adsorbates and the roughness of the underlying silicon wafer.

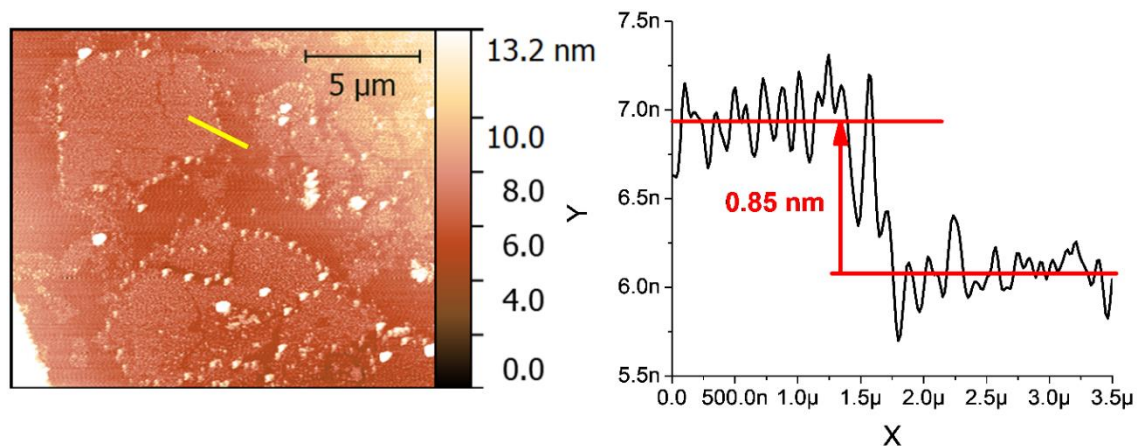


Figure 2-8 Atomic force microscope image (left) and thickness profile of the edge (right) of a WS<sub>2</sub> monolayer flake.

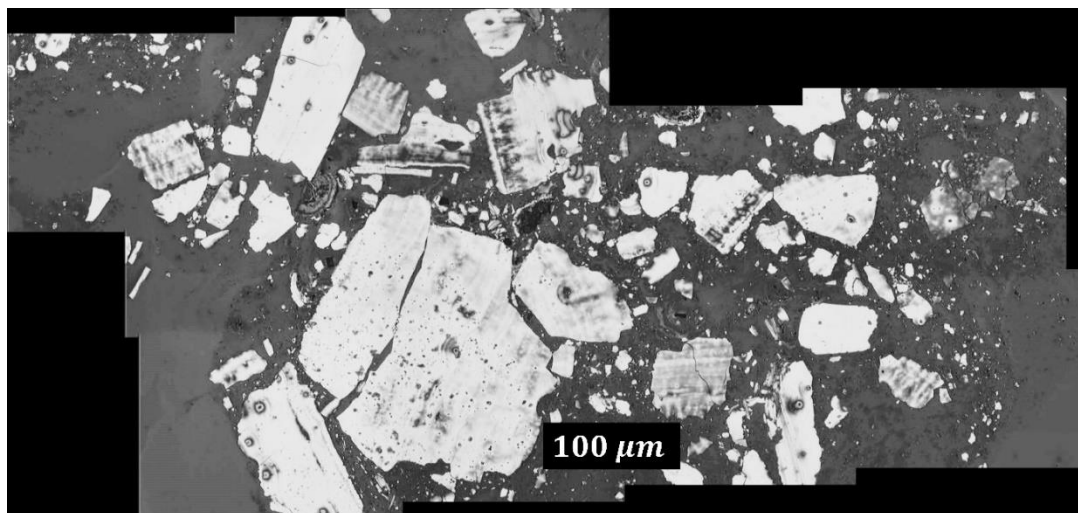


Figure 2-9 Optical microscope image of WS<sub>2</sub> flakes on a silicon wafer. Several images are stitched together to obtain a larger visible area.

The lateral size flake in figure 2 is over 100  $\mu\text{m}$ . Surface of the substrate is densely covered with the flakes. If we look at the biggest flake in the figure 2.9, It seems like the initially grown flake is broken and divided into two flakes. Similarly, cracks can be seen in many other flakes. Although the precursor solution was kept on vibrationally isolated optical bench to avoid damages in the flakes yet cracks or damages occurred in the flakes. These cracks in the flakes might occurred during the lifting process in the dip coating step.

### **2.4. Conclusion**

WS<sub>2</sub> precursor flakes were obtained from an aqueous precursor solution for the first time. An aqueous solution of ATTW was used for this purpose. The precursor solution was found to be stable at room temperature. The flake formation at the air-liquid interface takes place at 70-90 °C after a few hours. This shows that the activation energy is crucial for the formation of the flakes. The flakes were successfully transferred to a silicon substrate from the air-liquid interface by means of controlled dip-coating. Raman, IR and XPS results show that the flakes initially consist of WO<sub>3</sub> and small residual amount of ATTW. The transferred precursor flakes were successfully converted to WS<sub>2</sub> by a post annealing process with an additional sulfur source in an inert environment. The largest obtained flake had lateral size exceeding 100  $\mu\text{m}$  and the thickness of the thinnest flake was found to be 0.85 nm which is equivalent to the monolayer of WS<sub>2</sub>.

## Chapter 3

### 3. Mechanical transfer of electrodeposited MoS<sub>2</sub> films to silicon wafer

This work is submitted to Journal of Applied Electrochemistry (December 2020)

#### 3.1.Introduction

After discovery of graphene as an atomically thin two-dimensional (2D) material [32], a complete new research area has been opened. Recently, 2D semi-conducting materials analogue to graphene, i.e. transition metal dichalcogenides (TMDCs), have attracted great attention due to their interesting optical and electronic properties and 2D nature. Among other 2D TMDCs, molybdenum disulfide (MoS<sub>2</sub>) exhibits a non-zero band-gap, unlike conducting graphene, and it has interesting properties such as a tunable bandgap [52], optoelectronics [53], and spin-orbit coupling effects [54]. It can be used in switching devices such as a field effect transistor and in hydrogen evolution reaction because of its suitable band-structure [8], [28]. TMDCs thin films have been deposited by various deposition methods such as pulsed laser deposition [35], chemical vapor deposition (CVD) [55], [9], mechanical exfoliation [8], liquid-phase exfoliation [27], dip-coating [26], [56] and spin-coating [25]. Fabrication of transistor is also reported by solution based process such as spin-coating and liquid-phase exfoliation [27], [57]. However, a major challenge is to grow MoS<sub>2</sub> ultra-thin films on large scale and transferring those films to a desired substrate for different applications and characterization while preserving the quality of the films. In this work ultra-thin films of MoS<sub>2</sub> have been grown electrochemically on a Au-substrate and transferred onto a silicon substrate by mechanical transfer method followed by gold etching. Such mechanical transfer method while the MoS<sub>2</sub> film is supported by a Poly methyl methacrylate (PMMA) layer was recently reported [58], which is an

alternative transfer method to chemical etching of the substrate. For chemical etching of the substrate, usually toxic etchants are used such as hydrofluoric acid (HF) for etching of SiO<sub>2</sub> [59]. In order to avoid toxic etchants for transfer, the environmental friendly transfer method has been used in our approach. The MoS<sub>2</sub> films are mechanically separated by ultra-sonication from the silicon substrate along with Au layer because of its weak adhesion to the oxidized silicon surface. The Au layer is removed by a non-toxic gold-etchant such as potassium iodide. This mechanical transfer followed by gold etching doesn't harm the MoS<sub>2</sub> film and the underlying substrate can be reused. The obtained films have been characterized by various spectroscopic methods, i.e., Raman, UV-Vis and XPS before and after transfer.

### **3.2.Methodology**

#### **3.2.1. Electrochemical growth of MoS<sub>x</sub>**

Ammonium tetrathiomolybdate ((NH<sub>4</sub>)<sub>2</sub>MoS<sub>4</sub>, ATTM) was dissolved in di-ionized (DI) water in order to prepare 1 mM precursor solution for the electrodeposition. The aqueous solution of the precursor was ultra-sonicated for 20 minutes to get a uniform solution. Silicon wafers were cleaned with acetone and isopropanol and dried with nitrogen. Afterwards the wafers were treated with UV-ozone for 10 minutes to remove organic contaminations. A 50 nm gold layer was deposited on the silicon wafers by e-beam evaporation. However, any standard deposited method can be used to deposit Au thin film such as physical vapor deposition or sputter coating. After preparing electrolyte and substrates for electrodeposition, the electrochemical setup was prepared. The Potentiostat consists of three electrodes: counter electrode (Pt), working electrode (Au deposited on a silicon wafer) and reference electrode (calomel electrode). The reduction potential of the calomel electrode is 0.27 V, which is referenced to standard hydrogen electrode at room temperature. The over-voltage was kept constant at 0.38V and deposition time was varied

48

in order to get films with different thicknesses. The electrochemical setup is illustrated in figure 3.1. ATTM is a single source Mo-precursor with the molybdate ion surrounded by sulfur as main source of MoS<sub>2</sub>. After electrodeposition, the samples were pre-annealed at 120 °C for 15 minutes to evaporate remaining solvent.

### **3.2.2. Transfer of grown films to silicon wafer**

Poly methyl methacrylate (*PMMA*) (4 wt%) material was dissolved in methyl ethyl ketone (MEK) solvent and stirred overnight. The PMMA solution was spin-coated on the electrochemically deposited MoS<sub>x</sub> film at 1000 rpm for 60 sec. It was afterwards annealed at 150 °C for 20 minutes. The polymer coated electrodeposited film on Au/SiO<sub>2</sub>/Si was then ultra-sonicated (Bandelen RK-100-H (35 kHz) for 1 min. Ultra-sonication causes the PMMA/MoS<sub>x</sub>/Au stack to separate from the silicon wafer and to float on the surface of the DI-water. The floating PMMA/MoS<sub>x</sub>/Au layer stack was then transferred from DI-water to a gold etching solution (K/KI) in order to etch the Au layer. Undiluted standard gold etchant (651818) was used and was bought from sigma-aldrich. After etching the gold, the PMMA/MoS<sub>x</sub> layer stack was picked up with a cleaned silicon wafer with highly hydrophilic surface and annealed at 120 °C for 30 minutes. Finally, the PMMA layer was removed with acetone. This way the MoS<sub>x</sub> layer was successfully transferred from the conducting Au substrate to a silicon wafer.

### **3.2.3. Conversion of electrodeposited films to MoS<sub>2</sub>**

The transferred MoS<sub>x</sub> sample was then annealed at target temperature (450, 500, 600, 700, 800, 900 °C) with a heating rate of 20 °C/min and with an additional sulfur source in inert 95% Ar and 5% H<sub>2</sub> atmosphere. For this purpose, the sample was placed in the middle of a quartz tube and pure sulfur was placed in the upstream near the edge. The quartz tube was then placed in an oven. Initially the flow of Ar/H<sub>2</sub> was kept high to remove residual

air. The target temperature was maintained for 120 minutes. The complete sequence of the experiment is illustrated in figure 3.1.

### 3.2.4. Characterization methods

The electrodeposited films and the films after transfer were characterized with different spectroscopic techniques to study the surface morphology, composition of the film and crystal quality. Atomic force microscope (AFM) (Nanosurf) was used in tapping mode to analyze surface morphology and uniformity of the films. The thickness of the films is measured by a Dektak profilometer. UV-Vis spectroscopy (Cary 5000 UV Vis – NIR Spectrometer) was done in a spectral range from 200 to 1100 nm in order to observe the excitonic finger print of MoS<sub>2</sub>. For UV-Vis measurements, an electrochemically deposited film was transferred to a quartz substrate before and after post-annealing. Raman measurements (Horiba Jobin-Yvon T64000) were carried out using 514.5 nm laser excitation source in order to identify the chemical structure based on unique molecular bond vibration and to analyze the crystallinity from the width of the peaks. The Raman signal was collected by a 50x objective and dispersed with 2400 lines/mm grating and detected by a CCD (charge coupled device) detector at -110 °C (cooled by liquid nitrogen). In order to do x-ray photoelectron spectroscopy (XPS), the samples were introduced to the XPS vacuum vessel, which has a photoelectron spectrometer with a hemispherical analyzer (Specs Phoebos 100) and a Mg/Al X-ray gun (Specs XR-50). The analyzer was used in transmission mode with a pass energy of 50 eV and Mg K<sub>α</sub> radiation (E=1253.6 eV) was used as source of excitation. The XPS data evaluation was done with the CASA XPS<sup>TM</sup> software and Shirley method was used to subtract the background. The minor shift in the binding energy because of charging was corrected with respect to the C<sub>1s</sub> peak.



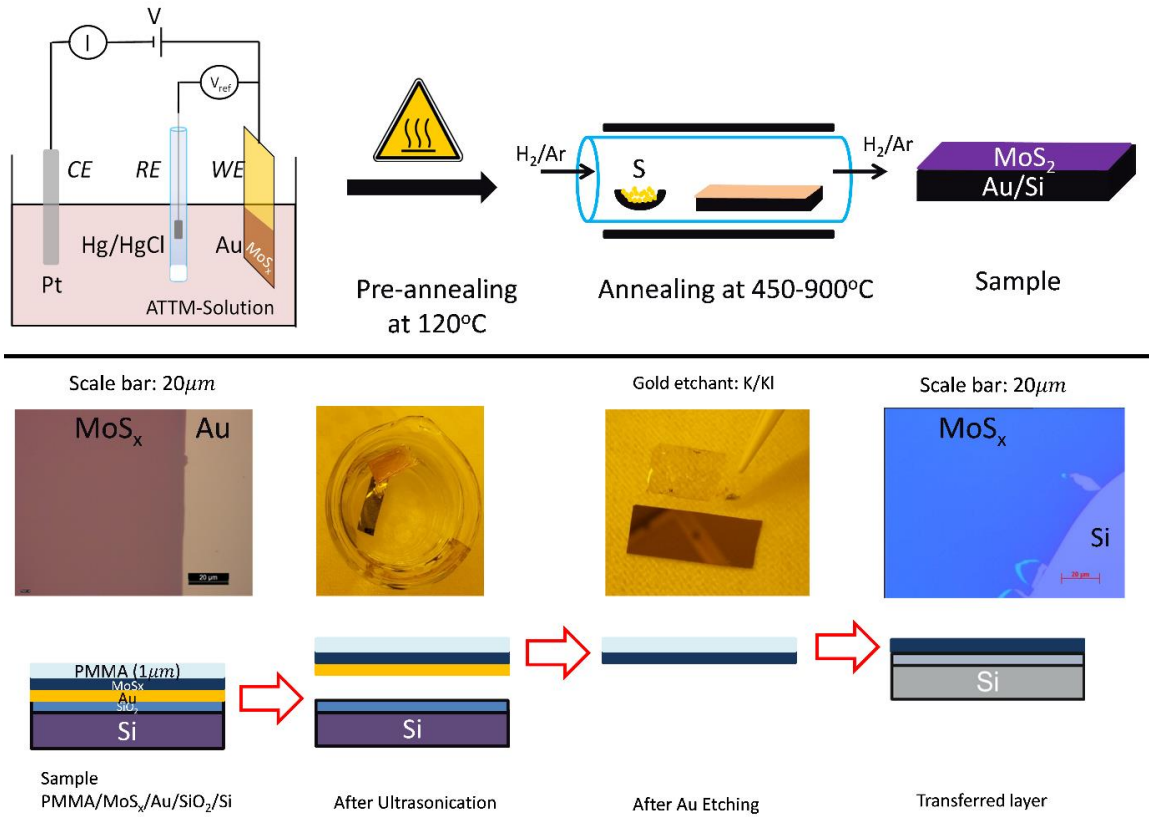


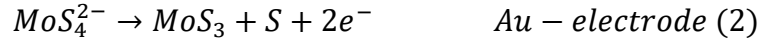
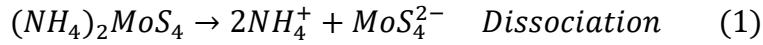
Figure 3-1 a) Electrochemical setup followed by post annealing scheme b) Scheme for the transfer of the electrodeposited film from Au covered growth substrate to a base silicon substrate and corresponding real image.

### 3.3. Results and discussion

#### 3.3.1. Electrodeposition and mechanical transfer of MoS<sub>x</sub> films

Thermal decomposition of ATTM happens between 120 °C and 360 °C and converts to MoS<sub>3</sub>. Above 800 °C in inert environment it turns into MoS<sub>2</sub> [60]. It has been reported that MoS<sub>2</sub> conversion temperature can be reduced from 800 °C to 450 °C by using H<sub>2</sub> in an inert

environment [60]. ATTM can be converted to MoS<sub>3</sub> at room temperature electrochemically according to equation 1 and 2. MoS<sub>3</sub> can be further reduced to MoS<sub>2</sub> by annealing above 450 °C in an inert environment. The thermolysis of electrochemically deposited MoS<sub>3</sub> takes place during post annealing step and results in MoS<sub>2</sub> as one of the final reaction products. The chemical reactions that occur during electrodeposition and post-annealing process are given below [61].



The color contrast of the optical microscope images shows that obtained films are uniform and cover large area (see figure 3.1). ATTM solution with low concentration (1mM) results in uniform and closed thin films. Ultra-thin films having thickness down to 1 nm have been successfully obtained by electrodeposition, which is equivalent to thickness of a bi-layer of MoS<sub>2</sub>. Electrodeposition is one of the best ways to produce large area ultra-thin films of MoS<sub>2</sub> at room temperature and without using vacuum. The polymer coated electrodeposited film with Au layer is mechanically separated from silicon wafer by means of ultra-sonication as shown in figure 3.1b. Due to the operational principle of the ultra-sonication machine standing acoustical waves are produced. Millions of micron sized bubbles are produced at the nodes of those standing waves. Initially, there is a negative pressure creating the bubbles. The size of these bubbles is getting bigger and bigger, until the pressure switches from negative to positive pressure. Due to this positive pressure bubbles are compressed and collapse. This implosion of bubble releases energy and transfer it to the environment. The imploding bubbles can provide enough energy to separate two layers [58]. As a result of ultra-sonication, the PMMA/MoS<sub>x</sub>/Au stack is separated from the

silicon substrate because of low adhesion of Au to silicon. The PMMA layer protects the MoS<sub>x</sub> layer during this procedure from breaking [58].

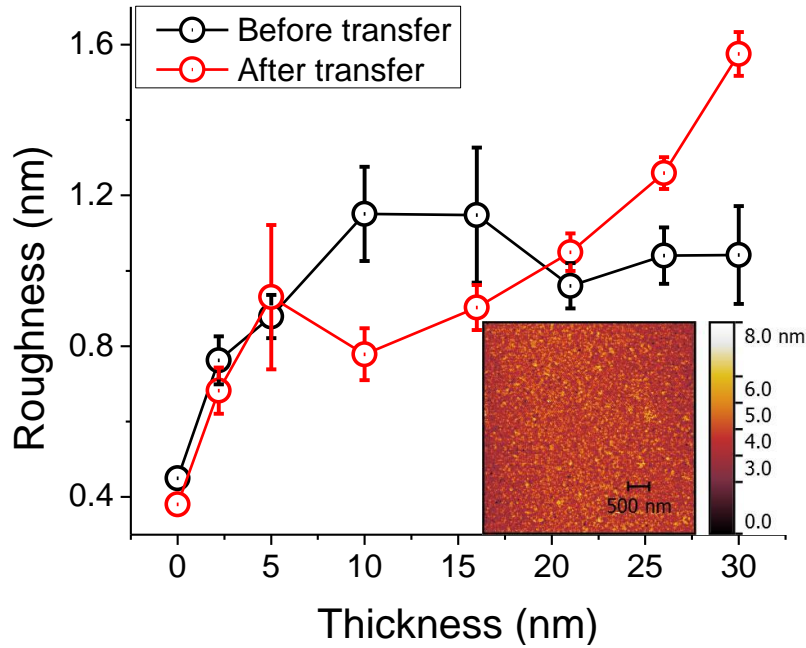


*Figure 3-2 Thickness vs roughness plot of electrodeposited MoS<sub>x</sub> film before and after transfer with inset of atomic force microscopy image electrodeposited layers.*

In figure 3.2 roughness of the electrodeposited film obtained from the AFM images before and after transfer is shown. The surface roughness of the 2.2 nm thick MoS<sub>2</sub> film is ~0.7 nm which is comparable to the thickness of the monolayer of MoS<sub>2</sub>. Furthermore, no big change in the roughness of the films with increasing thickness is observed due to the amorphous nature of the films. The obtained films are uniform and closed as can be seen from the small roughness values of the films in figure 3.2.

### **3.3.2. Characterization of MoS<sub>x</sub> films before and after transferred and annealing**

The MoS<sub>2</sub> formation was investigated by non-destructive spectroscopic methods such as Raman, XPS and UV-Vis spectroscopy.

#### **3.3.2.1. UV-Vis spectroscopy**

In figure 3.3 the UV-Vis spectra of an electrodeposited film before and after post-annealing are shown. In the spectrum of the film before post-annealing a gradual increase in the absorption is observed with decreasing wavelength. It doesn't exhibit any absorption peak which indicates the absence of MoS<sub>2</sub> content in the initial electrochemically deposited film. In contrast, the spectrum of the film after post-annealing exhibit clear characteristic peaks of MoS<sub>2</sub> at 612 nm and 674 nm, which indicates the conversion of electrochemically deposited film to MoS<sub>2</sub>. The peaks at 612 and 674 nm correspond to the A and B excitons of MoS<sub>2</sub> which are attributed to the direct transition at the *K* point of the Brillouin zone

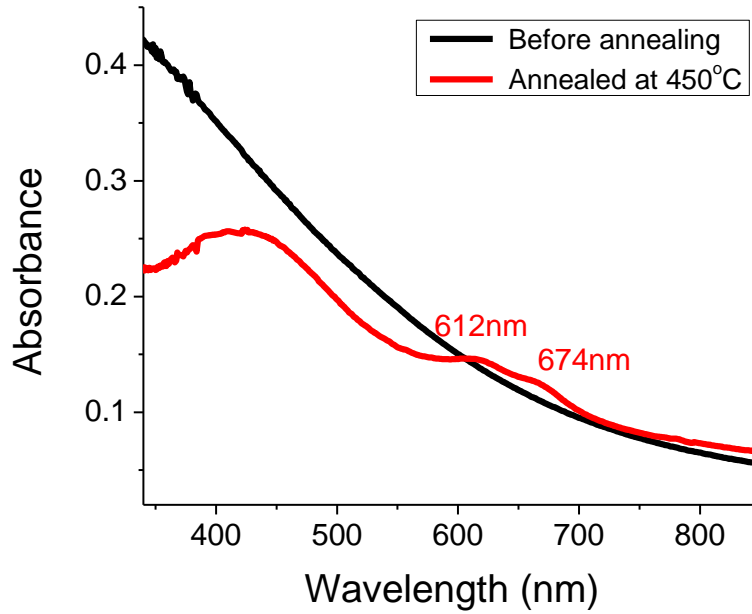


*Figure 3-3 UV-Vis spectra of the electrodeposited films before and after conversion to MoS<sub>2</sub>.*

[62], [13]. In addition a broad peak is visible at around 400-450 nm which is attributed to contain two individual peaks i.e. the C and D excitons which are attributed to inter-band transitions [62].

### 3.3.2.2. Raman spectroscopy

In figure 3.4a Raman spectra of electrodeposited films post-annealed at different temperatures (450-900 °C) are shown. The Raman spectra of the annealed films exhibit two characteristic peaks at 382 cm<sup>-1</sup> and 407 cm<sup>-1</sup>, which correspond to the Raman active modes of MoS<sub>2</sub>, i.e the  $E_{2g}^1$  (in plane vibrational mode) and  $A_{1g}$  (out of plane vibrational mode) [29]. According to group theory, there are four Raman active modes of MoS<sub>2</sub> [63] but only two of them are observed in the measured spectral range. The four Raman active

mode of MoS<sub>2</sub> are A<sub>1g</sub> (out-of-plane vibration (c-axis) of S atoms) at 407 cm<sup>-1</sup>, E<sub>2g</sub><sup>1</sup> (in-plane vibration (basal plane) of Mo and S atoms) at 382 cm<sup>-1</sup>, E<sub>1g</sub> (in-plane vibration (basal plane) of S atoms) at 286 cm<sup>-1</sup>, and E<sub>2g</sub><sup>2</sup> (in-plane vibration (basal plane) of Mo and S atoms) at 32 cm<sup>-1</sup>. E<sub>1g</sub> is invisible under back-scattering Raman geometry and for E<sub>2g</sub><sup>2</sup> the sensitivity factor is relatively small [64]. Among all Raman active modes of MoS<sub>2</sub>, E<sub>2g</sub><sup>1</sup> and A<sub>1g</sub> are widely studied and they also depend on the thickness of the MoS<sub>2</sub> films [29]. The Raman measurements allow to study the crystallinity of the MoS<sub>2</sub> films post-annealed at different temperatures. In figure 3.4b the full width at half maximum (FWHM) of both modes (E<sub>2g</sub><sup>1</sup> and A<sub>1g</sub>) is plotted against the post-annealing temperature. The FWHM for both Raman active modes is large for low temperature and small for high temperature [15]. Decreasing FWHM with increasing temperature indicates that the crystalline quality of the MoS<sub>2</sub> improves for higher post-annealing temperatures. For comparison the Raman spectrum for geologically found bulk MoS<sub>2</sub> is also measured. It is found that the FWHM of the MoS<sub>2</sub> film annealed at 900 °C is essentially equal to the value of the reference MoS<sub>2</sub> crystal (FWHM<sub>A<sub>1g</sub></sub> = 1.94 cm<sup>-1</sup> and FWHM<sub>E<sub>2g</sub><sup>1</sup></sub> = 1.71 cm<sup>-1</sup>). The minor difference in FWHM between electrochemically obtained MoS<sub>2</sub> and the geological MoS<sub>2</sub> crystal is attributed to the polycrystalline nature of the layers, which has more grain boundaries and related imperfections. A reported study shows that crystal grain size of MoS<sub>2</sub> increases with increasing post-annealing temperature [25]. Similarly, HR-TEM also shows high crystal quality for samples annealed at 900 °C [25] which is consistent with our measured Raman results.

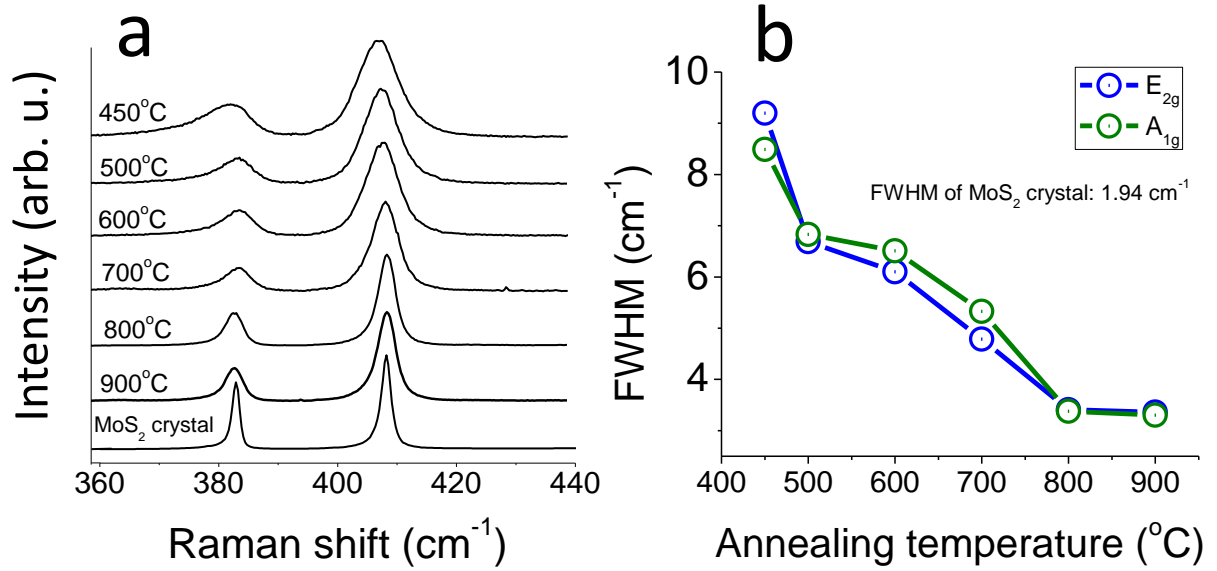


Figure 3-4 a) Raman spectra of the MoS<sub>2</sub> films annealed at different temperature. b) FWHM of E<sub>2g</sub><sup>1</sup> and A<sub>1g</sub> peak vs post annealing temperature.

In figure 3.5 Raman spectra of MoS<sub>2</sub> films with different thicknesses (Bilayer to bulk) are shown. A red-shift is observed for the peak position of the E<sub>2g</sub><sup>1</sup> mode and a blue-shift is observed for the peak position of the A<sub>1g</sub> mode with increasing number of MoS<sub>2</sub> monolayers. Both peaks are moving away from each other with increasing number of MoS<sub>2</sub> monolayer. According to literature the difference between A<sub>1g</sub> and E<sub>2g</sub><sup>1</sup> peak positions is 20 cm<sup>-1</sup> for MoS<sub>2</sub> monolayer and 27 cm<sup>-1</sup> for MoS<sub>2</sub> bulk [29], [65]. So in Figure 5 the Raman spectrum with a difference of 22 cm<sup>-1</sup> between peak positions is attributed to MoS<sub>2</sub> bi-monolayer while the Raman spectrum with 27 cm<sup>-1</sup> difference between peak positions is attributed to bulk-like MoS<sub>2</sub>, i.e > 6 ML. These results agree with the expected layer thickness from profilometer measurements. In figure 3.5, AFM image of transferred MoS<sub>2</sub> layer is shown. The thickness of the film is 1.9 nm which is equivalent to three monolayers of MoS<sub>2</sub> as thickness of the MoS<sub>2</sub> monolayer is 0.65 nm [66].

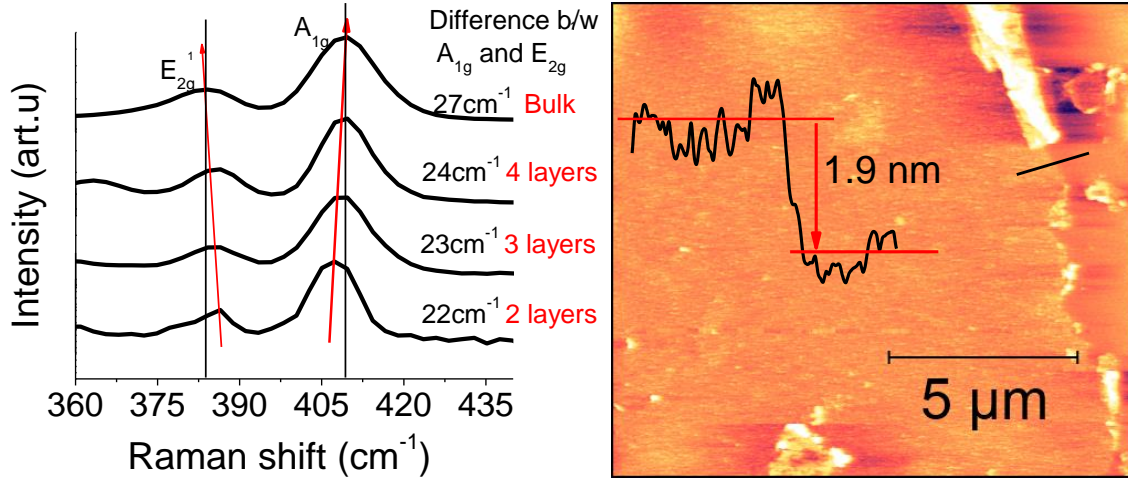


Figure 3-5 Raman spectra of MoS<sub>2</sub> films with different thicknesses (left). Atomic force microscope image of a transferred MoS<sub>2</sub> film on silicon wafer (right).

### 3.3.2.3. X-ray photoelectron spectroscopy

In figure 3.6 x-ray photoelectron spectra of the Mo<sub>3d</sub> doublet and the S<sub>2s</sub> singlet with corresponding peaks are shown. The spectrum in the upper panel is of a film after the electrochemical deposition while the lower panel contains the spectrum of this film transferred to Si substrate and after annealing at 800 °C. The spectrum of the electrochemically deposited film exhibits a Mo<sub>3d</sub> doublet with binding energy of 232.7 eV and 229.5 eV for the Mo3d<sub>3/2</sub> and 3d<sub>5/2</sub>, respectively, which is attributed to MoS<sub>3</sub> [67]. The atomic ratio between Mo<sub>3d</sub> and S<sub>2s</sub> peaks is found to be 1:2.85. It can also be deduced from the atomic ratio that the electrodeposited film contains MoS<sub>3</sub>. In the lower panel, the spectrum of the transferred film annealed at 800 °C consists of a Mo<sub>3d</sub> doublet with a binding energy of 232.2 eV and 229 eV for the Mo3d<sub>3/2</sub> and 3d<sub>5/2</sub>, respectively. The red-shift in the binding energy of the 3d state of Mo with respect to the MoS<sub>3</sub> counterpart is 0.5 eV, which is attributed to the formation of MoS<sub>2</sub> [68]. The peak intensity of the S<sub>2s</sub>



peak reduces when the film is annealed at 800 °C because the MoS<sub>3</sub> reduces to MoS<sub>2</sub>. The Atomic ratio between Mo<sub>3d</sub> and S<sub>2s</sub> peaks is found to be 1:2.08, which is close to the ideal MoS<sub>2</sub> ratio. Hence the formation of MoS<sub>2</sub> is confirmed after annealing which is also verified by Raman and UV-Vis spectroscopy.

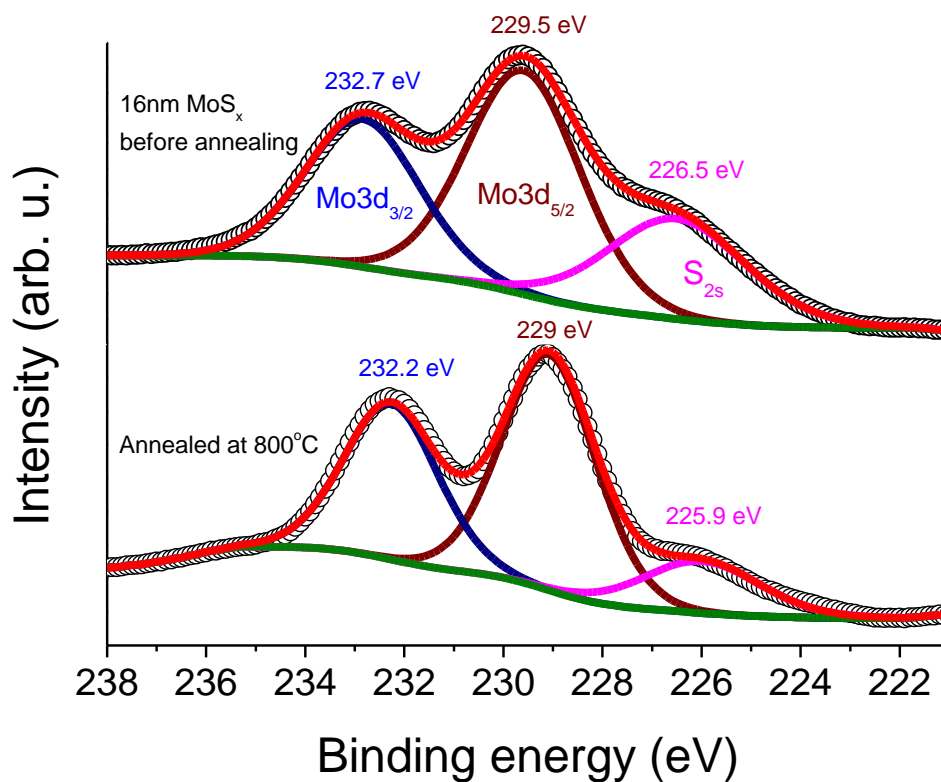


Figure 3-6 XPS spectrum: Mo<sub>3d</sub> and S<sub>2s</sub> peaks of the electrodeposited film before and after conversion to MoS<sub>2</sub>.

### 3.4. Conclusion

Ultra-thin films of MoS<sub>x</sub> were successfully deposited by means of electrochemical deposition at room temperature. The film thickness was controlled by varying the electrodeposition time. A film thickness down to 1 nm was successfully achieved. For film thickness beyond a thickness of 10 nm the roughness stayed around 1 nm which is comparable to the thickness of monolayer of MoS<sub>2</sub>. The roughness of the films was found to be essentially thickness independent as expected from smooth, uniform films covering the surface completely. The electrochemically deposited films were successfully transferred from the initial Au substrate to a bare silicon substrate. The mechanical transfer method followed by environmental-friendly standard Au etching is a novel green method for thin film transfer without using toxic chemicals. It doesn't harm the MoS<sub>x</sub> film during transfer process. Furthermore, the underlying growth substrate can be reused. The MoS<sub>x</sub> films were successfully converted to MoS<sub>2</sub> by post annealing with an additional sulfur source in Ar/H<sub>2</sub> environment. The reduction of the electrodeposited films to MoS<sub>2</sub> was confirmed by Raman, XPS, and UV-Vis spectroscopy. The crystallinity of the MoS<sub>2</sub> films was improved with higher post annealing temperatures as confirmed by Raman measurements. The successful preparation and transfer of bilayer of MoS<sub>2</sub> was as well confirmed by Raman spectroscopy.

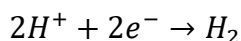
## Chapter 4

### 4. Electrodeposited ultra-thin MoS<sub>2</sub> films for hydrogen evolution reaction

This work is submitted to Journal of Physics D: Applied Physics in November 2020

#### 4.1. Introduction

Among other 2D transition metal dichalcogenide materials, molybdenum disulfide is one of the promising candidates for hydrogen evolution reaction. It has been investigated in many research areas such as transistors [8], water splitting [28], photovoltaic cells [69] and photocatalysis [62] due to its characteristic mechanical, optical and electronic properties [9], [52], [33]. Hydrogen is a promising fuel that can replace fossil fuel in the future, and it has a high energy density. The best source of hydrogen is water due to its abundance and it produces harmless byproduct. Water can be electrochemically split into oxygen and hydrogen in a two half-cell reaction, where the hydrogen evolution reaction is given below:



For hydrogen evolution reaction (HER), a catalyst is required to lower the overpotential. The current state of the art catalyst for HER is platinum [3]. For mass production of hydrogen, platinum has limitations because of its high cost and low abundance. One of the promising replacement materials for HER is MoS<sub>2</sub> because of its suitable band structure for HER. The bandgap of MoS<sub>2</sub> is 1.8 eV unlike conducting 2D graphene. Nanocrystalline MoS<sub>2</sub> particles are more active for HER [4], [70] than the layered MoS<sub>2</sub> [19]. MoS<sub>2</sub> has been deposited by different deposition methods such as chemical vapor deposition (CVD) [9], spray coating [27], dip-coating [25] and electrochemical deposition [28]. Previously, MoS<sub>2</sub> flakes were grown on gold substrate by CVD process and showed good HER activity.

But flakes size was small and only 23% of the surface was covered by flakes [24]. Similarly, MoS<sub>2</sub>/MoS<sub>3</sub> has also been produced by electrochemical process for HER on glassy carbon substrate [28]. Amorphous MoS<sub>3</sub> is formed in anodic regime while amorphous MoS<sub>2</sub> is formed in the cathodic regime [28]. MoS<sub>2</sub> nanoparticles grown on graphene [71] and MoS<sub>2</sub> nanosheets obtained by mechanical activation of MoO<sub>3</sub> and S micro-particles [72] are also demonstrated to be active catalysts for HER. Chemically exfoliated 1T-MoS<sub>2</sub> performed better for HER than 2H-MoS<sub>2</sub> [21]. In this work, MoS<sub>2</sub> ultra-thin films are grown electrochemically (at a constant voltage of 0.38 V with respect to a saturated calomel reference electrode) followed by an additional post annealing at 450 °C in Ar/H<sub>2</sub> environment. This method gives complete surface coverage and controllable thickness of the films. Thickness of the film depends on the concentration of the precursor and the time of deposition, which are well controllable parameters. In the present case, the concentration of the precursor solution was kept constant while electrodeposition time was varied to get a desired film thickness. Any underlying flat conducting substrate can be used for this purpose. These films are characterized by Raman spectroscopy, atomic force microscopy (AFM) and x-ray photoelectron spectroscopy (XPS) before and after annealing. Finally, HER activity is measured on different substrates, i.e., Au coated silicon wafer and ITO/glass. These HER measurements of MoS<sub>2</sub> on different underlying substrates were compared. For analysis the Tafel slope was derived from the polarization curves.

## **4.2.Methodology**

### **4.2.1. Sample preparation and electrodeposition**

Silicon wafers with a 270 nm thick SiO<sub>2</sub> layer were used as substrate in this experiment. The substrates were cleaned with acetone and isopropanol in an ultra-sonic bath and treated with UV-ozone for 10 minutes to remove organic contaminations. After the cleaning process 5 nm titanium layer (as an adhesion layer) and 50 nm gold layer were deposited by

62

an e-beam evaporation process. Similarly, 180 nm ITO/glass substrates were also cleaned with the process mentioned above. Three electrodes are used during electrodeposition, i.e. Au deposited on silicon substrates or 180 nm ITO/glass as the working electrode, a platinum wire as counter electrode and a saturated calomel (Hg/HgCl) as a reference electrode (see figure 4.1a). The calomel electrode was kept in the glass tube and 3 M KCl solution was used as a salt bridge. The reduction potential of this reference electrode is 0.27 V with respect to the standard hydrogen electrode at room temperature. For electrodeposition, ammonium tetrathiomolybdate (ATTM) was used as a single source Mo-precursor material in an aqueous solution with a concentration of 1 mM. The electrochemical deposition is done for different deposition times to get thin films with different thicknesses in the range from 2.3 nm to 30 nm. The growth area is defined to  $1 \times 1 \text{ cm}^2$  by optical photolithography. A magnetic stirrer is used during the deposition process to distribute ions in the solution equally to get uniform films. A pipe of bubbling argon gas was dipped into the electrolyte 15 minutes before and during the electrodeposition in order to replace initially dissolved oxygen in the solution with inert argon.

### 4.2.2. Characterization

The thicknesses of the electrodeposited MoS<sub>x</sub> films were measured with a Dektak profilometer after the stripping of the photoresist layer in acetone. In addition, these thin films were also studied with Raman, AFM, and XPS. For the Raman measurements (Horiba Jobin-Yvon T64000) an argon ion laser with 514 nm wavelength was used. Raman scattered light was collected by 50x objective and dispersed by 1200 lines/mm grating. The signal is detected by a charged-coupled device (CCD) detector which was cooled by liquid nitrogen. AFM measurement (Nanosurf) was done to study the morphology of the grown films. XPS measurements (Analyzer: Specs Phoibos 100) were conducted to study the chemical state and composition of the film, which is analyzed with Mg K<sub>α</sub> radiation ( $h\nu = 1253.6 \text{ eV}$ ). Peaks are fitted with a simplified Voigt function and Shirley background using

CASA XPS. After characterization of the electrochemically deposited film, they were annealed at 450 °C in an inert (95% Ar and 5% H<sub>2</sub>) environment to reduce these films to MoS<sub>2</sub>.

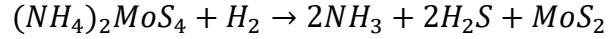
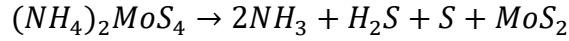
### **4.2.3. Hydrogen evolution reaction**

After annealing these films were again characterized by Raman and XPS measurements. Afterwards they were used for hydrogen evolution reaction (HER) in 1 molar H<sub>2</sub>SO<sub>4</sub> at pH = 0. The H<sub>2</sub>SO<sub>4</sub> solution was saturated with argon in the same way as described above. The setup allowed currents up to 1 mA for the 1 cm<sup>2</sup> sample area. For HER measurements, a three-electrode setup was used: working electrode (MoS<sub>2</sub> thin films on Au or ITO), counter electrode (a platinum wire) and a saturated calomel reference electrode. For the IV (HER) measurements the voltage was scanned from 0.2 to -0.7 V with the rate of 2 mV/s. Tafel slope analysis was done based on the polarization curve. HER measurements were done for all available thicknesses. Furthermore, HER measurements were done on bare Pt, bare Au and bare ITO as reference for comparison.

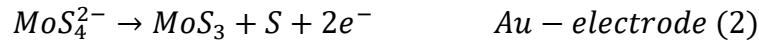
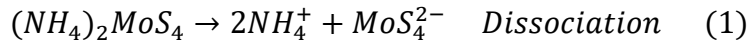
## **4.3. Results and discussion**

### **4.3.1. Film deposition and characterization**

With our approach MoS<sub>2</sub> thin films were electro-synthesized from its [MoS<sub>4</sub>]<sup>2-</sup> precursor followed by a post-annealing step. A single Mo-precursor ((NH<sub>4</sub>)<sub>2</sub>MoS<sub>4</sub>, ATTM) is used for this purpose which decomposes to MoS<sub>3</sub> and H<sub>2</sub>S between 120 °C and 360 °C. It further reduces to MoS<sub>2</sub> at 800 °C in an inert environment [60]. This conversion occurs at a lower temperature of 450 °C if H<sub>2</sub> gas is added to the inert environment. The pure thermal decomposition reaction with and without H<sub>2</sub> gas is given as follows [60]



For electrodeposition MoS<sub>3</sub> thin films can be obtained already at room temperature by electrochemical synthesis. The electrochemical synthesis of MoS<sub>x</sub> is done in an argon saturated electrolyte to avoid the presence of dissolved oxygen. The post-annealing results in MoS<sub>2</sub> as one of the final products. The chemical reactions that occur during the electrochemical and post annealing process are given by [61]



Upon optimizing various parameters such as overvoltage, deposition time and concentration of ATTm, MoS<sub>x</sub> was electro-synthesized with different deposition times to get films with different thicknesses. The optical microscopy image of the electrodeposited film is shown in Figure 4.1. From the color contrast, the deposited film can be easily distinguished from the gold substrate on the left side of the image. A linear behavior between the thickness of the layers and time of deposition was found as expected, because more and more material is deposited with passage of time at constant applied voltage with respect to the reference electrode (see Figure 4.1). The linear behavior of thickness shows that this process is very controllable. A 2.3 nm MoS<sub>2</sub> film has been successfully deposited which corresponds to the thickness of four monolayers of MoS<sub>2</sub> [73]. The thickness of the produced films range from 2.3 nm to 30 nm. The growth rate of the film was found to be 1.7 nm/min.

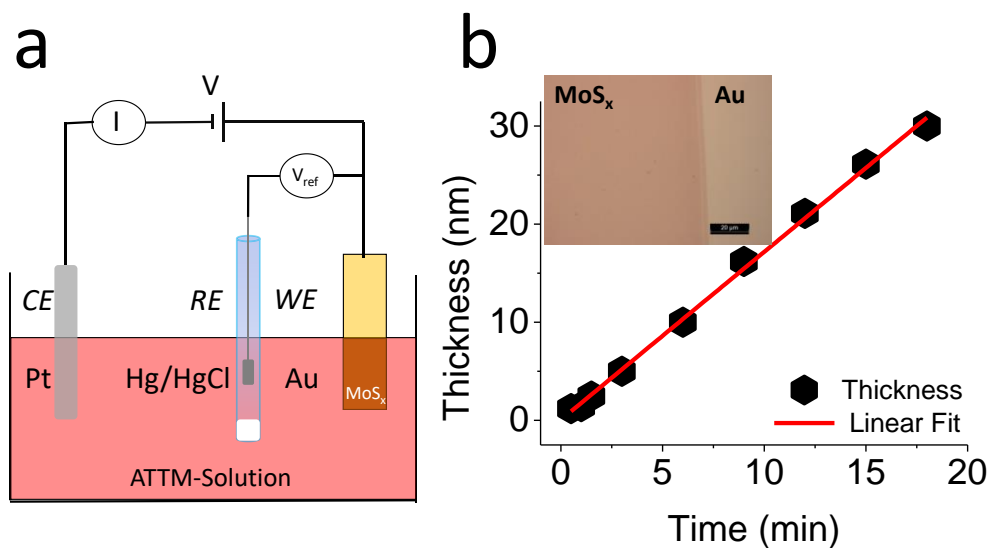


Figure 4-1 a) Electrochemical deposition setup. b) Deposition time vs thickness of the films plot with inset of an optical microscope image (scale bar: 20 μm) of 20 nm electrochemically deposited MoS<sub>x</sub> layer of Au substrate

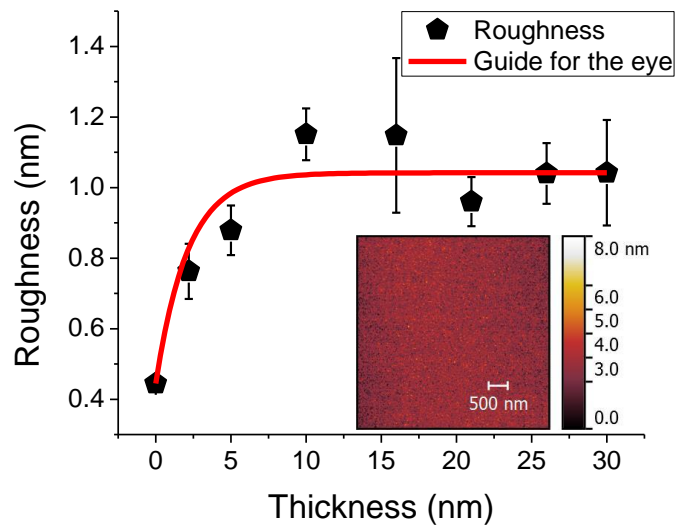


Figure 4-2 Thickness vs roughness plot and inset of atomic force microscope image of the electrochemically deposited film.



The morphology of the films was investigated by atomic force microscope (AFM). Initial roughness of the bare gold surface was found to be 0.42 nm. After depositing MoS<sub>x</sub> film electrochemically the roughness increases as can be seen in the figure 4.2. After a film thickness of 10 nm, the roughness saturates and stays around 1 nm. The roughness of the films is comparable to one monolayer of MoS<sub>2</sub>, which is 0.65 nm [73]. No significant change in the roughness of the film with an increase in thickness implies that the film is closed and uniform.

After the successful deposition of MoS<sub>x</sub> films by electrodeposition, the films were characterized by Raman spectroscopy. The Raman spectrum (Figure 4.3) shows peaks at 320 cm<sup>-1</sup>, 438 cm<sup>-1</sup> and 489 cm<sup>-1</sup> on a broad background. The broad background and broad peaks indicate amorphous material or very low crystalline quality. The broad peak shape and some peaks positions (320 and 428 cm<sup>-1</sup>) match with reported Raman spectra of amorphous MoS<sub>3</sub> prepared by thermal decomposition [74]. As expected from the chemical equation for electrodeposition (Equation 2) it is consistent that deposited film is composed of MoS<sub>3</sub>.

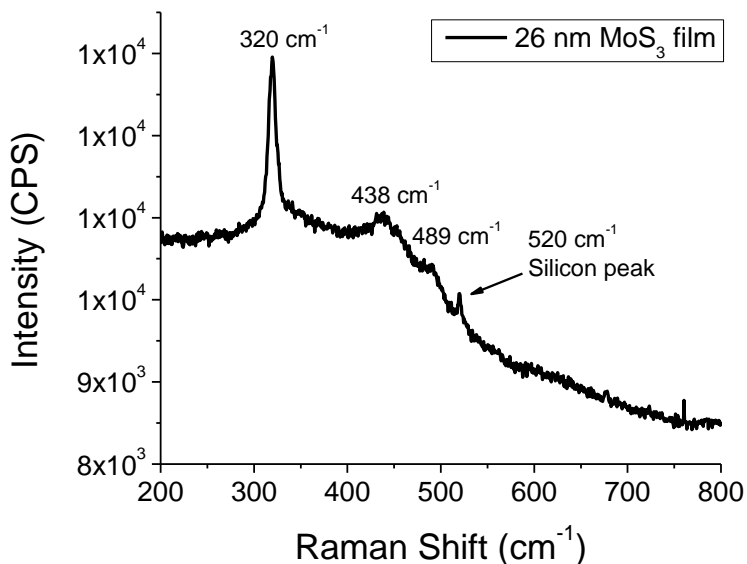


Figure 4-3 Raman spectrum of electrodeposited MoS<sub>3</sub> before annealing.

Raman measurements were also done after annealing the sample at 450 °C in the Ar/H<sub>2</sub> environment. New peaks at 382 and 407 cm<sup>-1</sup> (Figure 4.4) are observed which are Raman active modes (E<sub>2g</sub><sup>1</sup> an in-plane vibration and A<sub>1g</sub> an out-of-plane vibration) of MoS<sub>2</sub>. [63]. MoS<sub>2</sub> has four Raman active modes [63] of which two are observed in Figure 4.4 in the measured spectral range. Thus the MoS<sub>3</sub> was successfully converted to MoS<sub>2</sub> by post annealing as confirmed by Raman measurement. This is in agreement with chemical equation (Equation 3). Information about the crystallinity of the films can be obtained from the full width at half maximum (FWHM) of the Raman peaks. The FWHM of the of the A<sub>1g</sub> Raman mode for a mechanically exfoliated flakes is 1.97 cm<sup>-1</sup> [25]. MoS<sub>2</sub> with high crystal quality has small FWHM and vice-versa. The measured FWHM of MoS<sub>2</sub> Raman active mode (A<sub>1g</sub>) has a large value of 8.3 cm<sup>-1</sup>, which implies that the obtained films have low crystallinity or the MoS<sub>2</sub> films are amorphous. This is beneficial for the HER activity as a reported study shows that amorphous MoS<sub>2</sub> or films with defects exhibit good HER activity [24]. The measured FWHM is found to be independent of the thickness of the films which implies that crystal quality does not change with thickness.

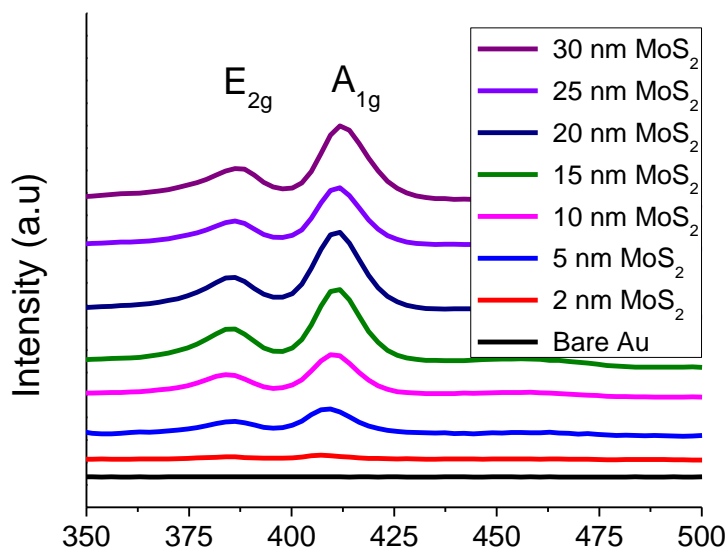


Figure 4-4 Raman spectrum of electrodeposited films with different thickness after annealing at 450 °C.

XPS measurements were done to explore the growth of electrochemical deposited film and conversion to MoS<sub>2</sub> after annealing. Figure 4.5 exhibits Mo3d<sub>3/2</sub>, Mo3d<sub>5/2</sub> and S2s core level photoelectron transitions. For data evaluation Mo<sub>3d</sub> with two doublets (Mo3d<sub>3/2</sub> and Mo3d<sub>5/2</sub>) with a spin-orbit splitting of 3.16 eV and a single S<sub>2s</sub> peak were used. Before annealing Mo<sub>3d</sub> had two components, one is from sulfide and the second one belongs to oxygen and carbon contaminations which disappear after annealing. The oxide or carbide contaminations come from the atmosphere since the film was exposed to the atmosphere during transport from the electrochemical setup to the XPS chamber. The S<sub>2s</sub> peak is fitted at 226.7 eV before annealing as can be seen in figure 4.5. This peak position corresponds to MoS<sub>3</sub> [67]. Due to the reduction of MoS<sub>3</sub> to MoS<sub>2</sub> a drop of the S<sub>2s</sub> peak intensity is observed. From data evolution of Mo<sub>3d</sub> and S<sub>2s</sub> peaks before and after annealing, it is deduced that before annealing there is electrochemically deposited MoS<sub>3</sub> layer on a gold substrate with some oxygen and carbon contaminations which are removed by post annealing step and MoS<sub>3</sub> is successful converted to MoS<sub>2</sub>. The atomic ratios between Mo and Sulfur are given in table 1 which are obtained using a single layer model and Scofield cross-sections [75].

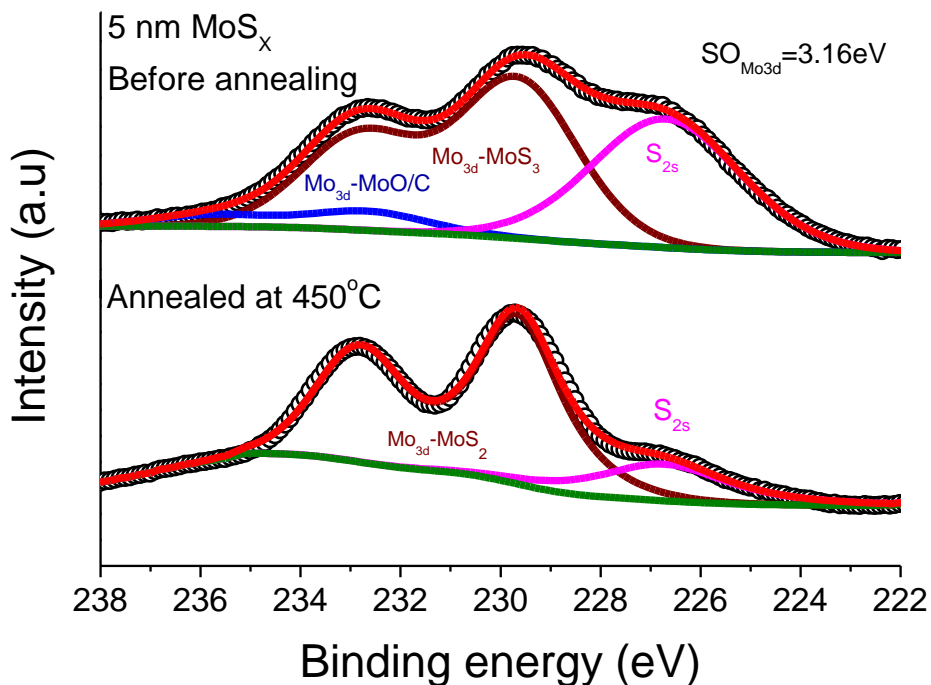


Figure 4-5 XPS spectrum: Mo<sub>3d</sub> and S<sub>2s</sub> before and after annealing at 450 °C.

Table 4-1 The atomic ratio between Mo and S calculated before and after annealing.

	Mo	S
Before annealing	1	3.1
After annealing	1	1.8

The conversion from MoS<sub>3</sub> to MoS<sub>2</sub> during the annealing step is also confirmed by Raman spectroscopy results discussed before. The atomic ratio obtained from XPS measurements indicates that there is sulfur deficiency or S-vacancies in the obtained MoS<sub>2</sub>. A reported study shows that S-vacancies act as active sites for HER [24], [76]. Defects are also engineered by plasma and hydrogen treatment in MoS<sub>2</sub> monolayer to further increase the

efficiency of HER [77]. After the spectroscopic study of the films HER measurements were done next.

#### **4.4. Hydrogen evolution reaction**

To characterize the hydrogen evolution reaction (HER) of the ultrathin MoS<sub>2</sub> films, polarization curves of the electrodeposited and subsequently annealed films were recorded for the MoS<sub>2</sub> films on Au and ITO substrates. Furthermore, Pt, Au and ITO electrodes were measured as a reference with respect to the standard hydrogen electrode to determine the activity of the bare substrates. For the pure ITO surface from the slight increase of the current density the overpotential could not be determined within the measurement range due to unsufficient change in current density (see figure 4.6). For Pt and Au overpotentials of -0.02 V and -0.12 V, respectively, were determined for a current density of 1 mA/cm<sup>2</sup>. All MoS<sub>2</sub> films either on the Au or on the ITO substrate showed HER activity. It is further notable that the overpotential is gradually decreasing with the thickness of the MoS<sub>2</sub> films on the Au substrate. Whereas the overpotential for a 30 nm thick MoS<sub>2</sub> film is -0.33 V, it converges with thicknesses below 10 nm to -0.22 V (Figure 4.6). The complete set of measurements between 30 nm and 2.2 nm can be found in Figure 4.7. The decreasing overpotential with increasing thickness is attributed to a series resistance effect in the films. Since crystal quality remains the same according to the FWHM of the Raman peaks (see figure 4.4).

In order to confirm that the HER activity is produced by the MoS<sub>2</sub> film itself and not by the underlying Au substrate via defects in the film, MoS<sub>2</sub> films have been prepared under the same conditions on an ITO/glass substrate. In comparison to the bare ITO surface, which exhibits only minor HER activity, the deposited MoS<sub>2</sub> films have overpotentials ranging from -0.37 V to -0.24 V (see Figure 4.6). In contrast to Au, the ITO substrate has a roughness of 2.2 nm (see Figure 4.8), which leads to a less systematic behaviour of the overpotential in dependence of thickness. Thin layers with thickness comparable to the

substrate (ITO) roughness show now not the best but a larger overpotential. The minimum value of -0.24 V is now obtained for a medium film thickness of 9.5 nm. However, the range of overpotential values indicate that the HER activity has its origin in the MoS<sub>2</sub> layer only (Figure 4.6). The results on ITO justifying the assumption of a closed layer with no passways to the substrate. The hysteresis in the curves is due to the H<sub>2</sub> bubble formation on the surface of MoS<sub>2</sub>. Therefore, HER activity determination is done in the forward direction only, where fewer bubbles are present on the ITO/glass surface.

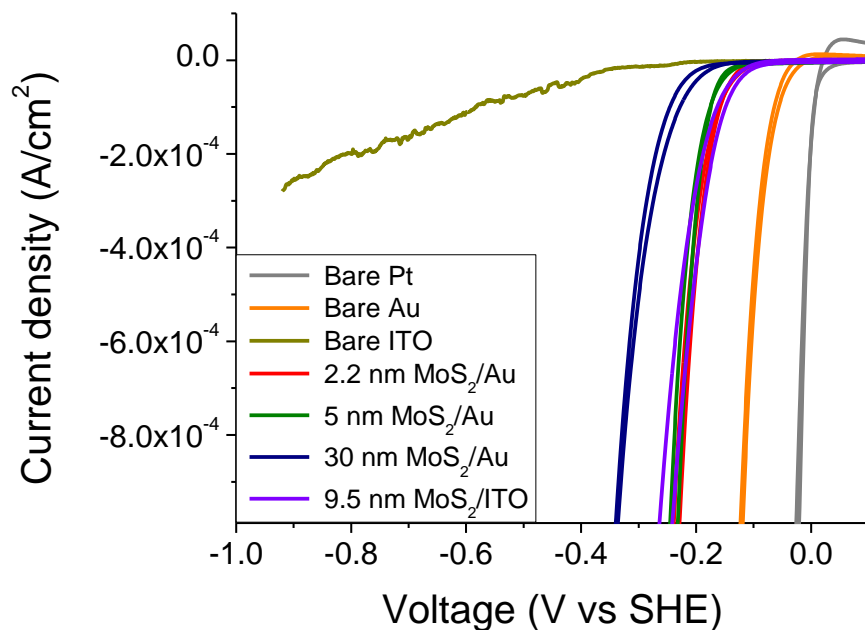


Figure 4-6 Polarization curve of MoS<sub>2</sub> films on ITO and Au substrate and Pt as a reference.

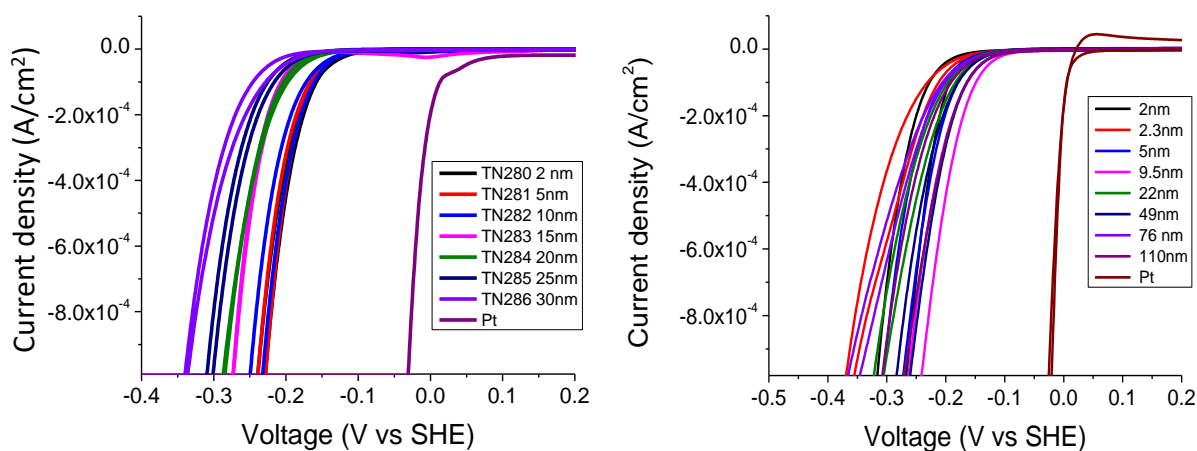
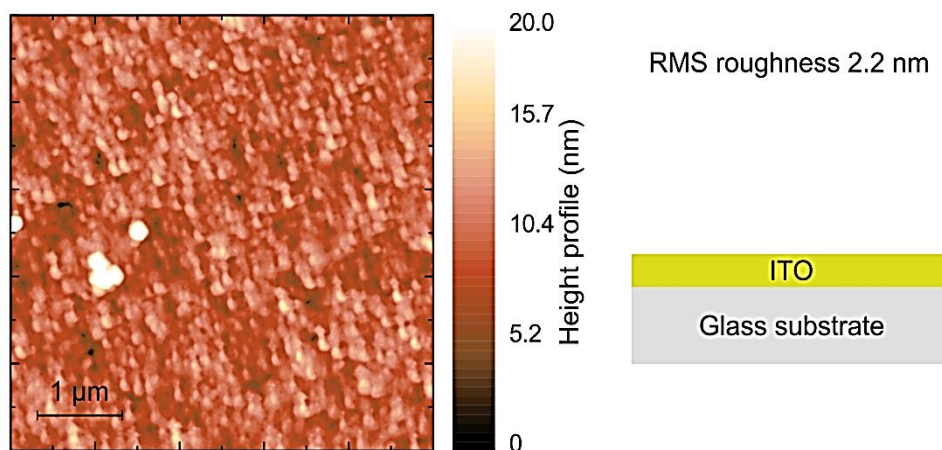


Figure 4-7 Polarization curve of MoS<sub>2</sub> films with different thicknesses on Au substrate (left).  
b) Polarization curve of MoS<sub>2</sub> films with different thicknesses on Au substrate.



*Figure 4-8 AFM picture of ITO on glass surface.*

The reaction rate of the hydrogen evolution reaction is evaluated in Figure 4.9 which exhibits the Tafel plot of a polarization curve for a 5 nm and a 30 nm thick MoS<sub>2</sub> film on Au substrate and a 9.5 nm MoS<sub>2</sub> film on ITO substrate. The analysis of the data at overpotentials in the range between -0.05 V and -0.3 V and their corresponding current densities give a slope within the Tafel plots of 45, 44, 68 and 61 mV per decade for thicknesses of 2.2 nm, 5 nm, 30 nm MoS<sub>2</sub> on Au and 9.5 nm MoS<sub>2</sub> on ITO, respectively. Thin films perform better than thicker films. Only amorphous MoS<sub>2</sub> samples on a glassy carbon substrate are reported to have similar value of 40 mV per decade [28], whereas single crystal MoS<sub>2</sub> shows 55 to 60 mV per decade [4], nanoparticulate MoS<sub>2</sub> films 120 mV per decade [70], and WS<sub>2</sub> 138 mV per decade [5], with a smaller Tafel slope is favorable for HER.



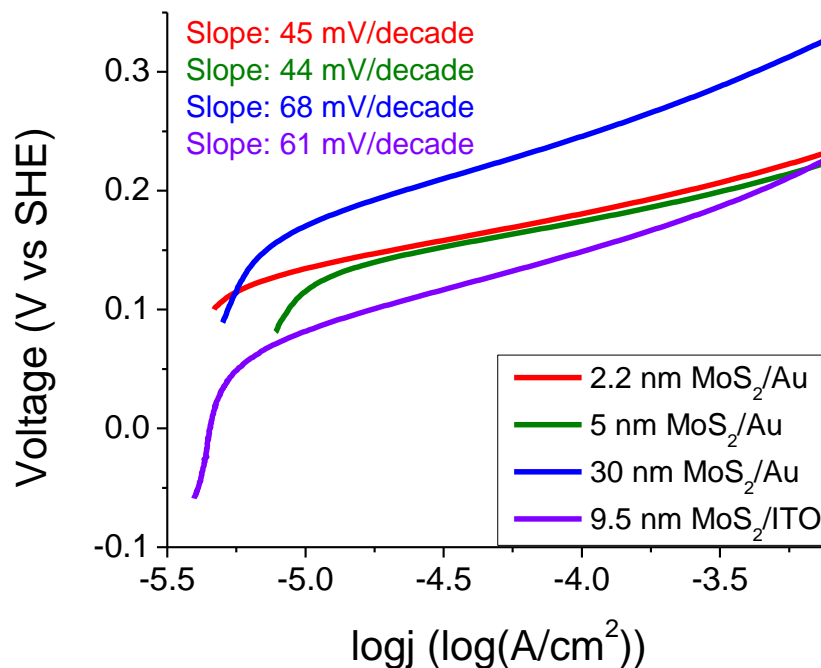


Figure 4-9 Tafel plots obtained from polarization curves.

## 4.5. Conclusion

In conclusion, I have successfully deposited thin layers of MoS<sub>3</sub> with different thicknesses by an electrochemical deposition method. The MoS<sub>3</sub> layers are converted to MoS<sub>2</sub> by post annealing at 450 °C in Ar/H<sub>2</sub> environment. As based on the roughness measurements, I found that the films are uniform and the surface is completely covered. Raman and XPS results show that the electrodeposited films before annealing are composed of MoS<sub>3</sub>, whereas the subsequent annealing at 450 °C leads to a conversion to MoS<sub>2</sub>. These films show good HER activities, as deduced from the small Tafel slope of 44 mV per decade. Measurements on different substrates verify that the HER occurs at the MoS<sub>2</sub> layer. MoS<sub>2</sub>

is cheaper and more abundant compared to noble metal catalysts. The MoS<sub>2</sub> catalyst can be prepared on a large scale by electrochemical deposition and can be used for hydrogen production from water as fuel.

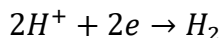
## Chapter 5

### 5. Growth of MoS<sub>2</sub> films by spin coating for hydrogen evolution reaction

This work is submitted to Journal of Applied Electrochemistry on Dec 22<sup>nd</sup>, 2020.

#### 5.1.Introduction

Transition metal dichalcogenides (TMDs) two-dimensional have attracted intensified research in recent years due to their potential for a wide range of applications [78], [53], [62]. A suitable catalyst is required for the hydrogen evolution reaction to lower the overpotential and minimize energy consumption. Among other 2D-TMDs, MoS<sub>2</sub> is one of the best catalysts for the hydrogen evolution reaction (HER) because of its suitable band structure. It has a bandgap of 1.8 eV [79], unlike the conducting analogue material graphene. Hydrogen can replace currently used fossil fuel in the future due to its high energy density, and it can be obtained from water due to its abundance and harmless byproducts by means of HER [4] and oxygen evolution reaction (OER) [80]. The current state of the art catalyst for HER is Pt [3], but due to its low abundance and high cost, it needs to be replaced by some high earth abundance and low cost material such as MoS<sub>2</sub>. MoS<sub>2</sub> assists splitting water into O<sub>2</sub> and H<sub>2</sub> electrochemically [4] in one of the two half-cell reaction, where the cathodic part of the reaction is given below



For mass production, MoS<sub>2</sub> thin films need to be produced on a large scale. 2D TMDs films/flakes have been grown by various deposition methods [81], [39], [40], [82], [83]. MoS<sub>2</sub> thin films have been deposited by various deposition methods for HER, such as chemical vapor deposition (CVD) [24], electrochemical deposition [28], thermal

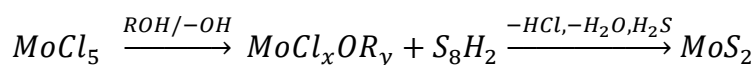
decomposition [84] and spray coating [85]. Other reported deposition methods such as CVD give high-quality MoS<sub>2</sub> crystals but require vacuum processing. In this work MoS<sub>2</sub> thin films have been produced by mean of spin coating using a novel single source Mo-precursor (MoCl<sub>5</sub>) which was previously used only for field effect transistor [57]. The spin coated Mo-precursor is converted to MoS<sub>2</sub> by post-annealing at 450 °C with an additional sulfur source in an inert environment. Spin coating is a large area deposition method. The thickness of the film depends on the concentration of the precursor solution and spin speed. In the present case, spin speed was kept constant while concentration was varied to get a desired thickness of the film. The synthesized MoS<sub>2</sub> films were used for the HER and HER activity was observed. MoS<sub>2</sub> film thickness dependence HER measurements are done. The results of HER were comparable to the amorphous MoS<sub>2</sub> grown by electrodeposition [28]. The Tafel slope extracted from the polarization curves and compared with MoS<sub>2</sub> obtained by other deposition methods and other TMDs.

## 5.2. Methodology

### 5.2.1. Spin coating of precursor and conversion to MoS<sub>2</sub>

Molybdenum (V) chloride (MoCl<sub>5</sub>) precursor (as single source Mo-precursor) was dissolved in 1-methoxy-2-propanol with different concentrations (4-50 mg/ml) to get different film thicknesses after spin coating. The prepared solutions were stirred overnight in order to obtain uniform closed films. MoCl<sub>5</sub> is very reactive with organic solvent, e.g. 1-methoxy-2-propanol results in HCl formation [86]. The resulting solution is quite stable in air. After preparation of the solution, 180 nm ITO/glass was cleaned with acetone and isopropanol and dried with a nitrogen gun. The substrate was heated at 120 °C for 15 min to evaporate the solvents and is afterwards treated with UV-ozone to remove organic contamination. The as-prepared solution was spin-coated on 1 × 1 cm<sup>2</sup> ITO/glass substrate with 3000 rpm for 1 min. The obtained films were pre-annealed at 150 °C for 20 min to

evaporate the remaining solvents. The thickness of the fabricated films is directly proportional to the concentration of the precursor solution. The samples were then post annealed at 450 °C in a 95% Ar and 5% H<sub>2</sub> environment with an additional sulfur source present. The hydrogen gas helps to remove organic impurities originating from the solvent used in the preparation of the precursor solution (before spin coating). For this purpose, samples were placed in a quartz tube and the tube was inserted in an oven. Pure sulfur was kept in a separate container in the upstream near the edge of the oven. The boiling point of sulfur is 444.6 °C and the high vapor pressure helps in the diffusion of the sulfur atoms into the film and reduction of the precursor to MoS<sub>2</sub>. The air in the quartz tube was replaced by the Ar/H<sub>2</sub> gas with a high flow rate for 3 min. The temperature of the oven was raised from room temperature to 450 °C at a rate of 20 °C/min. The target temperature was maintained for 120 min. The chemical reaction that occurs during the process is given below [25]. The complete experiment is illustrated in figure 5.1.



### 5.2.2. Characterization of films before and after conversion

The obtained films were characterized by different spectroscopic techniques, i.e. Raman, UV-Vis and XPS, to investigate the composition of the films and their crystal quality. For the Raman measurement, a 514 nm laser was used at 1 mW power. 50x objective was used to collect the Raman scattered photons. The collected signal was then dispersed with a 2400 g/mm grating and the signal was detected by charge-coupled device (CCD) detector cooled by liquid nitrogen (Horiba Jobin-Yvon T64000). The UV-Vis measurements of the films were performed using a Cary 5000 UV-Vis-NIR spectrophotometer in the spectral range from 200 nm to 1100 nm. For the UV-Vis measurements, the films were deposited on quartz substrates. For X-ray photoelectron spectroscopy (XPS) the layers were deposited on a gold coated silicon wafer substrate to avoid charging during the XPS

measurements. Photoelectrons were excited by  $MgK\alpha$  radiation ( $E=1253.6$  eV) from an Mg/Al X-ray gun (Specs XP-50). The analyzer was operated in fixed analyzer transmission mode with a pass energy of 50 eV. The energetic shift in the binding energy position due to minor charging of the sample was corrected with respect to the C<sub>1s</sub> peak. The data evaluation was done by CASAXPS<sup>TM</sup> software. Shirley's method was used to subtract the background. To investigate the surface morphology, atomic force microscopy (AFM, Nanosurf) in tapping mode was performed.

### 5.2.3. Hydrogen evolution reaction

After spectroscopic and morphology measurements, the samples were used for the hydrogen evolution reaction (HER). For this purpose, 1 molar sulfuric acid (H<sub>2</sub>SO<sub>4</sub>) was used at pH=0. A potentiostat with three electrodes was used: working electrode (MoS<sub>2</sub> thin films spin coated on ITO/glass substrate), counter electrode (a platinum wire) and a calomel reference electrode (Hg/HgCl). The HER study was done on samples with different thicknesses. The setup allowed currents up to 1 mA for the 1 cm<sup>2</sup> sample area. To observe HER activity of the MoS<sub>2</sub> layers the over voltage was scanned from 0.2 to -0.7 V with respect to a standard hydrogen electrode (SHE) with a scan rate of 2 mV/s. To obtain the reaction rate of the HER, Tafel slope analysis was done based on the polarization curve.

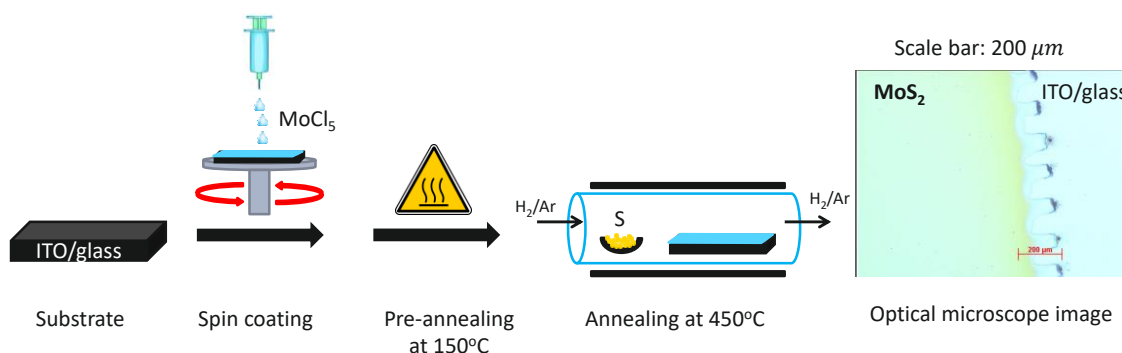


*Figure 5-1 Schematic illustration of the sample preparation: From liquid phase precursor till conversion to MoS<sub>2</sub> films.*

### 5.3. Results and discussion

#### 5.3.1. Spin coating of MoS<sub>2</sub> films and characterization

##### 5.3.1.1. Film thickness and morphology

In figure 5.2, thickness and the roughness of the spin coated films against the concentration of the precursor is shown. The film thickness was measured with the atomic force microscope (AFM). The thickness of the films shows a linear correlation with the concentration of the precursor solution. Films from 25 nm down to 2.2 nm were successfully deposited with surface roughness less than 1 nm. Thinnest film (2.2 nm) is similar to the thickness of 3 monolayers as reported in our previous work [25]. The surface roughness of the grown films is found to be independent of the thickness of the films. The average roughness is lower than 1 nm, which is comparable to the thickness of a monolayer of MoS<sub>2</sub>. The low roughness of the films also indicates a complete coverage of the surface. It was shown in our earlier study [25], that the films annealed at 450 °C have amorphous nature and crystallinity of the film increases with annealing temperature [25]. In the present case, 450 °C is the upper limit for annealing because the underlying conducting ITO layer is not stable at higher temperatures.

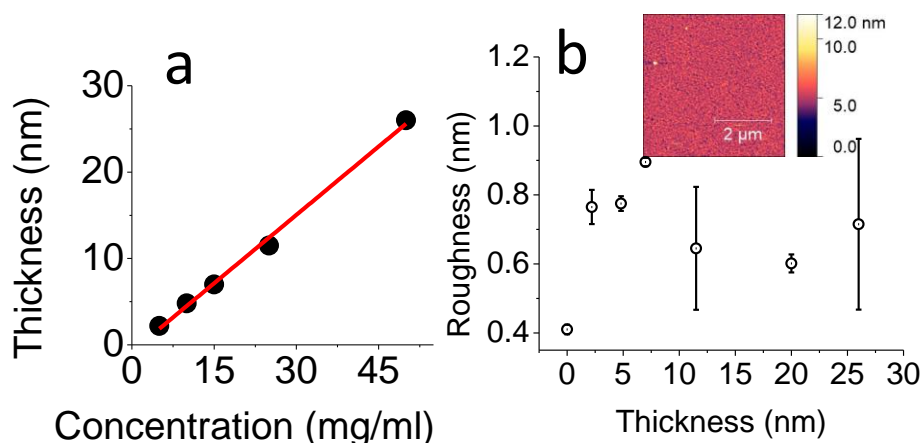


Figure 5-2 a) Thickness of the films vs concentration of the precursor solution. b) Roughness vs thickness of the film with inset of atomic force microscope image of MoS<sub>2</sub> film.

The spin coated single source Mo-precursor was successfully converted to MoS<sub>2</sub> by post annealing at 450 °C in 95% Ar/ 5% H<sub>2</sub> environment with an additional sulfur source. The reduction of the Mo-precursor to MoS<sub>2</sub> during post annealing is studied by Raman, UV-Vis and XPS spectroscopy

### 5.3.1.2. Raman spectroscopy

Raman spectroscopy is a non-destructive way to study the TMDs via their phonon vibrations. In figure 5.3, peaks at 383 cm<sup>-1</sup> and 408 cm<sup>-1</sup> are visible that corresponds to the Raman active modes of MoS<sub>2</sub> [29]. The peak at 408 cm<sup>-1</sup> is related to A<sub>1g</sub> vibrational mode, which is an out-of-plane vibration, while the peak at 383 cm<sup>-1</sup> corresponds to the E<sub>2g</sub><sup>1</sup> vibrational mode, which is an in-plane vibration [29]. According to theoretical prediction, there are four Raman active modes of MoS<sub>2</sub>, of which I observe only two in the measured spectral range [63]. From literature, it is known that the difference between A<sub>1g</sub> and E<sub>2g</sub><sup>1</sup> modes for the monolayer of MoS<sub>2</sub> is 18 cm<sup>-1</sup> and for the bulk-MoS<sub>2</sub> it is 25 cm<sup>-1</sup> [29]. In the measured Raman spectrum (see figure 5.3), a difference of 25 cm<sup>-1</sup> is observed between A<sub>1g</sub> and E<sub>2g</sub><sup>1</sup> modes. This implies that the obtained films are bulk-like MoS<sub>2</sub>. The full width at half maximum (FWHM) of the Raman peak gives us information about the crystal quality. Reported work [25] show that the FWHM of the A<sub>1g</sub> Raman mode for a perfect crystal (mechanically exfoliated flakes) is 1.97 cm<sup>-1</sup> in agreement with own measurement. FWHM increases as quality of the crystal decreases. The FWHM of A<sub>1g</sub> mode in figure 5.3 is 8.1 cm<sup>-1</sup> which means that quality of the crystal is very low or the material is amorphous. Furthermore, the crystallinity of the obtained films is independent of the thickness of the MoS<sub>2</sub> films as FWHM of Raman peaks remains unchanged.



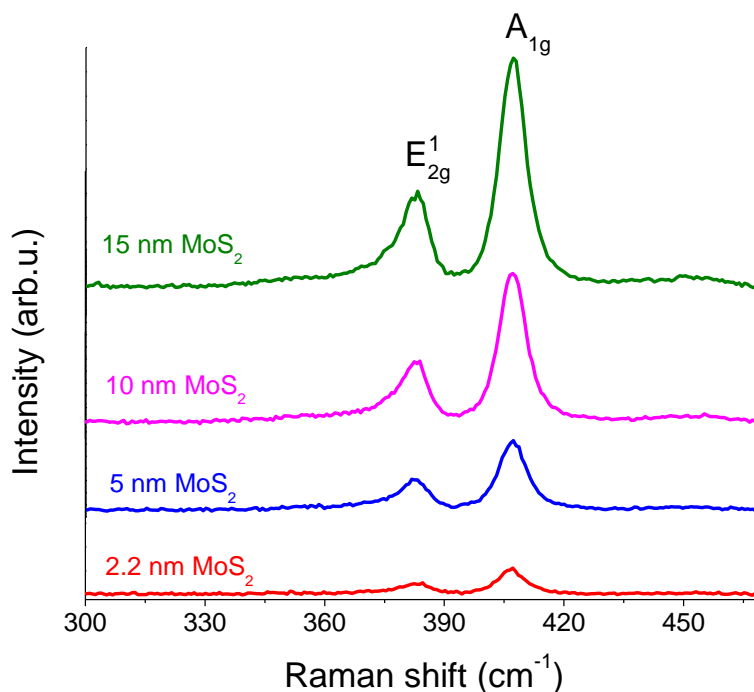


Figure 5-3 Raman spectra of the annealing at 450 °C triggering conversion to MoS<sub>2</sub>.

### 5.3.1.3. UV-Vis spectroscopy

In figure 5.4, the UV-Vis spectra of the spin coated film before and after annealing are shown. UV-Vis absorption measurements were performed for the spin coated and annealed sample to further verify the conversion of the spin coated Mo-precursor to MoS<sub>2</sub>. The spin coated film before annealing exhibited no clear absorption peak, but absorption is slightly increased beyond 400 nm. The lack of characteristic peaks of MoS<sub>2</sub> on the spin coated layer from MoCl<sub>5</sub> before annealing indicates the absence of any MoS<sub>2</sub> content in the as-deposited film. The spectrum of the annealed sample exhibits clear characteristic broad peaks of MoS<sub>2</sub> at 612 nm and 674 nm, which indicates the conversion of as-deposited Mo-precursor to MoS<sub>2</sub> after post annealing. The peaks at 612 nm and 674 nm corresponds to the A and B excitons of MoS<sub>2</sub>, respectively, which originate from a direct transition at the K point of

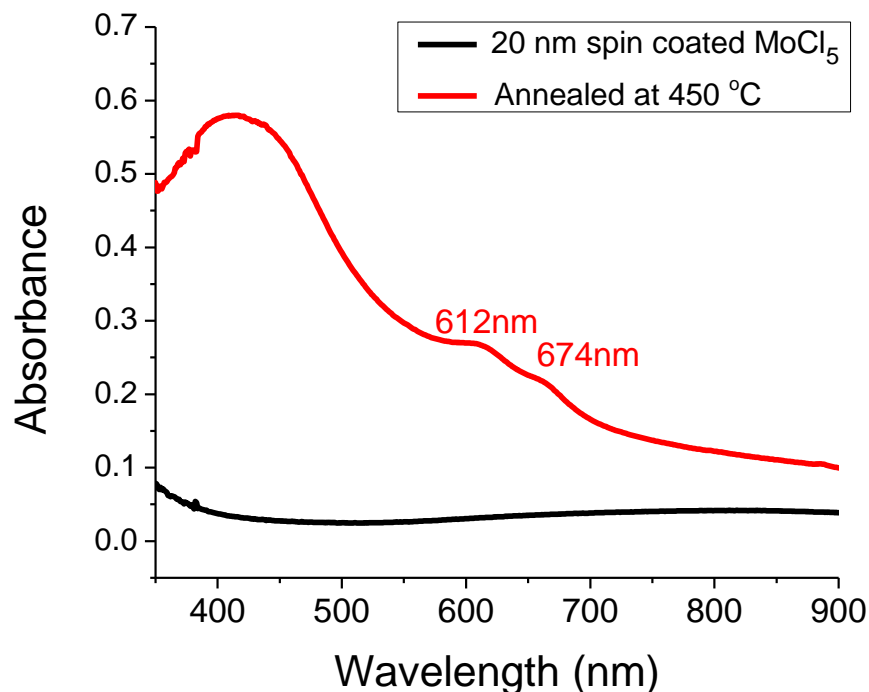


Figure 5-4 UV-Vis absorption spectra of the films before and after annealing at 450 °C triggering conversion to MoS<sub>2</sub>.

the Brillouin zone [73]. In addition, one broad peak are observed around 400-450 nm, which corresponds to the C and D excitons which correspond to further interband transitions [13]. The broadness of the peaks indicates that MoS<sub>2</sub> in the film has low crystal quality or is in the amorphous form [25].

#### 5.3.1.4. X-ray photoelectron spectroscopy

The films were further characterized by XPS to study the chemical state and composition of the spin coated films before and after their conversion to MoS<sub>2</sub>. Figure 5.5 shows the X-ray photoelectron spectra, and corresponding fits for the Mo 3d<sub>3/2</sub> and 3d<sub>5/2</sub> doublet of the sample after spin coating the Mo-precursor and after sample annealing. An additional S<sub>2s</sub>

peak appears in the spectrum after annealing. The spectrum of the just spin-coated Mo-precursor mainly consists of a doublet with a binding energy of 235.5 eV and 232.3 eV corresponding to the Mo 3d<sub>3/2</sub> and 3d<sub>5/2</sub>, respectively, which is attributed to MoO<sub>3</sub> [87]. In the lower panel of figure 5.5, the spectrum of annealed film at 450 °C with an additional sulfur source in an inert environment is shown. The major peaks are now located at 232.4 eV and 229.2 eV [88] corresponding to Mo 3d<sub>3/2</sub> and 3d<sub>5/2</sub>, respectively. The shift of both 3d states of Mo with respect to the MoO<sub>3</sub> counterparts is 3.1 eV. The new peak position fell in the range typical for MoS<sub>2</sub> [89]. Furthermore, an additional peak at 226 eV appeared after annealing, which corresponds to the S<sub>2s</sub> state. The ratio between Mo<sub>3d</sub> peak and S<sub>2s</sub> is found to be 1:1.85, which also confirms the formation of MoS<sub>2</sub> after annealing as verified by UV-Vis and Raman spectroscopy. The atomic ratio between Mo and S indicates the sulfur concentration is about 10% lower in the MoS<sub>2</sub> obtained films, in comparison to an ideal MoS<sub>2</sub> ratio (1:2). The deficiency of sulfur gives rise to point defects in the MoS<sub>2</sub>

crystal, such as S-vacancies [76]. At the S-vacancy sites, the access of Mo atoms introduces gap state that increases the efficiency for HER [76], [24].

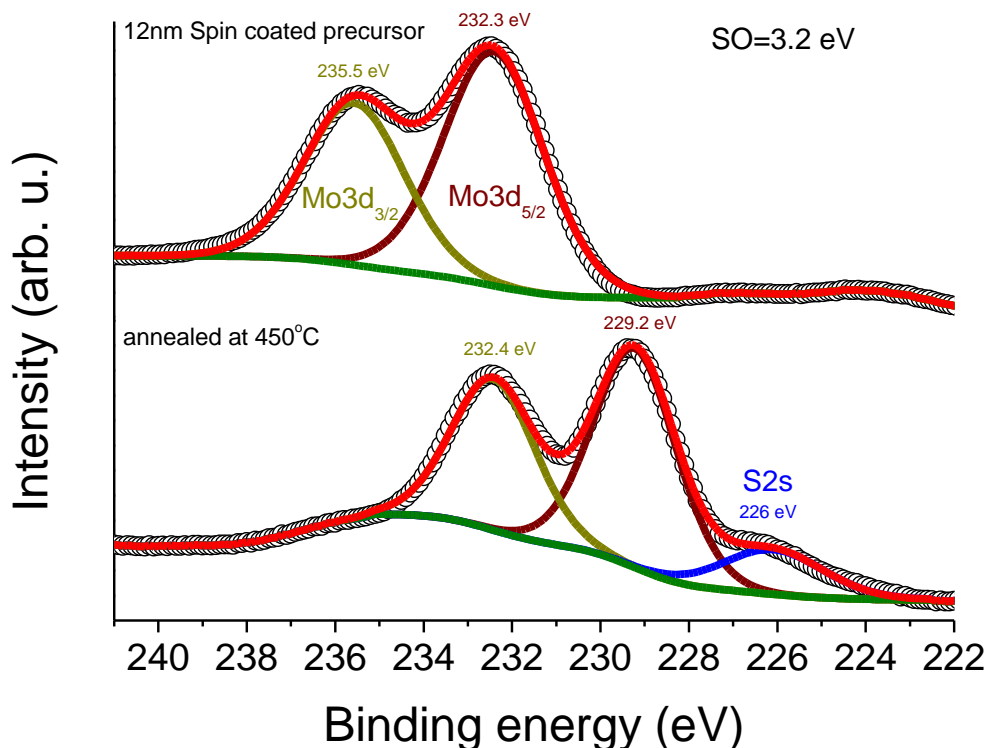
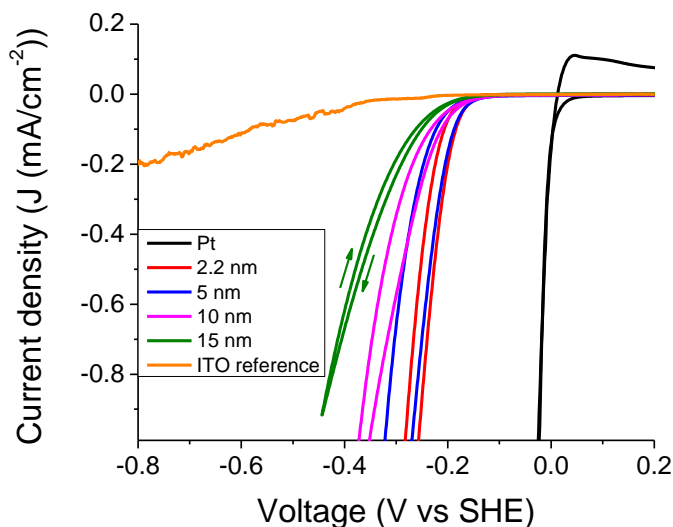


Figure 5-5 XPS: Mo<sub>3d</sub> and S<sub>2s</sub> energy range before and after conversion to MoS<sub>2</sub>.

## 5.4. Hydrogen evolution reaction

To confirm the HER activity of the obtained MoS<sub>2</sub> films, the films were deposited on a nonactive substrate for HER, i.e. a 180 nm ITO/glass substrate. For this purpose, first bare ITO/glass was measured with respect to the standard hydrogen electrode (SHE) to see the HER activity of the bare substrate only. In the polarization curve of the bare ITO/glass (figure 5.6) a slight increase in the current density is observed but from this measurement, the overpotential cannot be obtained within the limits of the measurement range. Similarly,

bare Pt was measured as a reference which exhibited an overpotential at -0.02 V, which was obtained for a current density of 1 mA/cm<sup>2</sup>. For all MoS<sub>2</sub> films with different thicknesses on ITO/glass substrate, distinct HER activity was observed. The visible hysteresis is caused by H<sub>2</sub> bubble formation. Therefore, HER activity determination is done in the forward direction only, where fewer bubbles are present on the ITO/glass surface. Furthermore, a systematic decrease in the overpotential with increasing thickness of the MoS<sub>2</sub> films was observed. The best HER activity was found for the 2.2 nm thick MoS<sub>2</sub> film at an over-voltage -0.25 V while for 15 nm thickness the HER activity is observed at -0.44 V only. The decreasing overpotential with increasing thickness is attributed to a series resistance effect in the film. The quality of the MoS<sub>2</sub> films doesn't change with thickness as the Raman peak shape remains unaltered and their FWHM remains constant (see figure 5.3)



*Figure 5-6 Polarization curves of Pt and ITO as reference and MoS<sub>2</sub> films with different thicknesses on ITO/glass substrate. Scans start at 0.2 V with the forward and backward directions indicated by the arrows.*

To check the reaction rate of the HER, the Tafel slope was extracted from the polarization curve in a Tafel plot for the 2.2 nm thick MoS<sub>2</sub> film (figure 5.7). Tafel plots of 43, 51, 74 and 81 mV per decade for thicknesses of 2.2 nm, 5 nm, 10 nm and 15 nm MoS<sub>2</sub> on ITO. Thin films perform better than thicker films. The Tafel slope is inversely proportional to the reaction rate of HER, i.e. increment in overpotential required for tenfold reaction rate. MoS<sub>2</sub> films deposited by electrodeposition on glassy carbon are reported to have 40 mV/decade [28] which is comparable to this work. The reported Tafel slope for the single crystal MoS<sub>2</sub> is worse with a value of 61-74 mV/decade [90]. Analogue 2D transition metal dichalcogenide such as WS<sub>2</sub> exhibited even worse values of 90-147 mV/decade [5], [91], [92].

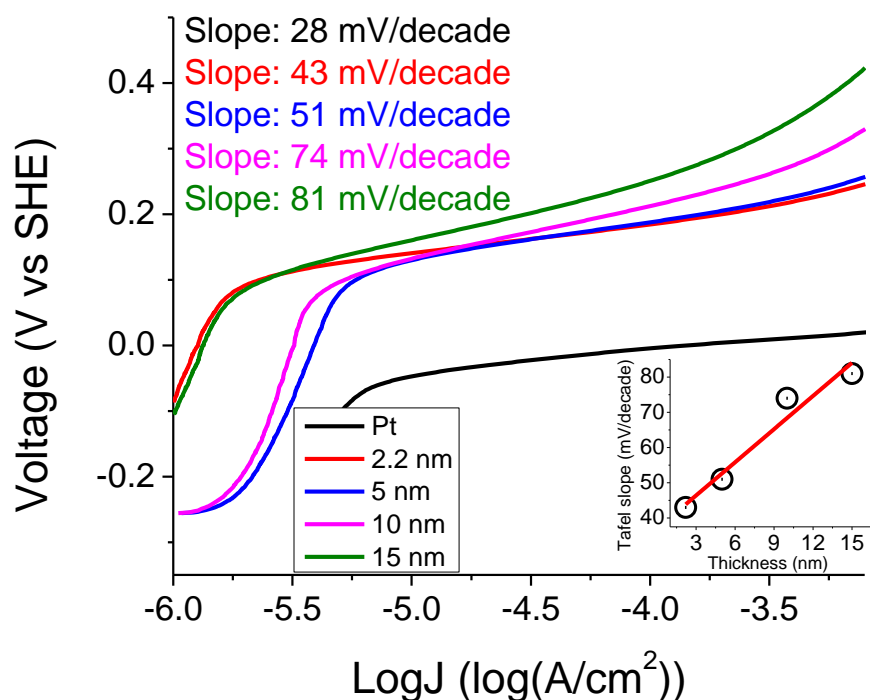


Figure 5-7 . Tafel plot extracted from the polarization curve in the forward direction of 2.2 nm MoS<sub>2</sub> film.

## 5.5. Conclusion

Thin films of MoS<sub>2</sub> were successfully deposited by mean of spin coating followed by post annealing at 450 °C with an additional sulfur source in Ar/H<sub>2</sub> environment. The roughness of the films was found to be less than 1nm, which means that the films were uniform and covering the surface completely. The films were characterized by Raman, UV-Vis and XPS before and after annealing. Best HER activity was observed for the thinnest film. The extracted Tafel slope from the polarization curve exhibits a low value of 43 mV/decade. Due to low cost and high abundance, MoS<sub>2</sub> is an interesting option to replace expensive noble metal catalyst for HER. Spin coating is a large area deposition technique which allows obtaining thin films of MoS<sub>2</sub> on a large scale. The presented method to prepare a HER-cathode is a promising way to produce hydrogen from water as fuel in the future.

## 6. Conclusions

In this work I have successfully deposited MoS<sub>2</sub>/WS<sub>2</sub> films/flakes using different solution-based deposition techniques, i.e. electrochemical deposition, dip-coating, and spin-coating. The obtained films/flakes were investigated for different applications.

Ultra-thin WO<sub>3</sub> flakes were successfully grown at the air-liquid interface and sulfurized at high temperature in the next step. To my best knowledge this is the first time WS<sub>2</sub> flakes have been obtained from the aqueous solution. For this purpose, ammonium tetrathiotungstate was used as a precursor material. The precursor solution was found to be stable at room temperature and under normal atmospheric pressure. The formation of the flakes at the air-liquid interface was observed above 50 °C after few hours. Which indicates that activation energy is required for the flake's formation at the air-liquid interface. The grown flakes were successfully transferred from the air-liquid interface to the silicon substrate by controlled dip-coating process. The spectroscopic investigation of the W-precursor showed that the initially obtained flakes are mainly composed of WO<sub>3</sub> with small ATTW residuals. Post-annealing step results in the successful conversion of WO<sub>3</sub> flakes to WS<sub>2</sub>. The post annealing was done with addition sulfur source in an inert environment. The obtained flakes were investigated by XPS, UV-Vis, Raman, and IR spectroscopy before and after post-annealing. Post-annealing temperature dependent Raman results showed that the crystallinity of the WS<sub>2</sub> flakes improves with increasing post-annealing temperature. The lateral size of the obtained flakes was found to be of different sizes. The lateral size of the biggest obtained flake was exceeding 100  $\mu m$  and the thickness of the thinnest flakes was



found to be 0.85 nm which is equivalent to the thickness of the monolayer of the WS<sub>2</sub>. Raman results showed that the crystal quality of the obtained WS<sub>2</sub> flakes at post-annealing temperature of 900 °C has similar to the WS<sub>2</sub> flakes grown by CVD and ALD. Hence the grown WS<sub>2</sub> flakes can also be used for different applications such as field effect transistors, spintronics.

Similarly, MoS<sub>2</sub> ultra-thin films have also been successfully grown by another solution-based process, i.e. electrochemical deposition at room temperature. Electrodeposition time was varied to get films with different thicknesses. MoS<sub>2</sub> films down to 1 nm was achieved which is equivalent to bilayer of MoS<sub>2</sub>. The confirmation of bilayer was done by AFM and Raman spectroscopy. The obtained films were uniform and closed as verified by AFM measurements. The roughness of the films was found to be independent of the thickness of the films. The electrochemically grown MoS<sub>2</sub> film was successfully transferred from initial Au growth substrate to a bare silicon substrate by a mechanical transferred method followed by gold etching. Such transferred method is an environmentally friendly. It does not damage the MoS<sub>2</sub> layers. The underlaying growth substrate can be reused. The electrochemically grown MoS<sub>x</sub> layer was successfully converted to MoS<sub>2</sub> by a post annealing step at high temperature (450-900°C) in an inert environment. This conversion was confirmed by UV-Vis, Raman and XPS spectroscopy. The crystallinity of the MoS<sub>2</sub> films was improved with higher annealing temperatures as verified by Raman spectroscopy.

The electrochemically grown layer were also used for hydrogen evolution reaction. For this purpose, thin films were grown on Au and ITO substrates. The post-annealing was done at maximum 450 °C because the underlying conducting layers are not stable at temperature higher than 500 °C. The initially grown electrochemically grown films were found to be made of MoS<sub>3</sub> as verified by Raman and XPS measurements. MoS<sub>3</sub> films were successfully converted to MoS<sub>2</sub> by post-annealing step as confirmed by Raman and XPS. These films showed good HER activity as deduced from the small overpotential and low Tafel slope of 44 mV/decade. Thinner films show better HER activity than thicker film which is attributed to resistance effects in the films.



## 7. References

- [1] Larscheid P, Lück L and Moser A 2018 Potential of new business models for grid integrated water electrolysis *Renew. Energy* **125** 599–608
- [2] Michalski J, Bünger U, Crotogino F, Donadei S, Schneider G S, Pregger T, Cao K K and Heide D 2017 Hydrogen generation by electrolysis and storage in salt caverns: Potentials, economics and systems aspects with regard to the German energy transition *Int. J. Hydrogen Energy* **42** 13427–43
- [3] Bartak D E, Kazee B, Shimazu K and Kuwana T 1986 Electrodeposition and Characterization of Platinum Microparticles in Poly(4-vinylpyridine) Film Electrodes *Anal. Chem.* **58** 2756–61
- [4] Jaramillo T F, Jørgensen K P, Bonde J, Nielsen J H, Hørch S and Chorkendorff I 2007 Identification of active edge sites for electrochemical H<sub>2</sub> evolution from MoS<sub>2</sub> nanocatalysts *Science (80-. )*. **317** 100–2
- [5] Wu Z, Fang B, Bonakdarpour A, Sun A, Wilkinson D P and Wang D 2012 WS<sub>2</sub> nanosheets as a highly efficient electrocatalyst for hydrogen evolution reaction *Appl. Catal. B Environ.* **125** 59–66
- [6] Saraiva E F and Milan L A 1998 Cramming More Components onto Integrated Circuits *Proc. IEEE* **86** 82–5
- [7] Novoselov K S, Geim A K, Morozov S V., Jiang D, Katsnelson M I, Grigorieva I

- V., Dubonos S V. and Firsov A A 2005 Two-dimensional gas of massless Dirac fermions in graphene *Nature* **438** 197–200
- [8] Radisavljevic B, Radenovic A, Brivio J, Giacometti V and Kis A 2011 Single-layer MoS<sub>2</sub> transistors *Nat. Nanotechnol.* **6** 147–50
- [9] Schmidt H, Wang S, Chu L, Toh M, Kumar R, Zhao W, Castro Neto A H, Martin J, Adam S, Özyilmaz B and Eda G 2014 Transport properties of monolayer MoS<sub>2</sub> grown by chemical vapor deposition *Nano Lett.* **14** 1909–13
- [10] Kuc A, Zibouche N and Heine T 2011 Influence of quantum confinement on the electronic structure of the transition metal sulfide T S 2 *Phys. Rev. B* **83** 245213
- [11] Ovchinnikov D, Allain A, Huang Y, Dumcenco D, Kis A, Federale E P and Engineering E 2014 Electrical Transport Properties *ACS Nano* **8** 8174–81
- [12] Debbarma R, Behura S K, Wen Y, Che S and Berry V 2018 WS<sub>2</sub>-induced enhanced optical absorption and efficiency in graphene/silicon heterojunction photovoltaic cells *Nanoscale* **10** 20218–25
- [13] Klots A R, Newaz A K M, Wang B, Prasai D, Krzyzanowska H, Lin J, Caudel D, Ghimire N J, Yan J, Ivanov B L, Velizhanin K A, Burger A, Mandrus D G, Tolik N H, Pantelides S T and Bolotin K I 2014 Probing excitonic states in suspended two-dimensional semiconductors by photocurrent spectroscopy *Sci. Rep.* **4** 1–7
- [14] Nisar T, Balster T, Haider A, Kortz U and Wagner V 2020 Growth of ultra-thin

large sized 2D flakes at air-liquid interface to obtain 2D-WS<sub>2</sub> monolayers *J. Phys. D. Appl. Phys.*

- [15] Hu Z, Bao Y, Li Z, Gong Y, Feng R, Xiao Y, Wu X, Zhang Z, Zhu X, Ajayan P M and Fang Z 2017 Temperature dependent Raman and photoluminescence of vertical WS<sub>2</sub>/MoS<sub>2</sub> monolayer heterostructures *Sci. Bull.* **62** 16–21
- [16] Xu Z, Lv Y, Li J, Huang F, Nie P and Zhang S 2019 RSC Advances monolayers *RSC Adv.* **9** 29628–35
- [17] Zink N, Therese H A, Pansiot J, Yella A, Banhart F and Tremel W 2008 In situ heating TEM study of onion-like WS<sub>2</sub> and MoS<sub>2</sub> nanostructures obtained via MOCVD *Chem. Mater.* **20** 65–71
- [18] Groven B, Heyne M, Mehta A N, Bender H, Nuytten T, Meersschaut J, Conard T, Verdonck P, Elshocht S Van, Vandervorst W, Gendt S De, Heyns M, Radu I, Caymax M and Delabie A 2017 Plasma-Enhanced Atomic Layer Deposition of Two-Dimensional WS<sub>2</sub> from WF<sub>6</sub>, H<sub>2</sub> Plasma, and H<sub>2</sub>S *Chemistry Mater.* **29** 2927–38
- [19] Jaegermann W and Tributsch H 1988 Interfacial properties of semiconducting transition metal chalcogenides *Prog. Surf. Sci.* **29** 1–167
- [20] Wang Q H, Kalantar-Zadeh K, Kis A, Coleman J N and Strano M S 2012 Electronics and optoelectronics of two-dimensional transition metal

dichalcogenides *Nat. Nanotechnol.* **7** 699–712

- [21] Voiry D, Salehi M, Silva R, Fujita T, Chen M, Asefa T, Shenoy V B, Eda G and Chhowalla M 2013 Conducting MoS<sub>2</sub> nanosheets as catalysts for hydrogen evolution reaction *Nano Lett.* **13** 6222–7
- [22] Zatko V, Galbiati M, Dubois S M, Och M, Palczynski P, Mattevi C, Brus P, Bezencenet O, Martin M, Servet B, Charlier J, Godel F, Vecchiola A, Bouzehouane K and Collin S 2019 Band-Structure Spin-Filtering in Vertical Spin Valves Based on Chemical Vapor Deposited WS<sub>2</sub> *ACS Nano* **13** 14468–76
- [23] Zhao Y, Liu J, Zhang X, Wang C, Zhao X, Li J and Jin H 2019 Convenient Synthesis of WS<sub>2</sub>-MoS<sub>2</sub> Heterostructures with Enhanced Photocatalytic Performance *J. Phys. Chem. C*
- [24] Li G, Zhang D, Qiao Q, Yu Y, Peterson D, Zafar A, Kumar R, Curtarolo S, Hunte F, Shannon S, Zhu Y, Yang W and Cao L 2016 All the Catalytic Active Sites of MoS<sub>2</sub> for Hydrogen Evolution *J. Am. Chem. Soc.* **138** 16632–8
- [25] Gomes F O V, Pokle A, Marinkovic M, Balster T, Canavan M, Fleischer K, Anselmann R, Nicolosi V and Wagner V 2018 Influence of temperature on morphological and optical properties of MoS<sub>2</sub> layers as grown based on solution processed precursor *Thin Solid Films* **645** 38–44
- [26] Zeng X, Hirwa H, Ortel M, Nerl H C, Nicolosi V and Wagner V 2017 Growth of

large sized two-dimensional MoS<sub>2</sub> flakes in aqueous solution *Nanoscale* **9** 6575–

80

- [27] Zeng X, Hirwa H, Metel S, Nicolosi V and Wagner V 2018 Solution processed thin film transistor from liquid phase exfoliated MoS<sub>2</sub> flakes *Solid. State. Electron.* **141** 58–64
- [28] Merki D, Fierro S, Vrubel H and Hu X 2011 Amorphous molybdenum sulfide films as catalysts for electrochemical hydrogen production in water *Chem. Sci.* **2** 1262–7
- [29] Lee C, Yan H, Brus L E, Heinz T F, Hone J and Ryu S 2010 Anomalous lattice vibrations of single- and few-layer MoS<sub>2</sub> *ACS Nano* **4** 2695–700
- [30] Zheng J, Sheng W, Zhuang Z, Xu B and Yan Y 2016 Universal dependence of hydrogen oxidation and evolution reaction activity of platinum-group metals on pH and hydrogen binding energy *Sci. Adv.* **2** 1–9
- [31] Tributsch H and Bennett J C 1977 Electrochemistry and photochemistry of MoS<sub>2</sub> layer crystals. I *J. Electroanal. Chem.* **81** 97–111
- [32] Novoselov K S, Geim A K, Morozov S V., Jiang D and Zhang Y 2004 Electric Field Effect in Atomically Thin Carbon Films *Science (80-. )*. **306** 666–70
- [33] Kam K K and Parkinson B A 1982 Detailed photocurrent spectroscopy of the semiconducting group VI transition metal dichalcogenides *J. Phys. Chem.* **86** 463–



- [34] Ballif C, Regula M and Le F 1999 Optical and electrical properties of semiconducting WS<sub>2</sub> thin films: From macroscopic to local probe measurements *Sol. Energy Mater. Sol. Cells* **57** 189–207
- [35] Tian K, Baskaran K and Tiwari A 2018 Growth of two-dimensional WS<sub>2</sub> thin films by pulsed laser deposition technique *Thin Solid Films* **668** 69–73
- [36] Lin H, Wang J, Luo Q, Peng H, Luo C, Qi R, Huang R, Travas-Sejdic J and Duan C G 2017 Rapid and highly efficient chemical exfoliation of layered MoS<sub>2</sub> and WS<sub>2</sub> *J. Alloys Compd.* **699** 222–9
- [37] Nguyen T P, Sohn W, Oh J H, Jang H W and Kim S Y 2016 Size-Dependent Properties of Two-Dimensional MoS<sub>2</sub> and WS<sub>2</sub> *J. Phys. Chem. C* **120** 10078–85
- [38] Cao S, Liu T, Hussain S, Zeng W, Peng X and Pan F 2014 Hydrothermal synthesis of variety low dimensional WS<sub>2</sub> nanostructures *Mater. Lett.* **129** 205–8
- [39] Qin Z, Loh L, Wang J, Xu X, Zhang Q, Haas B, Alvarez C, Okuno H, Yong J Z, Schultz T, Koch N, Dan J, Pennycook S J, Zeng D, Bosman M and Eda G 2019 Growth of Nb-Doped Monolayer WS<sub>2</sub> by Liquid-Phase Precursor Mixing *ACS Nano* **13** 10768–75
- [40] Yin H, Zhang X, Lu J, Geng X, Wan Y, Wu M and Yang P 2020 Substrate effects on the CVD growth of MoS<sub>2</sub> and WS<sub>2</sub> *J. Mater. Sci.* **55** 990–6

- [41] Genut M, Margulis L, Tenne R and Hodes G 1992 Effect of substrate on growth of WS<sub>2</sub> thin films *Thin Solid Films* **219** 30–6
- [42] Walton R I and Hibble S J 1999 A combined in situ X-ray absorption spectroscopy and X-ray *J. Mater. Chem.* **9** 1347–55
- [43] An G, Liu Y, Chai Y, Shang H and Liu C 2006 Synthesis , Characterization and Thermal Decomposition Mechanism of Cetyltrimethyl Ammonium Tetrathiotungstate *J. Nat. Gas Chem.* **15** 127–33
- [44] Daniel M F, Desbat B, Lassegues J C, Gerand B and Figilarz M 1987 Infrared and Raman Study of WO<sub>3</sub> Tungsten Trioxideand WO<sub>3</sub> xH<sub>2</sub>O Tungsten Trioxide Hydrates *J. Solid State Chem.* **67** 235–47
- [45] Srinivasan B R, Dhuri S N, Poisot M, Näther C, Bensch W and Kiel D- 2005 Synthesis , X-ray Structures , Spectroscopic and Thermal Characterization of Two New Organic Ammonium Tetrathiotungstates *J. Inorg. Gen. Chem.* **631** 1087–94
- [46] Medders G R and Paesani F 2015 Infrared and Raman Spectroscopy of Liquid Water through “ First- Principles ” Many-Body Molecular Dynamics *J. Chem. Theory Comput.* **11** 1145–54
- [47] Park J, Lee W, Choi T and Kim H 2014 Layer-modulated synthesis of uniform tungsten disulfide nanosheet using gas-phase precursors *Nanoscale* **7** 1308–13
- [48] Okada M, Sawazaki T, Watanabe K, Taniguch T, Hibino H, Shinohara H and

- Kitaura R 2014 Direct chemical vapor deposition growth of WS<sub>2</sub> atomic layers on hexagonal boron nitride *ACS Nano* **8** 8273–7
- [49] Cong C, Shang J, Wu X, Cao B, Peimyoo N, Qiu C, Sun L and Yu T 2014 Synthesis and optical properties of large-area single-crystalline 2D semiconductor WS<sub>2</sub> monolayer from chemical vapor deposition *Adv. Opt. Mater.* **2** 131–6
- [50] Song J G, Park J, Lee W, Choi T, Jung H, Lee C W, Hwang S H, Myoung J M, Jung J H, Kim S H, Lansalot-Matras C and Kim H 2013 Layer-controlled, wafer-scale, and conformal synthesis of tungsten disulfide nanosheets using atomic layer deposition *ACS Nano* **7** 11333–40
- [51] Kerkhof F P J M and Moulijn J A 1978 Elsevier Scientific Publishing Company, Amsterdam - Printed *J. Electron Spectrosc. Relat. Phenomena* **14** 453–66
- [52] Ryou J, Kim Y S, Santosh K C and Cho K 2016 Monolayer MoS<sub>2</sub> Bandgap Modulation by Dielectric Environments and Tunable Bandgap Transistors *Sci. Rep.* **6** 1–8
- [53] Nguyen V T, Ha S, Yeom D Il, Ahn Y H, Lee S and Park J Y 2019 Large-scale chemical vapor deposition growth of highly crystalline MoS<sub>2</sub> thin films on various substrates and their optoelectronic properties *Curr. Appl. Phys.* **19** 1127–31
- [54] Fan X, Singh D J and Zheng W 2016 Valence Band Splitting on Multilayer MoS<sub>2</sub>: Mixing of Spin-Orbit Coupling and Interlayer Coupling *J. Phys. Chem.*

- [55] Yorulmaz B, Özden A, Şar H, Ay F, Sevik C and Perkgöz N K 2019 CVD growth of monolayer WS<sub>2</sub> through controlled seed formation and vapor density *Mater. Sci. Semicond. Process.* **93** 158–63
- [56] Nisar T, Balster T, Haider A, Kortz U and Wagner V 2020 Growth of ultra-thin large sized 2D flakes at air-liquid interface to obtain 2D-WS<sub>2</sub> monolayers *J. Phys. D: Appl. Phys.* **54** 065301
- [57] Gomes F O V, Pokle A, Marinkovic M, Balster T, Anselmann R, Nicolosi V and Wagner V 2019 High mobility solution processed MoS<sub>2</sub> thin film transistors *Solid. State. Electron.* **158** 75–84
- [58] Ma D, Shi J, Ji Q, Chen K, Yin J, Lin Y, Zhang Y, Liu M, Feng Q, Song X, Guo X, Zhang J, Zhang Y and Liu Z 2015 A universal etching-free transfer of MoS<sub>2</sub> films for applications in photodetectors *Nano Res.* **8** 3662–72
- [59] Monk D J, Soane D S and Howe R T 1993 A review of the chemical reaction mechanism and kinetics for hydrofluoric acid etching of silicon dioxide for surface micromachining applications *Thin Solid Films* **232** 1–12
- [60] Brito J L, Ilija M and Hernández P 1995 Thermal and reductive decomposition of ammonium thiomolybdates *Thermochim. Acta* **256** 325–38
- [61] Bélanger D, Laperrière G and Marsan B 1993 The electrodeposition of amorphous
- 102

molybdenum sulfide *J. Electroanal. Chem.* **347** 165–83

- [62] King L A, Zhao W, Chhowalla M, Riley D J and Eda G 2013 Photoelectrochemical properties of chemically exfoliated MoS<sub>2</sub> *J. Mater. Chem. A* **1** 8935–41
- [63] Wieting T J and Verble J L 1971 Infrared and Raman studies of long-wavelength optical phonons in hexagonal MoS<sub>2</sub> *Phys. Rev. B* **3** 4286–92
- [64] Li H, Zhang Q, Yap C C R, Tay B K, Edwin T H T, Olivier A and Baillargeat D 2012 From bulk to monolayer MoS<sub>2</sub>: Evolution of Raman scattering *Adv. Funct. Mater.* **22** 1385–90
- [65] Tummala P, Lamperti A, Alia M, Kozma E, Nobili L G and Molle A 2020 Application-oriented growth of a molybdenum disulfide (MoS<sub>2</sub>) single layer by means of parametrically optimized chemical vapor deposition *Materials (Basel)*. **13** 1–13
- [66] Liu H, Zhu Y, Meng Q, Lu X, Kong S, Huang Z, Jiang P and Bao X 2017 Role of the carrier gas flow rate in monolayer MoS<sub>2</sub> growth by modified chemical vapor deposition *Nano Res.* **10** 643–51
- [67] Benoist L, Gonbeau D, Pfister-Guillouzo G, Schmidt E, Meunier G and Levasseur A 1994 XPS analysis of lithium intercalation in thin films of molybdenum oxysulphides *Surf. Interface Anal.* **22** 206–10

- [68] Zingg D S, Makovsky L E, Tischer R E, Brown F R and Hercules D M 1980 A surface spectroscopic study of molybdenum-alumina catalysts using x-ray photoelectron, ion-scattering, and Raman spectroscopies *J. Phys. Chem.* **84** 2898–906
- [69] Pak J, Lee I, Cho K, Kim J K, Jeong H, Hwang W T, Ahn G H, Kang K, Yu W J, Javey A, Chung S and Lee T 2019 Intrinsic Optoelectronic Characteristics of MoS<sub>2</sub> Phototransistors via a Fully Transparent Van Der Waals Heterostructure *ACS Nano* **13** 9638–46
- [70] Russell A E 2008 Faraday discussions: Preface *Faraday Discuss.* **140** 9–10
- [71] Li Y, Wang H, Xie L, Liang Y, Hong G and Dai H 2011 MoS<sub>2</sub> nanoparticles grown on graphene: An advanced catalyst for the hydrogen evolution reaction *J. Am. Chem. Soc.* **133** 7296–9
- [72] Wu Z, Fang B, Wang Z, Wang C, Liu Z, Liu F, Wang W, Alfantazi A, Wang D and Wilkinson D P 2013 MoS<sub>2</sub> nanosheets: A designed structure with high active site density for the hydrogen evolution reaction *ACS Catal.* **3** 2101–7
- [73] Splendiani A, Sun L, Zhang Y, Li T, Kim J, Chim C Y, Galli G and Wang F 2010 Emerging photoluminescence in monolayer MoS<sub>2</sub> *Nano Lett.* **10** 1271–5
- [74] Chang C H and Chan S S 1981 Infrared and Raman studies of amorphous MoS<sub>3</sub> and poorly crystalline MoS<sub>2</sub> *J. Catal.* **72** 139–48

- [75] Scofield J H 1976 Hartree-Slater subshell photoionization cross-sections at 1254 and 1487 eV *J. Electron Spectros. Relat. Phenomena* **8** 129–37
- [76] Li H, Du M, Mleczko M J, Koh A L, Nishi Y, Pop E, Bard A J and Zheng X 2016 Kinetic Study of Hydrogen Evolution Reaction over Strained MoS<sub>2</sub> with Sulfur Vacancies Using Scanning Electrochemical Microscopy *J. Am. Chem. Soc.* **138** 5123–9
- [77] Ye G, Gong Y, Lin J, Li B, He Y, Pantelides S T, Zhou W, Vajtai R and Ajayan P M 2016 Defects Engineered Monolayer MoS<sub>2</sub> for Improved Hydrogen Evolution Reaction *Nano Lett.* **16** 1097–103
- [78] Eda G, Yamaguchi H, Voiry D, Fujita T, Chen M and Chhowalla M 2011 Photoluminescence from chemically exfoliated MoS<sub>2</sub> *Nano Lett.* **11** 5111–6
- [79] Mak K F, Lee C, Hone J, Shan J and Heinz T F 2010 Atomically thin MoS<sub>2</sub>: A new direct-gap semiconductor *Phys. Rev. Lett.* **105** 2–5
- [80] Divanis S, Kutlusoy T, Ingmer Boye I M, Man I C and Rossmeisl J 2020 Oxygen evolution reaction: A perspective on a decade of atomic scale simulations *Chem. Sci.* **11** 2943–50
- [81] Dam S, Thakur A, G. A and Hussain S 2019 Synthesis and characterisation of MoS<sub>2</sub> thin films by electron beam evaporation *Thin Solid Films* **681** 78–85
- [82] Nisar T, Balster T, Haider A, Kortz U and Wagner V 2021 Growth of ultra-thin

large sized 2D flakes at air–liquid interface to obtain 2D-WS<sub>2</sub> monolayers *J. Phys. D. Appl. Phys.* **54** 065301

- [83] Kaindl R, Bayer B C, Resel R, Müller T, Skakalova V, Habler G, Abart R, Cherevan A S, Eder D, Blatter M, Fischer F, Meyer J C, Polyushkin D K and Waldhauser W 2017 Growth, structure and stability of sputter-deposited MoS<sub>2</sub> thin films *Beilstein J. Nanotechnol.* **8** 1115–26
- [84] Kim S K, Song W, Ji S, Lim Y R, Lee Y B, Myung S, Lim J, An K S and Lee S S 2017 Synergetic effect at the interfaces of solution processed MoS<sub>2</sub>-WS<sub>2</sub> composite for hydrogen evolution reaction *Appl. Surf. Sci.* **425** 241–5
- [85] Gusmão R, Sofer Z, Marvan P and Pumera M 2019 MoS<sub>2</sub> versatile spray-coating of 3D electrodes for the hydrogen evolution reaction *Nanoscale* **11** 9888–95
- [86] Marchetti F, Pampaloni G and Zacchini S 2015 The reactivity of MoCl<sub>5</sub> with molecules containing the alcohol functionality *Polyhedron* **85** 369–75
- [87] Sarma D D and Rao C N R 1980 XPS studies of oxides of second- and third-row transition metals including rare earths *J. Electron Spectros. Relat. Phenomena* **20** 25–45
- [88] Lin Y-C, Zhang W, Huang J-K, Liu K-K, Lee Y-H, Liang C-T, Chu C-W and Li L-J 2012 Wafer-scale MoS<sub>2</sub> thin layers prepared by MoO<sub>3</sub> sulfurization *Nanoscale* **4** 6637



- [89] Muijsers J C, Weber T, Vanhardeveld R M, Zandbergen H W and Niemantsverdriet J W 1995 Sulfidation study of molybdenum oxide using  $\text{MoO}_3/\text{SiO}_2/\text{Si}(100)$  model catalysts and  $\text{Mo-IV-S}_3$ -sulfur cluster compounds *J. Catal.* **157** 698–705
- [90] Shi J, Ma D, Han G F, Zhang Y, Ji Q, Gao T, Sun J, Song X, Li C, Zhang Y, Lang X Y, Zhang Y and Liu Z 2014 Controllable growth and transfer of monolayer  $\text{MoS}_2$  on Au foils and its potential application in hydrogen evolution reaction *ACS Nano* **8** 10196–204
- [91] Liu M, Geng A and Yan J 2020 Construction of  $\text{WS}_2$  triangular nanoplates array for hydrogen evolution reaction over a wide pH range *Int. J. Hydrogen Energy* **45** 2909–16
- [92] Thangasamy P, Raj J A and Sathish M 2020 Transformation of multilayer  $\text{WS}_2$  nanosheets to 1D luminescent  $\text{WS}_2$  nanostructures by one-pot supercritical fluid processing for hydrogen evolution reaction *Mater. Sci. Semicond. Process.* **119** 105167
- [93] Kobayashi M More than moore *Nature.com* (Available <https://www.nature.com/news/the-chips-are-down-for-moore-s-law-1.19338>)  
Accessed Oct. 2020
- [94] JF M 1995 *Handbook of x-ray photoelectron spectroscopy* (Physical Electronics, Eden Prairie)



## List of Publications

Talha Nisar's ORCID :

<https://orcid.org/0000-0003-0091-362X>



## Journal Contribution

### Primary publications

- Title: Growth of ultra-thin large sized 2D flakes at air-liquid interface to obtain 2D-WS<sub>2</sub> monolayers (Jan, 2021)  
Journal: Journal of Physics D: Applied Physics (IOP)  
DOI: <https://doi.org/10.1088/1361-6463/abc198>
- Title: Spin coating MoS<sub>2</sub> films for hydrogen evolution reaction  
Journal: Thin Solid Films (Submitted in Dec 2020)
- Title: Mechanical transfer of electrodeposited MoS<sub>2</sub> to silicon wafer  
Journal: Applied of Applied Electrochemistry (Submitted in Dec 2020)

### Publications with co-authorship

- Title: Improving Lithium-Ion Half-/Full-Cell Performance of WO<sub>3</sub>-Protected SnO<sub>2</sub> Core-Shell Nanoarchitectures (Nov, 2020)  
Journal: ChemSusChem (Wiley)  
DOI: <https://doi.org/10.1002/cssc.202002408>
- Title: Palladium (II)-Containing Tungstoarsenate (V), [Pd<sup>II</sup><sub>4</sub>(As<sub>2</sub>W<sub>15</sub>O<sub>56</sub>)<sub>2</sub>]<sup>16-</sup>, and Its Catalytic Properties (Sep, 2020)  
Journal: Inorganic Chemistry (ACS)

DOI: <https://doi.org/10.1021/acs.inorgchem.0c01737>

- Title : Tetra-Mn<sup>III</sup>-Containing 30-Tungsto-4-phosphate, [  $Mn_4^{III} (H_2O)_2(P_2W_{15}O_{56})_2$  ]<sup>12-</sup>: Synthesis, Structure, XPS, Magnetism, and Electrochemical Study (Aug, 2020)  
Journal: Inorganic Chemistry (ACS)  
DOI: <https://doi.org/10.1021/acs.inorgchem.0c01231>
- Title : Polyoxopalladate-Loaded Metal–Organic Framework (POP@MOF): Synthesis and Heterogeneous Catalysis (July, 2020)  
Journal: Inorganic Chemistry (ACS)  
DOI: <https://doi.org/10.1021/acs.inorgchem.0c00875>
- Title : Peroxo-Cerium(IV)-Containing Polyoxometalates: [  $Ce_6^{IV} (O_2)_9(GeW_{10}O_{37})_3$  ]<sup>24-</sup>, a Recyclable Homogeneous Oxidation Catalyst (Aug, 2019)  
Journal: Inorganic Chemistry  
DOI: <https://doi.org/10.1021/acs.inorgchem.9b01164>
- Title : Discovery of Polyoxo-Noble-Metalate-Based Metal–Organic Frameworks (Feb, 2019)  
Journal: Journal of American Chemical Society, JACS (ACS)  
DOI: <https://doi.org/10.1021/jacs.8b13397>
- Title : Electrochemically deposited amorphous cobalt-nickel-doped copper oxide as efficient electrocatalyst towards water oxidation reaction.  
Journal: ACS Omega (Submitted in March 2021)

## Conference contributions

- Title : Electrochemical growth and characterization of molybdenum sulfide layers for thin film transistors  
Conference: Deutsche Physikalische Gesellschaft (DPG), Regensburg, Germany, March 2016.  
Serial no: HL 533, Talk  
Online Abstract: [Verhandlungen der Deutschen Physikalischen Gesellschaft \(dpg-verhandlungen.de\)](http://www.dpg-verhandlungen.de)
- Title: Characterization of electrochemically deposited MoS<sub>x</sub> layers for thin film transistors  
Conference: Deutsche Physikalische Gesellschaft (DPG), Dresden, Germany, March 2017.  
Serial no: HL 99, Talk  
Online abstract: [Verhandlungen der Deutschen Physikalischen Gesellschaft \(dpg-verhandlungen.de\)](http://www.dpg-verhandlungen.de)
- Title: Characterization of dip coated tungsten sulfide flakes  
Conference: Deutsche Physikalische Gesellschaft (DPG), Berlin, Germany, March 2018.  
Serial no: HL 95, Talk  
Online abstract: [Verhandlungen der Deutschen Physikalischen Gesellschaft \(dpg-verhandlungen.de\)](http://www.dpg-verhandlungen.de)
- Title: Growth of large sized 2D molybdenum sulfide flakes at the air-liquid interface.  
Conference: Deutsche Physikalische Gesellschaft (DPG), Berlin, Germany, March 2018.  
Serial no: DS 06, Talk  
Online abstract: [Verhandlungen der Deutschen Physikalischen Gesellschaft \(dpg-verhandlungen.de\)](http://www.dpg-verhandlungen.de)
- Title: Transfer of electrodeposited MoS<sub>2</sub> to silicon substrate for electronic devices.

Conference: Deutsche Physikalische Gesellschaft (DPG), Regensburg, Germany, March 2019.

Serial no: HL 316, Talk

Online abstract: [Verhandlungen der Deutschen Physikalischen Gesellschaft \(dpg-verhandlungen.de\)](https://www.dpg-verhandlungen.de)

- Title: Novel deposition approach of MoS<sub>2</sub> thin films for hydrogen evaluation reaction

Conference: Deutsche Physikalische Gesellschaft (DPG), Regensburg, Germany, March 2019.

Serial no: DS 22, Talk

Online abstract: [Verhandlungen der Deutschen Physikalischen Gesellschaft \(dpg-verhandlungen.de\)](https://www.dpg-verhandlungen.de)

- Title: Growth of ultra-thin large sized 2D WS<sub>2</sub> monolayer flakes in at air-liquid interface.

Conference: Deutsche Physikalische Gesellschaft (DPG), Dresden, Germany, March 2020.

Serial no: DS 14, Talk

Online abstract: [Verhandlungen der Deutschen Physikalischen Gesellschaft \(dpg-verhandlungen.de\)](https://www.dpg-verhandlungen.de)

Note: Abstract was accepted but DPG spring meeting was cancelled because of COVID-19 outbreak.